Title

Microscopy of Bioelectric Potentials using Electrochromism

ISBN

9798189270901

Author

Ahmed, Burhan

Publication Date

2026-05-01

Peer reviewed|Thesis/dissertation

Microscopy of Bioelectric Potentials using Electrochromism

by

Burhan Ahmed

A dissertation submitted in partial satisfaction of the

requirements for the degree of

Doctor of Philosophy

in

Physics

in the

Graduate Division

of the

University of California, Berkeley

Committee in charge:

Professor Holger Müller, Chair
Professor Na Ji
Associate Professor Evan Miller

Spring 2026

Microscopy of Bioelectric Potentials using Electrochromism

Abstract

Microscopy of Bioelectric Potentials using Electrochromism

by

Burhan Ahmed

Doctor of Philosophy in Physics

University of California, Berkeley

Professor Holger Müller, Chair

Recording the electrical signals of biological cells is key to understanding processes that are integral to life. Electrochromic optical recording (ECORE) utilizes the electrochromism of certain materials to noninvasively record bioelectric signals. In this dissertation, we study the development of microscope ECORE, an advanced method based on ECORE and a high-NA microscope objective. We demonstrate a twofold enhancement in the spatial resolution, while also achieving a detection limit — the smallest possible potential that can be detected — of 3 µV, an improvement on previous ECORE methods. We use microscope ECORE to record spontaneous extracellular action potentials from cardiomyocytes with single-cell resolution and simultaneously utilize the objective to image the cells, which was not possible with previous iterations of ECORE. Because microscope ECORE makes use of an objective and a commercial microscope base, it is also simpler to set up and easier to align than any previous ECORE setup. This makes it a more viable recording method for many labs and therefore makes ECORE more accessible to the broader research community, providing a powerful, noninvasive, label-free method to record vital bioelectric signals.

To my wife, my parents, my sisters, and to everyone fighting for a more just world

Contents

Contents ii

List of Figures v

List of Tables vii

1 Introduction 1
- 1.1 Motivation . . . 1
- 1.2 Overview of this dissertation . . . 3

2 Background 5
- 2.1 Action potentials . . . 5
  - 2.1.1 Neurons . . . 6
  - 2.1.2 Cardiomyocytes . . . 8
  - 2.1.3 Intracellular and extracellular potentials . . . 10
- 2.2 Electrode-based recording of action potentials . . . 10
  - 2.2.1 Patch clamp . . . 10
  - 2.2.2 Multielectrode arrays . . . 12
- 2.3 Optical recording of action potentials . . . 13
  - 2.3.1 Fluorescent indicators . . . 13
  - 2.3.2 Label-free optical recording of action potentials . . . 14

3 Theory 15
- 3.1 Introduction to Electrochromic Optical Recording (ECORE) . . . 15
- 3.2 Electrochromism . . . 15
  - 3.2.1 Suitable electrochromic materials . . . 16
- 3.3 Interaction of light with material interfaces . . . 18
  - 3.3.1 Light at the interface of two materials . . . 18
    - 3.3.1.1 If both materials have real refractive indices . . . 20
    - 3.3.1.2 If material 2 has a complex refractive index . . . 24
  - 3.3.2 Interaction with a multilayer sample . . . 24
    - 3.3.2.1 Multilayer optical interactions in ECORE . . . 27

3.4 Application of voltage signals to samples . . . 30
3.4.1 Potentiostats . . . 30
3.5 Signal detection . . . 32
3.6 Previous ECORE experiments . . . 34
3.6.1 Original ECORE . . . 34
3.6.1.1 Experimental setup . . . 34
3.6.1.2 Setup optimization . . . 35
3.6.1.3 Sample optimization . . . 36
3.6.1.4 Results of cell-free experiments . . . 36
3.6.1.5 Results of cellular experiments . . . 37
3.6.2 Dual-color ECORE . . . 37
3.6.3 ECORE with alternative materials . . . 39
3.6.4 Summary of previous methods . . . 39
3.7 ECORE with microscope objectives . . . 40

4 Experimental Setup **41**
4.1 Introduction to microscope ECORE . . . 41
4.2 Theoretical considerations . . . 41
4.2.1 Diffraction limit . . . 41
4.2.2 High-NA objectives . . . 42
4.2.3 Parasitic reflections and light sources . . . 43
4.3 Sample preparation . . . 46
4.4 Optical setup . . . 47
4.4.1 Key components . . . 47
4.4.1.1 Light source . . . 47
4.4.1.2 Microscope and objective . . . 48
4.4.1.3 Detector . . . 48
4.4.2 Description of the setup . . . 48
4.4.2.1 Advantages . . . 49
4.5 Spatial resolution and spot size . . . 50
4.5.1 Setup capabilities . . . 50
4.5.2 Spot size used in the experiment . . . 51
4.6 Data recording and analysis . . . 52
4.6.1 Recorded signal and reflectance changes . . . 53
4.7 Noise mitigation . . . 55

5 Cell-Free Experiments with Microscope ECORE **58**
5.1 Setup considerations . . . 58
5.2 Typical cell-free recordings . . . 59
5.3 Sample optimizations for microscope ECORE . . . 60
5.3.1 PEDOT deposition method and input polarization . . . 61
5.3.2 PEDOT and PProDOT comparison . . . 62

5.3.3 Thickness of PEDOT thin films . . . 63
5.4 PEDOT response to applied voltages . . . 64
5.4.1 Bias voltage . . . 64
5.4.2 Magnitude of the applied square wave . . . 66
5.5 Microscope ECORE performance . . . 67

6 Cellular Recordings with Microscope ECORE **72**
6.1 Setup and sample considerations . . . 72
6.2 Action potential recordings . . . 74
6.3 Identification of electrical and mechanical signals . . . 75
6.4 Limits to recording duration . . . 77
6.5 Spatial mapping of potentials . . . 79

7 Summary and Outlook **83**
7.1 Improved spatial resolution . . . 84
7.2 Prolonged recording duration . . . 84
7.3 Dual-color microscope ECORE . . . 85
7.4 Simultaneous spatial mapping of potentials . . . 85
7.5 Conclusion . . . 86

Bibliography **87**

List of Figures

1.1 Using electrochromism for label-free recording . . . 3

2.1 Neuronal action potential . . . 7
2.2 Cardiomyocyte action potential . . . 9
2.3 Patch clamp method . . . 11
2.4 Multielectrode array . . . 12

3.1 Light reflection and refraction at the interface of two materials . . . 19
3.2 Reflectance at the boundary of two lossless materials . . . 22
3.3 Reflectance from an absorbing material . . . 25
3.4 Interaction of light with multiple layers of materials . . . 26
3.5 A typical multilayer ECORE sample . . . 28
3.6 Potentiostat . . . 31
3.7 Balanced photodetector . . . 33
3.8 Original ECORE experiment . . . 35

4.1 Laser and superluminescent light source operation . . . 45
4.2 Microscope ECORE setup . . . 47
4.3 Objective BFP illumination and spot size . . . 52
4.4 Microscope ECORE beam spot size comparison . . . 53
4.5 Vibrational noise reduction . . . 56

5.1 Typical cell-free recording . . . 60
5.2 Spin-coated and electrodeposited PEDOT samples . . . 62
5.3 PEDOT and PProDOT samples . . . 63
5.4 PEDOT film thickness . . . 65
5.5 PEDOT response as a function of bias voltage . . . 66
5.6 Linearity of PEDOT response . . . 67
5.7 Microscope ECORE noise versus shot noise . . . 69
5.8 Signal-to-noise ratio of microscope ECORE . . . 71

6.1 Microscope ECORE recording of cardiomyocytes . . . 75
6.2 Electrical versus mechanical signals . . . 76
6.3 Cardiomyocyte action potentials . . . 78

6.4 Light induced damage to cardiomyocytes 79
6.5 Creating a map of cardiomyocyte action potentials 81

List of Tables

3.1 Typical ECORE sample layer parameters 28
3.2 Summary of previous ECORE experiments 40

5.1 Thickness of PEDOT films versus electrodeposition time 64

Acknowledgments

As I reflect on the past seven years that make up my PhD, it is clear to me that I have been challenged in ways that I didn't think possible, both by events within and beyond my control. For one thing, I could not have anticipated living through a global pandemic shortly after starting grad school. I also could not have imagined that my PhD would coincide with the highest of highs: I got married to the love of my life, got to see the birth of my nephew, and worked with the most wonderful organizers to build a fairer UC. I'm glad that I got to share these years with many incredible people, who helped in ways that I hope I can faithfully express in the next couple of pages.

I'd like to start by thanking my advisor, Professor Holger Müller, who has patiently guided me through my PhD for the past five years. In my experience, there are very few scientists who care both about the work they do and the people they do it with. That Holger cares about the work he does should be abundantly clear — just spend a few minutes talking to him about science! But I also want to stress that Holger treats everyone with patience, dignity, and respect. Above all, he cares for the personal well-being of everyone in his group. I have always felt comfortable sharing any challenges that I'm facing with Holger, knowing that he would fully understand. Holger: thank you for giving me the time, resources, and mentorship to be successful. I am fortunate to have been a graduate student in your lab.

I am grateful to Professor Na Ji and Professor Evan Miller for their guidance and support with my dissertation. I'd also like to thank Holger, Na, Evan, and Professor Oskar Hallatschek for agreeing to serve on my qualifying exam committee and for generously offering me their time and mentorship. It was a true pleasure to learn from you all.

Next, I must acknowledge the Müller group. We've always been a very large group, so I won't list everyone by name here for fear of accidentally leaving someone out! But let me just say that the breadth of knowledge in our group is astounding, and there's always someone you can talk to if you have a question. I want to thank every member of the group for creating a culture where curiosity is expected, mistakes are welcome, and help can always be found. It's been a privilege to do science in the Müller group. I'd like to thank Matt, Garrett, and James for creating just the right amount of silliness in the lab to make us productive but also keep things fun. A special thanks to Jon, SuryaNeil, Beth, and Sara whose support has kept our group organized, informed and, most importantly, well-fed.

Additionally, I'd like to thank the ECORE team, both in the Müller group at Berkeley and our collaborators in the Cui group at Stanford. Thank you to Kenneth and Dana, who have been valuable members of this team, and whose company in the lab I have very much enjoyed! Many thanks to Lothar, who helped greatly with the microscope ECORE experiments and in the writing of the resulting manuscript, and whose advice has been indispensable. As for our Stanford teammates, I'd like to thank Professor Bianxiao Cui who, along with Holger, has guided ECORE to a very engaging and fruitful place. I want to recognize Peter and Erica, whose guidance when I was starting out on this project was invaluable. Erica: thanks for your expertise, support, kindness, and most importantly, patience (I am embarrassed to count the number of times I have requested PEDOT samples from you). It was a pleasure

to do the cardiomyocyte experiments at Stanford with you — thank you for being there for them, even when you were busy with your own dissertation. Pengwei: I will always appreciate your kindness and eagerness to help — thank you so much.

In my early graduate career, at the peak of the uncertainty caused by the onset of the COVID-19 pandemic, I was fortunate to encounter some fantastic senior grads who kindly gave me their time and checked in on me to make sure my PhD was going okay. Thank you Olive, Nick, Conrad, Kayla, and Sam for all of your support and for helping me chart my path in grad school. I owe a special thanks to Olive, who mentored me on research projects when I was doing a rotation in my second year. Olive: you showed me how to do good science, and your support and guidance in those early days encouraged me to stand up for myself and seek out the best opportunities for my career. I am so grateful for our friendship.

An experience that had a profound impact on me was working with fellow members of our union, UAW 4811, to improve the working conditions of graduate workers. In multiple times of crisis when I felt totally powerless, my union siblings showed me that we can believe in a just world and gave me the courage to fight for it. There are too many amazing UAW folks to mention here, but I'll try my best anyway. Thank you to Greg, Vikram, Max, Noelle, Ahmed, Olive, Keaton, Tanzil, Leo, Mia, Iris, Steph, Jacob, Connor, Liz, Anjali, Reed, Max G, Vanessa, Christian, Cecile, Sam, Julia, Conor, Gabe, Elise, Cole, Ruby, Sebastian, Sarah, Khalid, and the many amazing members of the Physics OC. I have to give the most special shout out to Greg, Vikram, and Max for organizing (and organizing with) me, standing by me during some very tough times, and for their unwavering friendships. I am proud of the work we have all done together. Thank you for giving me hope.

I've met some fantastic people in my cohort. I'd like to start by thanking my roommates Ashwin and Ryan, whose company pulled me through the early days of the COVID-19 pandemic. I will always remember the laughter and smiles you brought to my face in what was otherwise a very dark time. I am thankful for the many meals from Las Cabañas that we got to share together. Alongside Ryan and Ashwin, I'm also grateful for the company of Isaac, Sajant, Madeline M, Madeline B, Malcolm, James, Stephen, Irian, Noah, Jeske, Jon, and Antonio (whom I'll count as an honorary cohort member). Thank you all (and those of you who I'm sure I've accidentally left out) for the memories we created playing board games, hanging out, playing softball and cricket, and binge-watching TV. You've all made this long journey incredibly enjoyable. This goes doubly-so for Ashwin, who in addition to being a roommate and cohortmate, has also been my labmate and officemate for the past few years. Ashwin: thanks for literally always being there for me. There is no one else I would rather have been stuck with in a hotel room in Orlando with COVID. Oh, and thanks for being a witness at my wedding, too. You're one-of-a-kind with your brilliant, charming, and friendly personality. I'm glad we've gotten so close and I'm proud to call you my friend.

I'd also like to thank some amazing people I met as an undergrad at Clark University for their support throughout and beyond my time at Clark. I wouldn't have been here without the support of my undergraduate advisors, Professor Michael Boyer and Professor Amir Aazami. Thank you both for sparking my curiosity for science and math, for being excellent mentors, and for helping me realize my dream of becoming a scientist. I would also

like to express my gratitude for Natasha Kothari and Mitchell Perry, my wonderful mentors at Clark University Admissions who helped me grow and hone my leadership skills as an Admissions Ambassador, and who assisted tremendously with my grad school applications. I'm so grateful for the friends I made at Clark, including Ram, Hassan, Miranda, Eli, Zohaib, Megan, Daniel, Andy, Aly, Shannon, Calvin, Timm, Greg, and Michael. In particular, Ram: thanks for also moving to California shortly after I did. And even though you sometimes annoy the hell out of me, I'm so glad we got to spend a lot of time together through many conferences (and a random spring break together). Thanks for being a great friend.

My family has given me the emotional and financial support to get me where I am today. Although it has been a long and tough journey being so far away from you all for the past 11 years, I am grateful for everything you've done for me and I'm proud to make you proud. To my parents Sajida and Farooq: thank you for loving me unconditionally, providing me with a nurturing environment, and for always encouraging me to pursue whatever interested me. Your parenthood is truly special and I will always be grateful to be your son. To my sisters Maryam and Sarah: thank you both for loving me, comforting me when I needed it the most, and for sharing my passion for getting takeout (much to our parents' dismay). Zafar: thanks for being the kindest, most-caring, and most-friendly brother-in-law (and also an obligatory "thanks for putting up with my sister"). Khodadad: you're too young to know this, but your wonderful, joyous presence in this world alone has been enough to get me over some tough motivational hurdles over the last couple of years. A special shout out to my cousin, Suhayb, who is doing wonderful things — I'm proud of you!

Getting married in grad school has also given me the great fortune of almost doubling my family. All of my in-laws have been amazing, fully taking me on as one of their own. To my mother-in-law Kim, my father-in-law Paul, and my sisters-in-law Marissa and Gabby: thank you for your kindness and for welcoming me into your home and your lives with such open arms. I always looks forward to seeing you all and spending time with you. It has been a privilege to get to know you all over the past few years.

There's one person I haven't mentioned yet, and that's my beautiful wife Brianna. Brianna: thank you for being there for me all of these years. Through good times and bad, your love has been a constant presence in my life and has kept me going. Whenever the world seems like a gloomy place, your warmth and optimism remind me that things will be okay. Without a doubt, I owe the successes of these past few years to you. I'm a lucky guy for having met you 11 years ago — and my life has been special ever since. I'm incredibly excited to continue building our lives together in the future. There's nobody in this world who understands me like you do, and there's no other way I would rather have it. I love you.

Chapter 1

Introduction

1.1 Motivation

Understanding and interpreting bioelectric signals is a key scientific challenge. Action potentials — dynamic changes in the transmembrane potential of a cell — are key to many physiological functions, such as memory formation [1, 2], muscle contraction [3], and the beating of the heart [4]. Understanding these signals can help identify safe and effective drug candidates, for example, by monitoring changes in the action potentials of cardiomyocytes [5, 6].

The recording of bioelectric signals is achieved through a vast collection of existing and emerging methods[1]. Over multiple decades, many methods have been developed and significant improvements have been made to various aspects of these methods, such as the signal-to-noise ratio (SNR) [7, 8].

Electrode-based techniques have been used for more than a century to record bioelectric signals from organisms [9]. The patch clamp [10, 11], which uses an electrode inside a small pipette placed in contact with a cell's membrane, is often considered the "gold standard" technique for the direct recording of intracellular action potentials [12, 13]. However, it is an invasive technique, causing damage to the cell and limiting the duration of the recording to just tens of minutes [12]. It is also labor-intensive and thus limited to just a few cells at a time. Other electrode-based techniques, such as multielectrode arrays [14], rely on electrodes placed outside a cell to measure the extracellular action potential. While multielectrode arrays are less invasive, they are fixed in space and therefore provide limited spatial flexibility when recording action potentials from a network of cells.

An alternative probe to physical electrodes is light [7, 12]. The most popular light-based methods use fluorescence — the absorption and subsequent emission of light by a molecule — to record electrical signals. For example, voltage sensitive dyes can be introduced into the cell membrane, labeling the membrane clearly with their fluorescent light. Some dyes

[1] Throughout this dissertation, the words *method* and *technique* are used interchangeably. Both refer to any apparatus or procedure that is used to record bioelectric signals.

are based on photoinduced electron transfer (PeT), where the application of a voltage drastically changes the emission of a fluorescent molecule attached to an electron-rich donor [15]. By causing significant changes in the transmembrane potential, action potentials cause the fluorescent light emitted by the dye to change. Thus, by continuously monitoring the fluorescent emission of the dyes, these molecules can be used as voltage indicators for the recording of action potentials. Many other fluorescence-based methods have also been developed [8, 12]. They offer excellent spatial resolution as the molecules are very small (often much smaller than the wavelength of the fluorescent light). They also offer high spatial flexibility since many indicators can be expressed in specific areas of interest. However, all fluorescent indicators suffer from photobleaching, which is when prolonged illumination of a fluorescent molecule renders it irreversibly unable to fluoresce. Photobleaching places limits on the recording duration of many fluorescence-based methods [12].

These limitations have led to an increase in label-free optical techniques for the recording of bioelectric signals. For example, atomic force microscopy (AFM) can be used to detect sub-nanometer movements of a cell [16]. Since action potentials can lead to changes in the volume of a cell, AFM can be used to indirectly detect action potentials without the need for any labeling molecules. Many other label-free techniques have also been proposed over the past years [12]. In another technique, nitrogen vacancy (NV) centers in diamonds are used to directly detect the small magnetic fields that are generated by the propagation of action potentials [17]. Label-free techniques are non-perturbative to cells and therefore more suitable for longer-term recordings of action potentials. However, since the existing label-free techniques measure very small changes, they often have low SNRs. This reduces the reliability of detecting single action potentials, or requires the averaging of multiple action potentials to provide a reasonable signal, which reduces their applicability in real-time measurements. Furthermore, in label-free methods that rely on indirect measurements, there is uncertainty about the underlying mechanisms that relate the effect being measured (e.g., the membrane movement using AFM) to action potentials [12]. Thus, concerns remain about the conclusions that can be drawn from such indirect methods.

To overcome this challenge, we have previously introduced a new label-free method called electrochromic optical recording (ECORE) [18–20]. The concept of ECORE is illustrated in Fig. 1.1. This method makes use of electrochromic materials, which change their optical properties in response to changes in potential. By culturing cells on top of a suitable electrochromic material, the extracellular action potentials of cells will change the index of refraction of the material. This change is then detected by monitoring how light interacts with the material over time. ECORE presents many advantages compared to traditional, electrode-based recording techniques. The lack of a physical electrode means that ECORE offers more flexibility to record from any user-designated region on the sample. ECORE is also noninvasive and the materials used are biocompatible, i.e., they do not adversely affect the cells being studied. This allows longer-term recording of action potentials from these cells. Recordings of spontaneous action potentials in neurons and cardiomyocytes have been demonstrated, showing the effectiveness of ECORE in recording bioelectric signals.

Despite the successful development and demonstration of ECORE, a few barriers remain

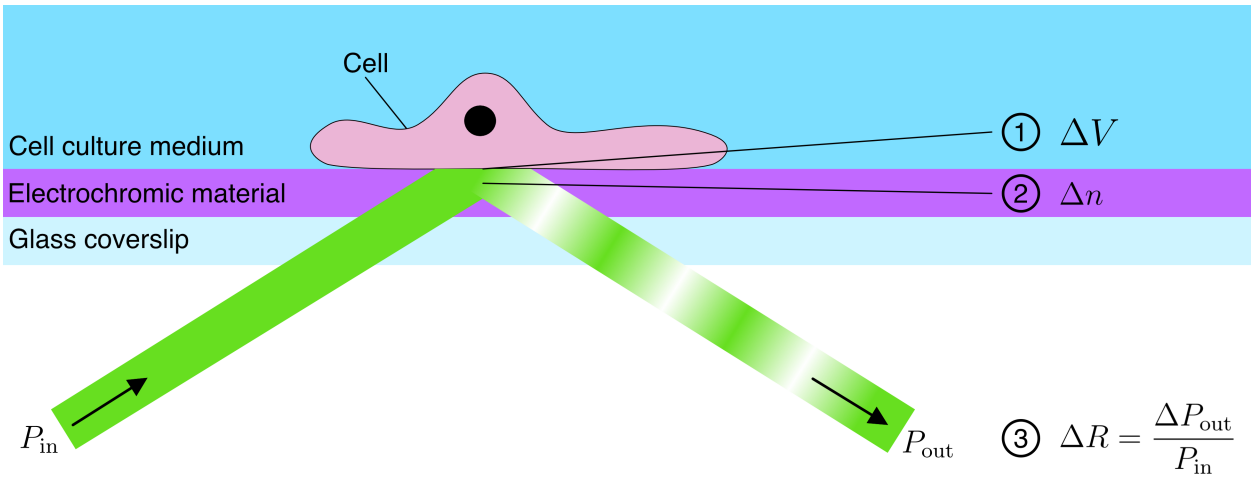

Figure 1.1: Schematic depicting the concept of electrochromic optical recording (ECORE). ECORE can be understood as a 3 step process. Step 1: a cell that is cultured on a thin film of an electrochromic material fires an action potential. This causes a local change in the potential outside the cell (ΔV). Step 2: as the potential changes, the index of refraction of the electrochromic material also changes (Δn). Step 3: light of power P_{in} interacts with the electrochromic material and some light is reflected with power P_{out}. Changes in the index of refraction of the material (Δn) over time cause the amount of light that is reflected from the sample to also change in response (ΔP_{out}). That is, the reflectance $R \equiv P_{\text{out}}/P_{\text{in}}$ of the sample changes over time (ΔR). By detecting the change in the reflectance over time, the action potential can be recorded.

to a wider implementation of the technique for the recording of bioelectric signals. One such limitation is the reliance of ECORE on specialized, custom optical setups, which may prevent it from being adopted by many labs working with cells. Another limitation is the spatial resolution of ECORE, which so far has been limited by the use of simple, low-numerical-aperture lenses. The combination of ECORE with common microscopy setups, which are widely-used in many research areas, would overcome both of these limitations and should enable more researchers to employ ECORE in their work.

1.2 Overview of this dissertation

This dissertation will describe significant advancements in ECORE. We will start by looking at the nature of action potentials and the techniques that are currently utilized to record them, and further motivate the need for improved label-free methods. This dissertation will then describe the optical theory necessary to understand how ECORE works. Finally, we describe microscope ECORE — the main subject of this dissertation — and how it builds

on previous iterations of electrochromic optical recording. We will go over the experimental setup and results that demonstrate the advantages presented by this new technique. Most importantly, we demonstrate that it represents a simplification of the optical setup of ECORE, and therefore should enable more researchers to utilize this versatile recording method in their research. Finally, we finish the dissertation by offering our perspective on future avenues of research that may build on this work and further strengthen ECORE for the recording of bioelectric potentials.

Chapter 2

Background

2.1 Action potentials

Cells and the environments in which they exist contain multiple species of ions, in particular sodium (Na^+), potassium (K^+), and calcium (Ca^{2+}). Cell membranes, which separate the inside of the cells from the extracellular environment, are typically impermeable to these ions except for specialized ion channels. These ion channels are transmembrane proteins that can open to permit certain ions to pass through the membrane, or close to decrease the permeability of the membrane to that specific ion species. Thus, ion channels give the membrane a varying degree of permeability for different ions.

In addition to ion channels, which allow diffusion of ions across the membrane (passive transport), cell membranes also contain ion pumps, which are transmembrane proteins that use energy to transport an ion species against its concentration gradient (active transport). These ion pumps work to maintain an imbalance of ion concentration across the membrane. Combined with the varying permeability of the membrane to different ion species, this means that the ionic concentrations inside and outside a cell are generally not the same. The concentration differences of each species combine to produce a potential difference across the membrane known as the transmembrane potential.

We are interested in exploring what happens when the permeability of the membrane is suddenly increased for some ion species X. Let's assume that the external concentration of X is higher than the internal concentration of X (i.e. $[X]_{\text{ext}} > [X]_{\text{int}}$). Because there is a concentration gradient, external X will tend to move into the cell to balance the internal and external concentrations. However, as external X flows inward, there will be a buildup of charge that opposes further inflow of X. That is, there is also an electrical potential gradient that must be considered. Thus, at equilibrium, the opposing forces due to the concentration gradient and the electrical potential gradient will balance out to give zero net flow of ion X across the membrane. The equilibrium potential at which this occurs is determined using the Nernst equation [21]:

$$V_X = \frac{RT}{z_X F} \ln\left(\frac{[X]_{\text{ext}}}{[X]_{\text{int}}}\right), \tag{2.1}$$

where $R = 8.314\,\mathrm{J\,mol^{-1}\,K^{-1}}$ is the gas constant, T is the temperature in Kelvin, z_X is the valency of species X, and $F = 9.6485 \times 10^4\,\mathrm{C\,mol^{-1}}$ is the Faraday constant. The equilibrium potential V_X tells us the hypothetical potential difference that would exist across the membrane if species X was allowed to flow until an equilibrium was reached.

However, when the cell is at rest, the membrane is more permeable to some ions than others. This means that the transmembrane potential for a cell at rest — the resting potential — is determined mostly by the ions that have the highest permeability in those conditions. On the other hand, if the permeability of the membrane to one ion species is suddenly increased, then eq. (2.1) shows us that this flow of ions will move the transmembrane potential towards the equilibrium potential of that ion species. This movement of ions transiently reverses the polarity of the transmembrane potential, and is called an action potential [21].

Action potentials are central to the regular and proper functioning of organisms. In neurons, for instance, an action potential may be generated as a response to some stimulus. This action potential then propagates down the nervous system, allowing the organism to respond to the stimulus. Irregularities in the generation or propagation of action potentials can have severe consequences. For example, multiple sclerosis can be attributed to the impaired propagation of the action potential due to improper myelination of axons [21].

Not all cells exhibit action potentials — those that do are known as excitable cells. We will describe the nature of action potentials in two different types of excitable cells: neurons and cardiomyocytes.

2.1.1 Neurons

Under resting conditions, i.e., when a neuron is not firing an action potential, the internal concentration of K^+ is higher than that of Na^+. This unequal distribution of ions is maintained through ion pumps which exchange internal Na^+ for external K^+ [21]. At typical resting concentrations in neurons, the equilibrium potentials for Na^+ and K^+ are $V_{Na^+} = 55\,\mathrm{mV}$ and $V_{K^+} = -103\,\mathrm{mV}$, respectively [21]. Since the membrane is more permeable to K^+ than to Na^+, the resting potential of the membrane is around $-60\,\mathrm{mV}$.

However, if the permeability of the membrane to Na^+ ions is increased, the concentration gradient will cause Na^+ ions to move into the cell. This raises the potential of the cell and is called depolarization. Conversely, if the permeability to K^+ ions is increased, K^+ ions will leave the cell causing the potential to drop. This is known as repolarization. Other ions can also be involved in changing the transmembrane potential, but the relative abundance of Na^+ and K^+ ions makes these species the major factors in neuronal action potentials.

The action potential in a neuron is traditionally said to consist of 3 phases, which are shown in Fig. 2.1:

- Phase 1: depolarization
- Phase 2: repolarization
- Phase 3: after-hyperpolarization

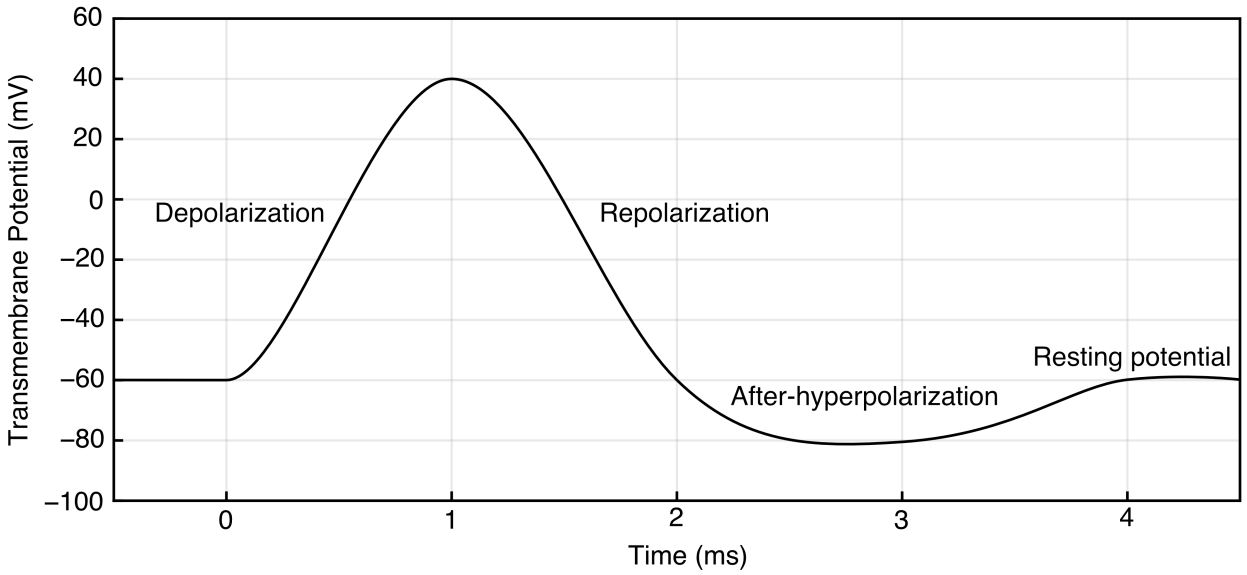

Figure 2.1: Schematic of a neuronal action potential. The phases identified in the text are labeled.

In the first phase, some local disturbance (for example, a stimulus) causes a slight depolarization of the transmembrane potential. Na^+ ion channels are voltage-sensitive (also called voltage-gated) and those in the vicinity of the depolarizing disturbance will open in response to this voltage change. This causes Na^+ ions to flow into the cell, causing further depolarization. If there is a strong enough disturbance and the transmembrane potential reaches a threshold value of around $-45\,\text{mV}$, all Na^+ channels open, causing a rapid inflow of Na^+ ions. This mechanism is responsible for the "all-or-nothing" characteristic of action potentials.

The sudden opening of the Na^+ channels leads to a rapid depolarization, increasing the potential inside the cell to $>0\,\text{mV}$. However, these Na^+ channels inactivate after $\sim 1\,\text{ms}$ due to the closing of an inactivation gate that prevents further Na^+ ions from crossing the membrane [21]. This causes the depolarization to slow down. Furthermore, at around the same time that the Na^+ channels are inactivated, the K^+ channels start to activate to allow K^+ to move from inside the cell to the extracellular medium. These K^+ channels require larger depolarizations to activate and have longer activation times than Na^+ channels. Thus, the opening of the K^+ channels not only slows down the depolarization, but leads to the second phase, i.e., the repolarization of the transmembrane potential. As opposed to Na^+ channels, K^+ channels do not quickly inactivate and therefore the transmembrane potential "overshoots" the original resting potential, leading to the third phase of the action potential: after-hyperpolarization.

As the transmembrane potential overshoots the original resting potential, the K^+ chan-

nels now start to inactivate to prevent the outward flow of intracellular K^+ ions. This low potential also aids in the recovery of the Na^+ channels from inactivation. Once both types of channels recover, the cell is ready to fire another action potential if there is another depolarizing disturbance.

The discussion of the transmembrane potential so far has focused on a small local region of the membrane. However, changes in the transmembrane potential in one region inevitably lead to depolarizing disturbances in neighboring regions. In this way, the action potential does not remain localized to one region of a cell, but rather is transmitted across a cell and into neighboring cells in a network of neurons. This mechanism of action potential propagation is responsible for the conduction of electrical signals in the nervous system.

2.1.2 Cardiomyocytes

Cardiomyocytes are the muscle cells of the heart and are responsible for the contraction and expansion of the heart, which causes blood to flow through the body. These cells therefore form the basis of the circulatory system. The generation and propagation of action potentials in cardiomyocytes is directly linked to the contraction and expansion of these cells by a process known as excitation-contraction coupling [22].

The internal concentration of K^+ in cardiomyocytes is higher than that of Na^+. These concentration differences lead to a resting potential of around $-80\,\mathrm{mV}$ [4]. The movement of ions, including K^+, Na^+, and Ca^{2+} across the cell membrane is responsible for action potentials in cardiomyocytes. Cardiomyocytes found in the working cells of the heart show characteristic action potentials that can be broken down into 5 phases [4, 23]:

- Phase 0: depolarization (or upstroke)
- Phase 1: early repolarization
- Phase 2: plateau
- Phase 3: primary repolarization
- Phase 4: resting potential

This action potential is depicted in Fig. 2.2. During phase 0, there is a rapid depolarization of the transmembrane potential which is caused by the rapid inflow of Na^+ ions into the cell. As in neurons, the current reaches a peak within 1 ms and the Na^+ channels are inactivated. During this process, the transmembrane potential increases by $\sim 100\,\mathrm{mV}$.

After the depolarization, the K^+ channels start to open and K^+ ions flow out from the cells, leading to a repolarization of the potential. However, unlike neurons, there are other effects which prevent a rapid repolarization. Chief among these is the role of Ca^{2+} ions, the inward flow of which approximately counteracts the outward flow of K^+ ions. This leads to phase 2 — the plateau phase. Ca^{2+} channels open even later than K^+ channels and take on

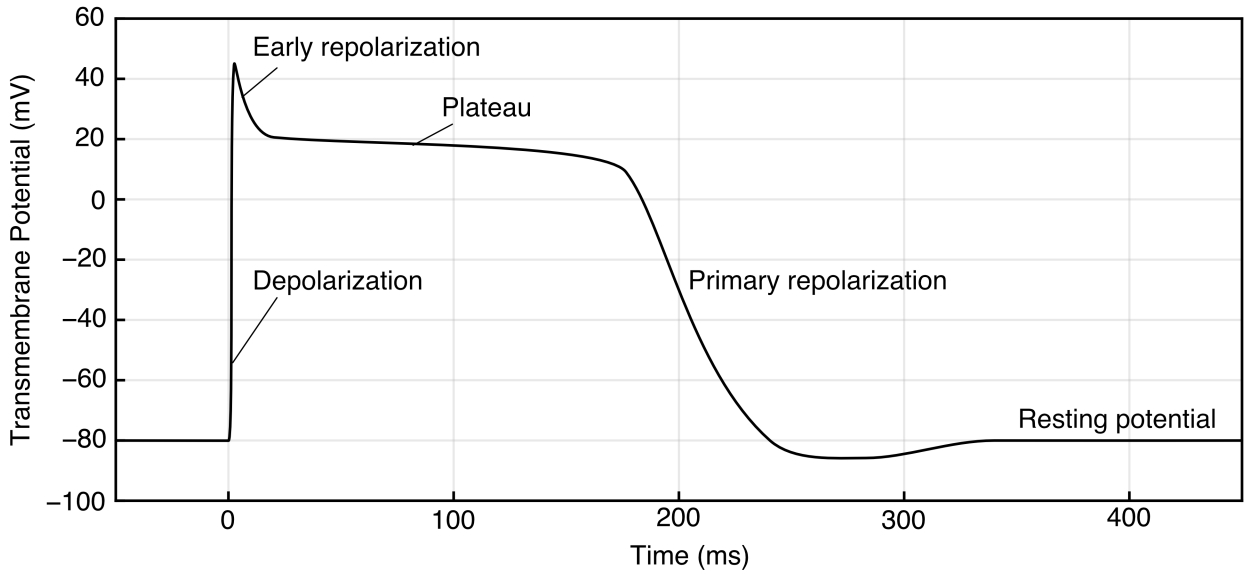

Figure 2.2: Schematic of a cardiomyocyte action potential. The phases identified in the text are labeled. Note the different time scale compared to Fig. 2.1.

the order of 100 ms to inactivate. Thus the plateau phase is fairly extended and prolongs the action potential in cardiomyocytes.

As the Ca^{2+} channels start to inactivate, the K^+ current becomes dominant and there is a larger, faster repolarization that occurs (phase 3). As the K^+ channels stay open longer, the transmembrane potential will drop back down towards the resting potential, where it will stay until another action potential is triggered (phase 4).

Therefore, compared to neuronal action potentials, which last only a few ms, cardiomyocyte action potentials are much longer in duration, lasting at least a few hundreds of ms. Cardiomyocyte action potentials are also more complex, with repolarization taking longer and involving more steps and ions.

Propagation of the action potential across a network of cardiomyocytes leads to the transmission of electrical signals. In addition to signaling, cardiomyocytes also contract and expand in response to the propagation of action potentials. Irregularities in the action potentials of cardiomyocytes are responsible for many heart disorders. One such example is Torsade de pointes (TdP), a serious arrhythmia (abnormal beating pattern) that can lead to cardiac arrest and death. TdP can be caused by some medications that prolong the depolarization-repolarization cycle of ventricular cardiomyocytes [5], which are located in the lower chambers of the heart. This prolongation significantly lengthens the duration of the action potential compared to the healthy, normal action potential depicted in Fig. 2.2, causing irregular beating of the heart. Therefore, in order to prevent TdP, drugs are often tested today to assess their risk of prolonging ventricular action potentials [5].

2.1.3 Intracellular and extracellular potentials

We have so far described the mechanisms underlying action potentials in neurons and cardiomyocytes. The recording of these action potentials represents a challenge, given that the transmembrane potential — by its very nature — can most faithfully be measured at the membrane. However, doing so means that a probe must be inserted into (or attached to) the membrane of the cell. This is typically achieved by bringing a physical electrode in close contact with the cell membrane, or by placing a fluorescent indicator in or near the membrane. Once the challenge of bringing a probe into contact with the membrane is overcome, detecting the action potential is relatively easy due to the large magnitudes of action potentials ($\sim$100 mV). We will refer to action potentials that are recorded at the membrane as intracellular action potentials.

Action potentials can also be measured in an extracellular manner if the probe is placed close to, but not in contact with, the cell membrane. As an action potential is generated in the nearby cell, there is a rapid flow of Na^+ ions into the cell. This flow of charge creates a local current in the extracellular medium. As the extracellular medium is resistive, this current flow leads to a drop in the voltage near the probe, which can be measured. Subsequent ion movement across the membrane, as described in the preceding sections, will lead to further voltage changes. We therefore get a voltage recording of the action potential, but measured extracellularly. We will refer to action potentials recorded in this way as extracellular action potentials.

Extracellular action potentials typically have much smaller magnitudes than their corresponding intracellular potentials. For example, extracellular cardiomyocyte action potentials have magnitudes of $\sim$100 µV [24, 25], about 3 orders of magnitude smaller than the intracellular action potentials. Therefore, methods that record extracellular action potentials need to be more sensitive. We will now discuss a few different recording techniques, both intracellular and extracellular.

2.2 Electrode-based recording of action potentials

Historically, bioelectric potentials have most often been recorded using physical electrodes. Even today, methods that utilize electrodes remain very common as they provide a time-tested, reliable way of recording transmembrane potential changes. Two common electrode-based methods include the patch clamp, which generally records the intracellular action potential, and multielectrode arrays, which typically record the extracellular action potential.

2.2.1 Patch clamp

In the mid-20th century, sharp glass electrodes were used to record intracellular action potentials from squid giant axons by puncturing the cell membrane [26, 27]. However, because the electrode punctured the membrane, this technique was very invasive and had a limited recording duration due to cellular damage. The invasive nature of the electrode

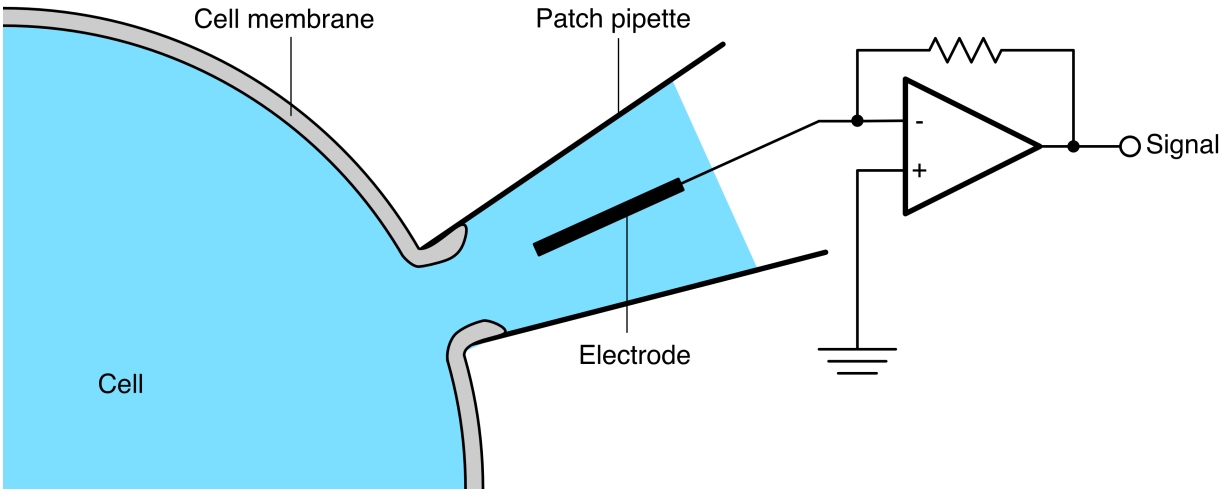

Figure 2.3: The patch clamp method in the "whole-cell" configuration. A small pipette is used to apply suction to the membrane until it ruptures. Using an electrode placed inside the pipette, the transmembrane potential can be recorded.

also led to additional complications. For example, the sharp electrodes did not form a high-resistance electrical seal with the membrane, allowing ionic current to leak through the electrode–membrane interface [11]. These leakage currents reduced the reliability of the method in measuring the true transmembrane potential changes caused by ion movements across an intact membrane.

A modification of this technique was subsequently developed to avoid puncturing the membrane [10]. Instead of using sharp electrodes, large-bore pipettes were used to form a tight seal with a small "patch" of the membrane, hence becoming known as the patch clamp method. In addition to being less invasive, this also allowed the recording of the activity of individual ion channels [10, 28]. Over time, the patch clamp method has evolved widely but remains the gold standard for electrophysiological recordings. Many different configurations of the patch clamp exist today. For example, in the "cell-attached" configuration, the patch pipette forms a seal with the membrane that leaves the membrane intact. From this configuration, if the suction is increased, the membrane can be ruptured and this leads to the "whole-cell configuration", shown in Fig. 2.3. Other configurations can also be achieved [11]. Furthermore, the experimenter can vary the type of recording — if the potential is kept fixed and the current is recorded, this is known as the "voltage clamp". On the other hand, in the "current clamp" mode, a fixed current is injected through the electrode and the voltage is monitored.

Regardless of the configuration used, the patch clamp method involves physical electrodes

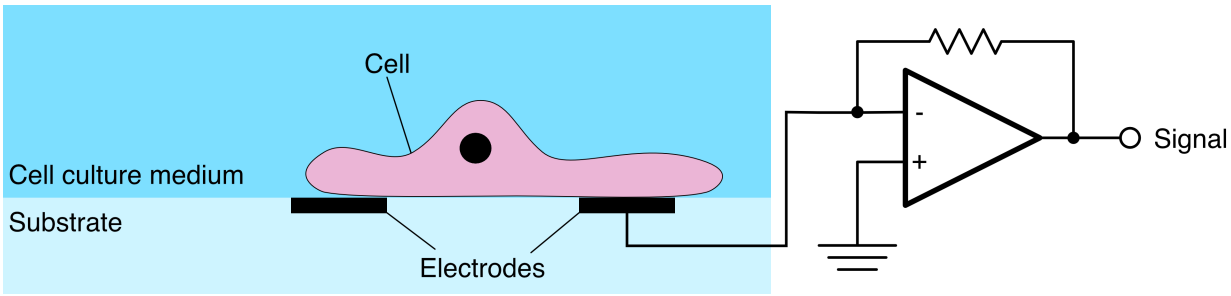

Figure 2.4: Multielectrode arrays can be used to record action potentials. Cells are cultured on a substrate which has a prefabricated array of electrodes. Electrodes in the proximity of a cell can detect changes in the potential around the cell, and can be used to record extracellular action potentials.

that are in contact with the cell, and is thus generally considered an invasive technique. This can limit the recording duration to tens of minutes [12]. Furthermore, the patch clamp method is laborious and difficult to perform at-scale, thus being limited to recording a handful of cells at a time. For this reason, while the patch clamp is still commonly used today to provide reliable recordings of action potentials with high temporal resolution, other techniques have been developed to supplement the patch clamp method.

2.2.2 Multielectrode arrays

If electrodes are brought in close proximity to the cell membrane, the extracellular action potentials of cells can be recorded. This is the idea underlying the use of multielectrode arrays [14]. Multielectrode arrays consist of a prefabricated pattern of physical electrodes on a substrate (Fig. 2.4). The specimen of interest is then deposited or cultured on top of this substrate, which brings the cells very close to the electrodes. By monitoring the potential changes at each of the electrodes, the extracellular action potential can be recorded. Multielectrode arrays have seen many developments over the years, including the combination of concepts from multielectrode arrays and patch clamp to enable intracellular recording of action potentials [29, 30].

Multielectrode arrays are generally noninvasive, allowing longer duration recordings. Traditional arrays typically consist of ∼60 electrodes [31], although recent advances in electrode technology have led to an increase in arrays with tens of thousands of electrodes [32, 33]. Because they employ many electrodes that can simultaneously record potentials, multielectrode arrays are also able to record from multiple cells at the same time, which can give useful information about how a network of cells communicates through the generation and transmission of signals. However, since the electrodes are fixed in place, the spatial flexibility of the technique is limited as the experimenter cannot arbitrarily select an area of the specimen to study in more detail.

2.3 Optical recording of action potentials

Due to the lack of spatial flexibility offered by physical electrodes (and in some cases their invasive nature, such as in the patch clamp), alternative light-based techniques have been developed. As light can be easily manipulated, this gives the experimenter a high level of spatial flexibility as well as control over the spatial resolution. We discuss optical recording methods of two distinct types: those involving fluorescent reporters (or labels) which respond to electrical activity, and those that are label-free.

2.3.1 Fluorescent indicators

Some of the most popular optical methods use fluorescent molecules that react to electrical activity by emitting light [7, 12]. By monitoring this emitted light using a microscope, action potentials can be recorded.

Calcium indicators, such as genetically encoded calcium indicators (GECIs), have a varying fluorescent signal in response to the calcium concentration around the indicator [12, 15]. Since the calcium concentration changes as an action potential is generated, the action potential can be studied by monitoring the fluorescence light emitted by the calcium indicators. These indicators are versatile and have been used in various studies of neuronal action potentials [34, 35]. However, as discussed previously, since the calcium concentration only changes on the order of $\sim$100 ms, these indicators can be slow to respond and therefore do not have the temporal resolution to reveal faster features of an action potential [12].

Another class of indicators are voltage sensitive dyes, which can be inserted into the cell membrane. The generation of an action potential will change the emission of the fluorescent molecules in the dyes, allowing the action potential to be recorded [13]. While these dyes are very sensitive and have faster dynamics, they are harder to specifically express in areas of interest. For example, these dyes indiscriminately label internal and plasma membranes, making it harder to decipher information from the membrane of interest since there is more background noise from unwanted fluorescence in other areas of the cell [7].

Some of these issues are resolved by the use of genetically encoded voltage indicators (GEVIs) [12, 15, 36]. GEVIs can be expressed more specifically, targeting certain types of cells [12, 15]. Recordings of neuronal action potentials using GEVIs have been shown [37, 38]. In addition, *in vivo* imaging with live animals has been demonstrated [12, 39, 40]. Furthermore, these indicators have fast response times and are sensitive, which enables the recording of faster action potential dynamics.

Despite the benefits presented by fluorescent recording, these methods also share a few limitations. As these methods are based on fluorescence, they suffer from photobleaching, which is when a fluorescent molecule ceases to emit light after some period of constant excitation [8, 12]. This can limit the recording duration as bleached reporter molecules cannot be used in recording. Fluorescent methods can also suffer from phototoxicity, which can damage the specimens [1, 12]. For example, the photochemical reactions involved in fluorescence can generate harmful free radicals which can break covalent bonds in molecules,

causing irreversible harm to vital cellular components such as proteins or DNA [41]. Finally, concerns remain about the effects that the introduction of fluorescent reporters can have on the membrane's intrinsic electrical properties [1, 12]. For these reasons, researchers have also sought out label-free methods for the recording of electrical activity in cells.

2.3.2 Label-free optical recording of action potentials

Light can be used to detect the intrinsic changes in cells that accompany action potentials or to monitor how the extracellular potentials affect materials placed near the cells [12]. These methods are label-free as they do not rely on the signals from any type of fluorescent indicator. Label-free methods are generally non-perturbative to cells, and therefore are capable of recording bioelectric signals for longer durations. They also offer greater spatial flexibility than electrode-based methods.

One way to record action potentials is to measure the structural changes of a cell with time. For example, the volume of a cell can change as the transmembrane potential changes. This can be recorded using atomic force microscopy (AFM). In AFM, a tip is mounted under a cantilever and placed in contact with the cell membrane. As the volume of the cell changes, the tip and the cantilever move in response. By monitoring the movement of the cantilever using a laser beam, the structural changes of a cell can be recorded. In one experiment, AFM was used to record membrane movement of HEK293 cells in response to an applied voltage [16]. Recordings of action potentials using AFM have also been demonstrated [42].

Another label-free approach is to detect intrinsic optical changes in the cells that accompany action potentials. Raman spectroscopy uses visible (or near-infrared) light to excite a sample and measures the inelastically scattered light, which contains small energy shifts corresponding to the vibrational modes of the molecules in the sample. Thus Raman spectroscopy can be used to measure molecular spectra and identify the distinctive signals from certain chemical species [12]. Stimulated Raman Scattering (SRS), a variant of Raman spectroscopy, is a non-linear optical technique that uses two laser beams to greatly amplify the scattering signal. SRS has been used to detect the action potential in a mouse neuron with a SNR of ~ 3.6 by recording the intensity changes of the Raman shift at $\sim 2930\,\mathrm{cm}^{-1}$ [12, 43].

It is also possible to record action potentials using materials that change their optical properties in response to an applied electrical signal. One approach uses nitrogen vacancy (NV) centers in diamond to detect the small magnetic fields that are generated by currents produced as a result of action potential propagation [17]. In this experiment, the action potentials in worm and giant squid axons were recorded. However, since the currents produced by action potentials are very small, the SNR of a single recording is ~ 1.2 and averaging of hundreds of individual recordings is needed to improve the SNR [12].

Electrochromic optical recording (ECORE), the subject of this dissertation, is another approach that utilizes the changing optical properties of materials in response to electrical activity to record action potentials. In the next chapter, we explore the theory of ECORE and the experiments that have been performed using this method.

Chapter 3

Theory

3.1 Introduction to Electrochromic Optical Recording (ECORE)

Electrochromic optical recording uses electrochromic materials to record extracellular action potentials. If excitable cells are placed in proximity to a suitable electrochromic material, the optical properties of the material will change in response to the action potential, and these changes can be detected by monitoring how light interacts with the material over time. This concept is depicted in Fig. 1.1.

All ECORE methods use this concept to record bioelectric signals. However, a few different variations have been developed over the past few years with the goal of improving sensitivity to smaller electrical signals. We now discuss some theoretical concepts necessary to understand how ECORE works before describing the different existing variants of ECORE.

3.2 Electrochromism

Electrochromism is the reversible change in color of a material in response to an applied voltage. This property of electrochromic materials is generally driven by redox (reduction-oxidation) processes [44, 45].

In a redox process, electrons are transferred between two or more chemical species (atoms, molecules, or ions). These reactions occur when electron transfer is thermodynamically favorable under the given conditions, or when external conditions are applied that make the reaction favorable, such as the application of an external voltage. In a redox process, species that gain electrons are said to be reduced, while those that lose electrons are oxidized. In many electrochromic materials, the observed color change arises from differences in the optical absorption spectra between the different redox states of the material.

There are many different types of electrochromic materials, and they have found many uses, including as displays and as “smart windows”, which can be made brighter or dimmer

on the application of some voltage. The different types of electrochromic materials can be classified by the solubility in their oxidized and reduced states [44]:

- Type I: These are soluble in both their oxidized and reduced states
- Type II: These are only soluble in either the oxidized or the reduced state
- Type III: These are insoluble in both their oxidized and reduced states

Type III electrochromic materials are common as the material can be deposited as a thin film. Once deposited, the film does not change phase and can be repeatedly used by applying a potential difference across it. The deposition of these electrochromic thin films onto a substrate usually requires an electrode. Given that electrochromic materials are desired for their interaction with light, these electrodes are usually optically transparent materials that allow light through to the electrochromic film. A popular choice of electrode is tin-doped indium oxide (In_2O_3:Sn), commonly referred to as indium tin oxide (ITO) [44]. ITO has a high transmittance in the visible range of the electromagnetic spectrum, is electrically conductive, and can be easily coated onto different types of glass substrates.

3.2.1 Suitable electrochromic materials

While there is a large variety of electrochromic materials, not all are suitable for the recording of bioelectric potentials. Many materials are toxic to cells or are unable to function properly under cellular conditions. We use the word biocompatible to refer to electrochromic materials that can be used in cellular environments. Another requirement for biocompatible electrochromic materials is that they can be used as films, which the cells can be deposited onto, instead of as solutions. Therefore, type III materials are best for use with cells (if they are also biocompatible). We now briefly discuss a few biocompatible electrochromic materials and the underlying mechanisms that are responsible for their electrochromic behavior.

One of the oldest known materials to exhibit electrochromism is Prussian blue, a pigment discovered more than 300 years ago and still widely used today, whose electrochromic properties have been extensively studied since 1978 [44, 46, 47]. Prussian blue is the name given to iron(III) hexacyanoferrate(II), $Fe_4{}^{III}[Fe^{II}(CN)_6]_3$, which has an intense blue color that is attributed to intervalence charge transfer (IVCT) between the mixed-valence iron centers in the compound. Reduction of Fe^{3+} to Fe^{2+} disrupts this mixed-valence state and causes the color to change from blue to colorless [44, 47]. This reduction can happen, for example, via the following reaction [47]:

$$Fe_4{}^{III}[Fe^{II}(CN)_6]_3 + 4K^+ + 4e^- \rightleftharpoons K_4Fe_4{}^{II}[Fe^{II}(CN)_6]_3\,, \tag{3.1}$$

where the K^+ ions in the electrolyte compensate the charge. The identity of the compensating cation can have a significant impact on the ability of Prussian blue to exhibit electrochromic behavior [47].

Metal oxides, such as iridium(IV) oxide, are often electrochromic due to the presence of multiple accessible oxidation states in the transition metal centers. In some cases, optical modulation can be described in terms of IVCT between different oxidation states [44], with each state exhibiting distinct optical absorption spectra. In iridium(IV) oxide, electrochromism arises from reversible redox transitions between Ir^{4+} and Ir^{3+}, often accompanied by ion insertion from the electrolyte. The more oxidized state typically exhibits strong optical absorption and appears blue, while the reduced state is significantly less absorbing and appears colorless.

Another promising class of electrochromic materials are conjugated conducting polymers. These polymers consist of resonance-stabilized aromatic units, such as thiophene derivatives, which form a π-conjugated backbone that allows delocalization of charge carriers along the backbone. One such electrochromic polymer is poly(3,4-ethylenedioxythiophene) (PEDOT), which is composed of monomers of 3,4-ethylenedioxythiophene (EDOT). PEDOT is often used in its conducting oxidized state, with positive charge carriers delocalized along the polymer backbone. Because it is positively charged, PEDOT requires a counterion for charge neutrality. The polymer poly(styrene sulfonate) (PSS) is typically used for this purpose, and also improves the water solubility and processability of PEDOT [44, 47]. Thus, for practical applications, the form of PEDOT used most widely is poly(3,4-ethylenedioxythiophene) polystyrene sulfonate (PEDOT:PSS). We will hereafter refer to this compound simply as PEDOT, given that the electrochromic properties arise primarily from the PEDOT backbone.

The electrochromism of PEDOT and other conjugated conducting polymers arises from changes in the electronic structure of the π-conjugated backbone, which affects how the polymer absorbs light. In PEDOT, the twisting of the polymer can reduce the effective conjugation length along the backbone, promoting localization of charge carriers. This forms distinct allowed localized charge states, called polarons and bipolarons [47], and their creation forms intermediate energy states in the bandgap of the neutral polymer. Optical absorption can then occur via transitions involving these polaron states, allowing absorption of lower-energy light in the conducting polymer [47]. The application of an electrical potential to PEDOT changes its doping level, thereby modifying the population of polarons and bipolarons, and thus altering its optical absorption, resulting in electrochromism.

Other polymers based on EDOT can also be used for their electrochromic properties. For example, P(OE3)-E (hereafter referred to simply as PProDOT), which is an alternating copolymer of unsubstituted EDOT and oligoether functionalized ProDOT [20], has been used for the detection of bioelectric signals. We will discuss these materials more in the context of ECORE later.

3.3 Interaction of light with material interfaces

3.3.1 Light at the interface of two materials

To record potential changes, changes in the optical properties of the electrochromic materials must be probed over time using light.

Light is composed of oscillating electric ($\mathbf{E}(\mathbf{r},t)$) and magnetic ($\mathbf{B}(\mathbf{r},t)$) fields that are consistent with Maxwell's equations [48]. We will focus our attention on the electric fields. Although Maxwell's equations admit many possible electromagnetic field solutions, one of the most useful is the plane-wave solution of the form

$$\mathbf{E}(\mathbf{r},t) = \mathbf{E}_0 e^{i(\mathbf{k}\cdot\mathbf{r}-\omega t)}\,, \tag{3.2}$$

where $\mathbf{r}$ is some location in space, t is some point in time, $\mathbf{E}_0$ is the magnitude and direction (polarization) of the wave, $\mathbf{k}$ is the wave vector, and ω is the frequency. Any arbitrary wave can be broken down into a sum of plane waves, so there is no loss in generality by focusing on just plane waves.

The frequency ω of the wave is given by

$$\omega = \frac{2\pi c}{\lambda_0}\,, \tag{3.3}$$

where λ_0 is the wavelength of light in vacuum and c is the speed of light in vacuum.

The wave vector $\mathbf{k}$ describes the spatial frequency and direction of propagation of the wave. It can be broken down as

$$\mathbf{k} \equiv k\hat{\mathbf{u}}\,, \tag{3.4}$$

where k is the magnitude of the wave vector and $\hat{\mathbf{u}}$ is the unit vector in the direction of the wave vector. In an isotropic, homogeneous, and nonconducting medium, the magnitude of the wave vector can be written as

$$k = \frac{n(\omega)\omega}{c}\,, \tag{3.5}$$

where $n(\omega)$ is the index of refraction of material, a frequency-dependent quantity that characterizes the optical properties of the material. For notational simplicity, we will drop the frequency-dependent notation and write $n \equiv n(\omega)$. In general, the refractive index is complex:

$$n \equiv n_\mathrm{r} + i\kappa\,, \tag{3.6}$$

where n_r and κ are the real and imaginary parts of the refractive index, respectively. We can understand the roles that these two parts have to play in the propagation of a wave by substituting the above expression in the electric field from eq. (3.2):

$$\mathbf{E}(\mathbf{r},t) = \mathbf{E}_0 \exp(i(k\hat{\mathbf{u}}\cdot\mathbf{r}-\omega t)) = \mathbf{E}_0 \exp\left[-\frac{\kappa\omega}{c}\hat{\mathbf{u}}\cdot\mathbf{r}\right] \exp\left[i\left(\frac{n_\mathrm{r}\omega}{c}\hat{\mathbf{u}}\cdot\mathbf{r}-\omega t\right)\right]\,. \tag{3.7}$$

The second exponential in the expression above — which contains only the real part (n_r) of the index — shows the normal, oscillatory behavior of a wave. Specifically, we see that

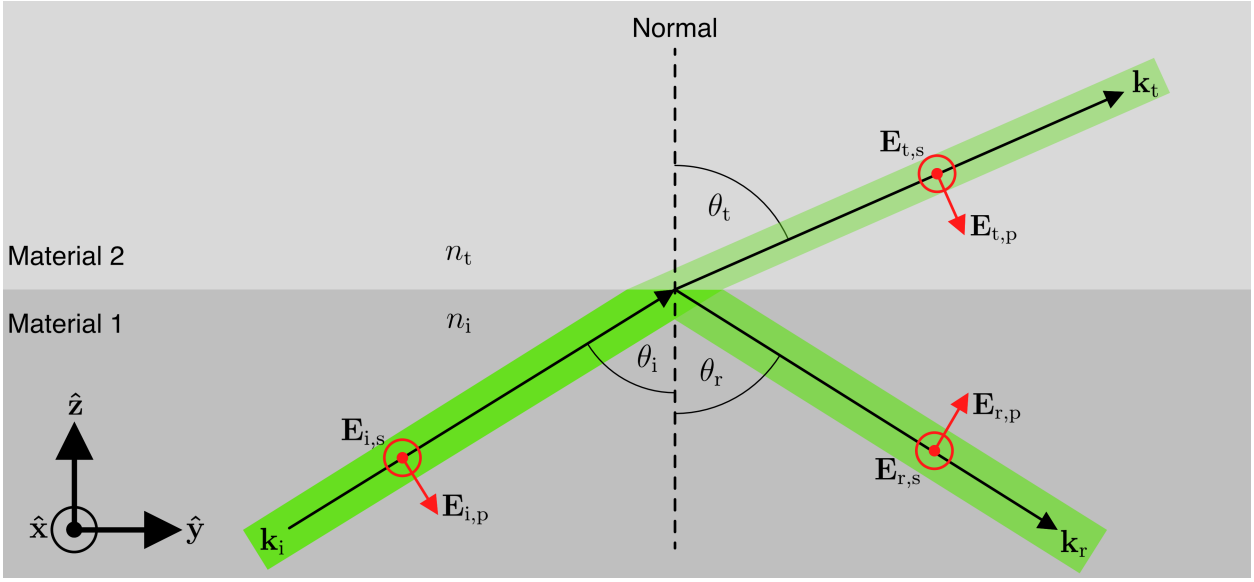

Figure 3.1: Light is incident on the boundary of two materials of different indices with an incident angle θ_i. Some light is reflected back into material 1 with an angle $\theta_r = \theta_i$. Some light is also transmitted into material 2 with an angle θ_t. The wave vectors $\mathbf{k}$ of the incident, reflected, and transmitted light are shown. The various electric field components $\mathbf{E}$ are also shown (red). The unit vectors of the coordinate system are drawn at the bottom left, with the positive x direction pointing out of the page.

n_r alters the spatial frequency of the light in that material. On the other hand, the first exponential shows a decay of the field magnitude if $\kappa > 0$, describing absorption of light by the material. Conversely, in active materials such as those used in lasers, $\kappa < 0$ represents gain (i.e., exponential growth of the field). Thus, the imaginary part of the refractive index characterizes the exponential decay or growth of light as it propagates through the material [48, 49], and is zero for a lossless material.

When light is incident on the interface of two semi-infinite materials (i.e., the materials are assumed to extend out to infinity in either direction of the interface), it is partially reflected and partially transmitted. This situation is depicted in Fig. 3.1, where the index of the first material (where the light is incident) is n_i, while the index of the second material (where light is transmitted) is n_t. Fig. 3.1 also shows the wave vectors of the incident, reflected, and transmitted waves, as well as the electric field components of each wave. The electric field components that lie in the plane of incidence constitute P-polarized light, while those that are perpendicular to the plane of incidence constitute S-polarized light.

The electric fields can be connected by employing boundary conditions imposed by Maxwell's equations [50]. These connections impose certain conditions on the directions of the fields (and the wave vectors). For the reflected light, the angle of reflection must be

equal to the angle of incidence, i.e. $\theta_\mathrm{r} = \theta_\mathrm{i}$. As for the transmission of light into the second material (known as refraction), the angles are related by Snell's law [50]:

$$n_\mathrm{i} \sin\theta_\mathrm{i} = n_\mathrm{t} \sin\theta_\mathrm{t} \,. \tag{3.8}$$

The boundary conditions also impose certain relationships between the magnitudes of the electric fields shown in Fig. 3.1. These relationships are known as the Fresnel coefficients [50]:

$$r_\mathrm{s} \equiv \frac{|\mathbf{E}_\mathrm{r,s}|}{|\mathbf{E}_\mathrm{i,s}|} = \frac{n_\mathrm{i}\cos\theta_\mathrm{i} - n_\mathrm{t}\cos\theta_\mathrm{t}}{n_\mathrm{i}\cos\theta_\mathrm{i} + n_\mathrm{t}\cos\theta_\mathrm{t}} \tag{3.9}$$

$$t_\mathrm{s} \equiv \frac{|\mathbf{E}_\mathrm{t,s}|}{|\mathbf{E}_\mathrm{i,s}|} = \frac{2n_\mathrm{i}\cos\theta_\mathrm{i}}{n_\mathrm{i}\cos\theta_\mathrm{i} + n_\mathrm{t}\cos\theta_\mathrm{t}} \tag{3.10}$$

$$r_\mathrm{p} \equiv \frac{|\mathbf{E}_\mathrm{r,p}|}{|\mathbf{E}_\mathrm{i,p}|} = \frac{n_\mathrm{i}\cos\theta_\mathrm{t} - n_\mathrm{t}\cos\theta_\mathrm{i}}{n_\mathrm{i}\cos\theta_\mathrm{t} + n_\mathrm{t}\cos\theta_\mathrm{i}} \tag{3.11}$$

$$t_\mathrm{p} \equiv \frac{|\mathbf{E}_\mathrm{t,p}|}{|\mathbf{E}_\mathrm{i,p}|} = \frac{2n_\mathrm{i}\cos\theta_\mathrm{i}}{n_\mathrm{i}\cos\theta_\mathrm{t} + n_\mathrm{t}\cos\theta_\mathrm{i}} \,, \tag{3.12}$$

where the subscripts s and p represent S- and P-polarized light, respectively. From these Fresnel coefficients, the reflected and transmitted power ratios (the reflectance R and transmittance T, respectively) can also be found. As the power of light is proportional to the square of the electric field amplitude, the reflectances are

$$R \equiv |r|^2 \,. \qquad \text{(S- or P-polarized)} \tag{3.13}$$

On the other hand, the transmittances are not simply the squared absolute values of their respective transmission amplitudes, i.e., $T \neq |t|^2$. Instead, we have to take into account the fact that the transmitted light is in a different material and that the propagation direction of the energy will therefore change. Thus, the transmittances are [49, 50]:

$$T = \frac{\mathrm{Re}\,(n_\mathrm{t}\cos\theta_\mathrm{t})}{\mathrm{Re}\,(n_\mathrm{i}\cos\theta_\mathrm{i})}|t|^2 \,. \qquad \text{(S- or P-polarized)} \tag{3.14}$$

Using Snell's law (eq. (3.8)) and the Fresnel coefficients (eqs. (3.9) to (3.12)), we can explore the behavior of the refracted light. We will consider two cases for different types of refractive indices.

3.3.1.1 If both materials have real refractive indices

Let's assume that the two materials have only real indices of refraction. Then, if $n_\mathrm{t} > n_\mathrm{i}$, we can see from eq. (3.8) that the light will always be refracted with some angle $\theta_\mathrm{t} < \theta_\mathrm{i}$.

On the other hand, if $n_\mathrm{i} > n_\mathrm{t}$, then varying the incident angle θ_i can result in different outcomes. If $(n_\mathrm{i}/n_\mathrm{t})\sin\theta_\mathrm{i} < 1$, then $\theta_\mathrm{t} < 90°$, and the light will be transmitted into material

2. However, if $(n_\mathrm{i}/n_\mathrm{t})\sin\theta_\mathrm{i} = 1$, then $\theta_\mathrm{t} = 90°$, and the transmitted light continues along the surface of the two materials. In this scenario, the incident angle $\theta_\mathrm{i} = \sin^{-1}(n_\mathrm{t}/n_\mathrm{i})$ is known as the critical angle θ_c.

For the scenario in which the critical angle is exceeded, i.e. if $(n_\mathrm{i}/n_\mathrm{t})\sin\theta_\mathrm{i} > 1$, we can better understand what happens to the incident light by starting with Snell's law and using the fact that $\theta_\mathrm{i} > \theta_\mathrm{c}$. We can employ the trigonometric identity

$$\sin^2\theta + \cos^2\theta = 1 \tag{3.15}$$

to write

$$\cos\theta_\mathrm{t} = \sqrt{1-\sin^2\theta_\mathrm{t}} = \sqrt{1-\frac{n_\mathrm{i}^2}{n_\mathrm{t}^2}\sin^2\theta_\mathrm{i}}\,. \tag{3.16}$$

However, since $(n_\mathrm{i}/n_\mathrm{t})\sin\theta_\mathrm{i} > 1$, this becomes

$$\cos\theta_\mathrm{t} = i\sqrt{\frac{n_\mathrm{i}^2}{n_\mathrm{t}^2}\sin^2\theta_\mathrm{i} - 1}\,. \tag{3.17}$$

We can now substitute this expression into the expressions for r_s or r_p in eqs. (3.9) and (3.11) to get

$$r_\mathrm{s} = \frac{n_\mathrm{i}\cos\theta_\mathrm{i} - in_\mathrm{t}\sqrt{\frac{n_\mathrm{i}^2}{n_\mathrm{t}^2}\sin^2\theta_\mathrm{i} - 1}}{n_\mathrm{i}\cos\theta_\mathrm{i} + in_\mathrm{t}\sqrt{\frac{n_\mathrm{i}^2}{n_\mathrm{t}^2}\sin^2\theta_\mathrm{i} - 1}} \tag{3.18}$$

and

$$r_\mathrm{p} = -\frac{n_\mathrm{t}\cos\theta_\mathrm{i} - in_\mathrm{i}\sqrt{\frac{n_\mathrm{i}^2}{n_\mathrm{t}^2}\sin^2\theta_\mathrm{i} - 1}}{n_\mathrm{t}\cos\theta_\mathrm{i} + in_\mathrm{i}\sqrt{\frac{n_\mathrm{i}^2}{n_\mathrm{t}^2}\sin^2\theta_\mathrm{i} - 1}}\,. \tag{3.19}$$

Note that eq. (3.18) can be written in the simplified form

$$r_\mathrm{s} = \frac{a-ib}{a+ib} \tag{3.20}$$

with $a \equiv n_\mathrm{i}\cos\theta_\mathrm{i}$ and $b \equiv n_\mathrm{t}\sqrt{\frac{n_\mathrm{i}^2}{n_\mathrm{t}^2}\sin^2\theta_\mathrm{i} - 1}$. We first write r_s in the standard form for a complex number:

$$r_\mathrm{s} = \frac{a-ib}{a+ib} = \frac{(a-ib)(a-ib)}{(a+ib)(a-ib)} = \frac{a^2-2iab-b^2}{a^2+b^2} = \frac{a^2-b^2}{a^2+b^2} + i\left(-\frac{2ab}{a^2+b^2}\right)\,. \tag{3.21}$$

Now, we find the magnitude of r_s:

$$\begin{aligned} |r_\mathrm{s}| &= \sqrt{\left(\frac{a^2-b^2}{a^2+b^2}\right)^2 + \left(-\frac{2ab}{a^2+b^2}\right)^2} = \sqrt{\frac{a^4-2a^2b^2+b^4}{(a^2+b^2)^2} + \frac{4a^2b^2}{(a^2+b^2)^2}} \\ &= \sqrt{\frac{a^4+2a^2b^2+b^4}{(a^2+b^2)^2}} = \sqrt{\frac{(a^2+b^2)^2}{(a^2+b^2)^2}} = \sqrt{1} = 1\,. \end{aligned} \tag{3.22}$$

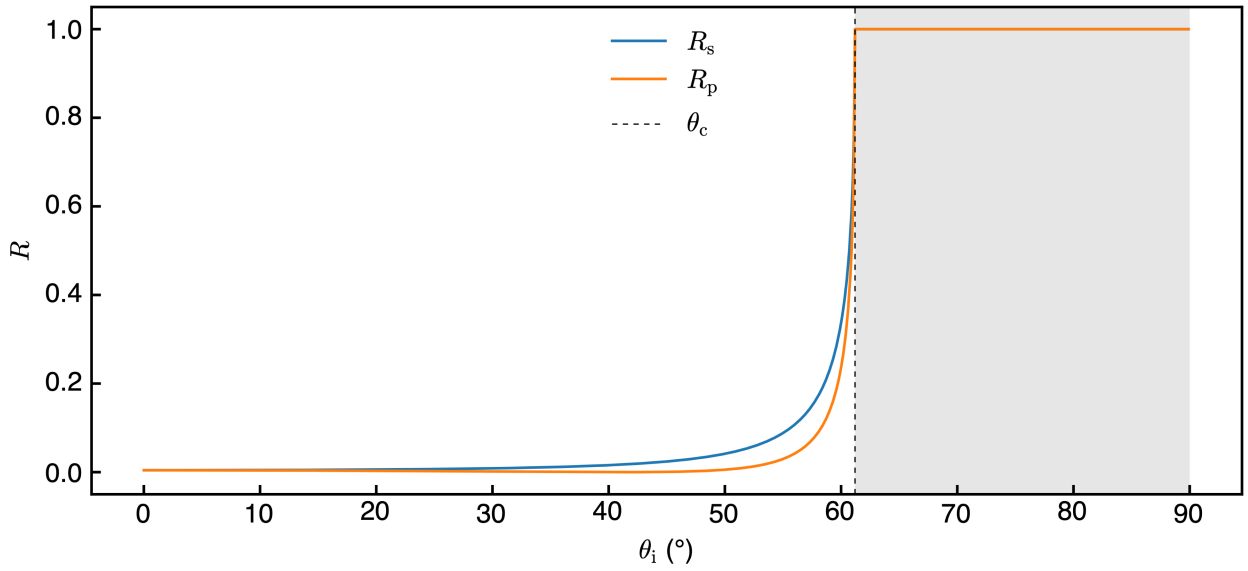

Figure 3.2: R_s and R_p for light going from glass ($n_i = 1.518$) into an aqueous solution ($n_t = 1.33$) at different angles of incidence (θ_i). The critical angle $\theta_c = 61.2°$ for this interface is shown as the dashed black line. At and beyond the critical angle, total internal reflection occurs (shaded region).

That is, the magnitude of the reflected S-polarized wave is the same as the incident S-polarized wave. Similar analysis for r_p (eq. (3.19)) shows that $|r_p| = 1$. From eq. (3.13), we therefore also have $R_s \equiv |r_s|^2 = 1$ and $R_p \equiv |r_p|^2 = 1$. In other words, when $n_i > n_t$ and $\theta_i > \theta_c$, all incident light power is reflected back into the first material. This phenomenon is called total internal reflection (TIR). A common case in microscopy is when light passes from glass ($n_i = 1.518$) into an aqueous solution ($n_t = 1.33$). For this case, the behavior of R_s and R_p across all incidence angles is shown in Fig. 3.2. The onset of TIR is clear beyond the critical angle of 61.2° for this system.

While all of the incident light power is reflected at supercritical angles, there are still waves that exist at the boundary in material 2. These can be understood by looking at the electric field in the second material. From Fig. 3.1, we can write the transmitted wave vector as

$$\mathbf{k}_t = k_t(\hat{\mathbf{y}} \sin\theta_t + \hat{\mathbf{z}} \cos\theta_t)\,. \tag{3.23}$$

Inserting this into eq. (3.2), the exponential factor for the transmitted waves (S or P) becomes

$$e^{i\mathbf{k}_t \cdot \mathbf{r}} = \exp\left[ik_t(y \sin\theta_t + z \cos\theta_t)\right]. \tag{3.24}$$

In particular, it is interesting to look at the behavior of the electric field in the $\hat{\mathbf{z}}$ direction, i.e., the direction normal to the interface. This is governed by the z term in the equation

above ($\exp(ik_t z\cos\theta_t)$). Using eq. (3.17) this becomes

$$\exp(ik_t z\cos\theta_t) = \exp\left(i^2 k_t z\left(\sqrt{\frac{n_i^2}{n_t^2}\sin^2\theta_i - 1}\right)\right) = \exp\left(-k_t z\left(\sqrt{\frac{n_i^2}{n_t^2}\sin^2\theta_i - 1}\right)\right). \tag{3.25}$$

That is, because $\cos\theta_t$ is imaginary for supercritical angles ($\theta_i > \theta_c$), there is an exponential decrease in the electric field amplitude of the transmitted wave moving away from the interface. On the other hand, the y term in eq. (3.24) does not show this behavior as $\sin\theta_t$ is real from Snell's law. Thus the transmitted field is oscillatory in the $\hat{\mathbf{y}}$ direction and decreases exponentially in the $\hat{\mathbf{z}}$ direction. This phenomenon is called evanescence and the wave is termed the evanescent wave. The behavior of this wave is consistent with our earlier observation that all of the incident light power is reflected. This is because the evanescent wave does not carry energy into the second material, but rather along the interface of the two materials [50].

The exponential decay of the field amplitude in the $\hat{\mathbf{z}}$ direction can be characterized further. If, instead of the field amplitude, we look at the light intensity (equivalently, the power), then the intensity along the $\hat{\mathbf{z}}$ direction can be written as

$$I(z) = I_0 e^{-z/d}, \tag{3.26}$$

where I_0 is the intensity of the light at the interface and d is the penetration depth of the evanescent field. Comparing the above equation with eq. (3.25), we can write the expression for d explicitly:

$$d = \frac{1}{\left(2k_t\left(\sqrt{\frac{n_i^2}{n_t^2}\sin^2\theta_i - 1}\right)\right)} = \frac{\lambda_0}{4\pi(\sqrt{n_i^2\sin^2\theta_i - n_t^2})}. \tag{3.27}$$

Note that the factor of 2 appears due to the fact that eq. (3.25) describes the field amplitude, and must be squared to describe the intensity instead. As an example, for light of wavelength $\lambda_0 = 500\,\text{nm}$ incident at $\theta_i = 65°$ at the glass-water interface considered earlier in this section ($n_i = 1.518$, $n_t = 1.33$), the evanescent field depth is $d = 110\,\text{nm}$. In general, the evanescent field depth is on the order of the wavelength used.

The small evanescent field depth can be utilized in applications involving the recording of fluorescent light. For example, in total internal reflection fluorescence (TIRF) microscopy, the evanescent wave can be used to excite fluorescent molecules in a sample. Typically, illumination of a sample at subcritical incident angles transmits the excitation light through the sample, exciting all fluorescent molecules in its path. This can lead to high background noise due to the illumination of fluorophores across a large depth of field. However, in TIRF microscopy, fluorescence is restricted to a thin layer of the sample closest to the TIR interface. This allows for brighter, higher SNR images of a very small section of the available fluorescent molecules in the entire sample.

3.3.1.2 If material 2 has a complex refractive index

The Fresnel coefficients (eqs. (3.9) to (3.12)) and Snell's law (eq. (3.8)) remain valid for complex refractive indices. We consider the case where the imaginary part of the refractive index of material 2 is nonzero. Specifically, we consider an absorptive second material, where $\kappa_t > 0$. This is also a common situation in microscopy, where light may be heading from glass (or air) into an absorptive material, such as an electrochromic material.

To get an understanding of what happens to the transmitted field in this scenario, let's focus on Snell's law (eq. (3.8)). Now that n_t is complex, $\sin\theta_t$ is also complex, and eq. (3.16) shows us that $\cos\theta_t$ is complex (as opposed to purely imaginary in the case where n_t is real and the critical angle is exceeded). From eq. (3.23), we therefore find that the electric field in the $\hat{\mathbf{z}}$ direction is not only decaying (as it is in the case where n_t is real and light is incident at supercritical angles) but also oscillating. That is, we see that the transmitted electric field has both an evanescent and oscillatory nature. Thus some light will be transmitted into the second material, in contrast to the previous case where no light was transmitted. Light that is transmitted into the second material is then absorbed by the material, with the absorbed energy heating the material.

While it is possible to follow similar steps to those from the previous section to get relationships for r_s and r_p (and therefore R_s and R_p), these are now cumbersome due to the complex second index. Thus, we will use the Fresnel coefficients and Snell's law to computationally determine R_s and R_p for a given situation. To facilitate comparison with the previous section, let's look at the case where light is heading from glass ($n_i = 1.518$) into a material with an index $n_t = 1.33 + i\kappa_t$. To study the effect of κ_t on the reflectances, we will determine R_s and R_p for the cases $\kappa_t = 0.01$, $\kappa_t = 0.1$, and $\kappa_t = 1$. The results are shown in Fig. 3.3.

In the case of $\kappa_t = 0.01$ (solid lines in Fig. 3.3), we see that the reflectances are similar to those in the lossless case (Fig. 3.2). However, in this case, there is no sharp transition to TIR as is true for the lossless case. Instead, the reflectances gradually rise towards $R = 1$ but do not reach it for $\theta_i < 90°$. That is, all light is not reflected back into material 1 and instead transmits into material 2, where it is absorbed. We see that, even when κ_t is fairly small, there is a significant amount of light transmitted into the second material. As κ_t is increased to $\kappa_t = 0.1$ and $\kappa_t = 1$, more light is transmitted (and absorbed) in the second material, and less light is reflected. Thus, if the second material is absorptive, TIR is suppressed.

3.3.2 Interaction with a multilayer sample

The analysis of the previous section can be expanded to the situation where light encounters a sample containing multiple layers of material [49]. This situation is practically important as many experiments, including ECORE, are carried out with intermediate thin layers of materials between the two semi-infinite materials originally considered in the previous section.

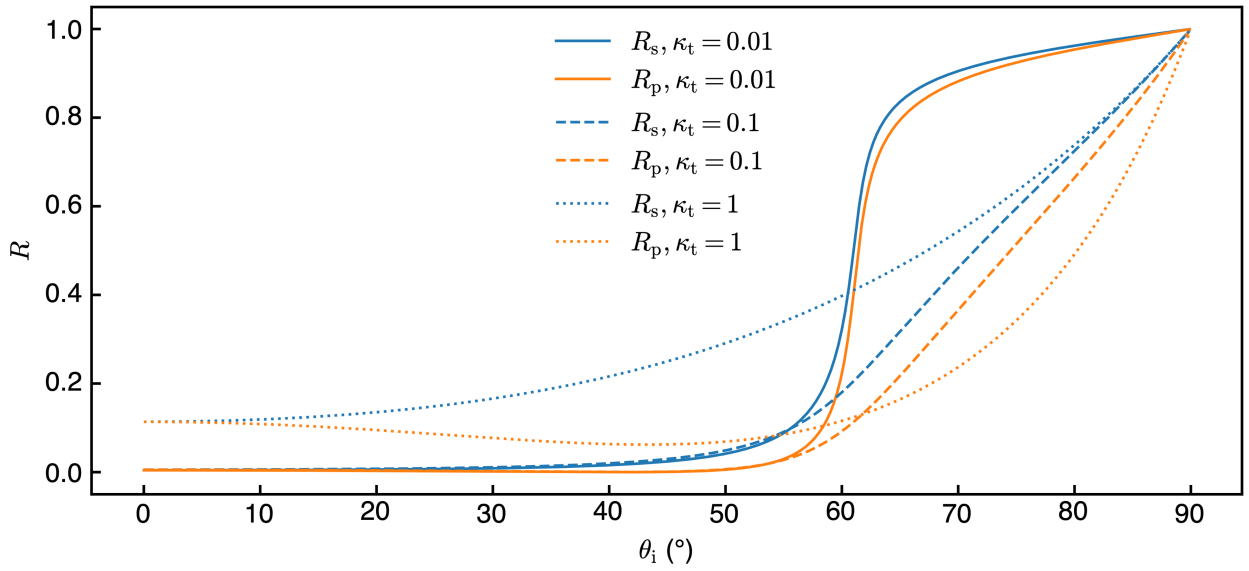

Figure 3.3: R_s and R_p for light going from glass ($n_\mathrm{i} = 1.518$) into a material with index $n_\mathrm{t} = 1.33 + i\kappa_\mathrm{t}$ at different angles of incidence (θ_i). Three different values of κ_t are plotted: $\kappa_\mathrm{t} = 0.01$, $\kappa_\mathrm{t} = 0.1$, and $\kappa_\mathrm{t} = 1$.

The general multilayer problem is illustrated in Fig. 3.4, where we have a stack of N layers of different materials, with the first and last materials being semi-infinite, while the intermediate layers are of a finite thickness. The magnitude of the "forward" moving electric field in each layer j is denoted by $E_{j\rightarrow}$ while the magnitude of the "backward" moving field is represented by $E_{j\leftarrow}$. Note that the arrows depicting the electric fields are not the directions of the electric fields themselves, but only show the association of the electric field magnitudes with the forward and backward moving plane waves in each material. Also note that we have dropped the subscripts s and p with the understanding that the electric fields $E_{j\rightarrow}$ and $E_{j\leftarrow}$ refer to either the S- or P-polarization, but not both at the same time (i.e., the two polarizations do not mix in the following analysis).

The electric field magnitudes $E_{0\rightarrow}$ and $E_{0\leftarrow}$ are taken to be at the interface of materials 0 and 1. All other field magnitudes $E_{j\rightarrow}$ and $E_{j\leftarrow}$ are defined at the interface of materials $j-1$ and j. For example, $E_{2\rightarrow}$ is the magnitude of the electric field of the plane wave moving away from the interface of material 1 and material 2.

Let's consider the magnitudes of the electric fields moving away from the interface of materials 0 and 1. The forward moving field at the boundary in material 1 is

$$E_{1\rightarrow} = r_{10}E_{1\leftarrow} + t_{01}E_{0\rightarrow}\,, \tag{3.28}$$

while the backward moving field at the boundary in material 0 is

$$E_{0\leftarrow} = r_{01}E_{0\rightarrow} + t_{10}E_{1\leftarrow}\,, \tag{3.29}$$

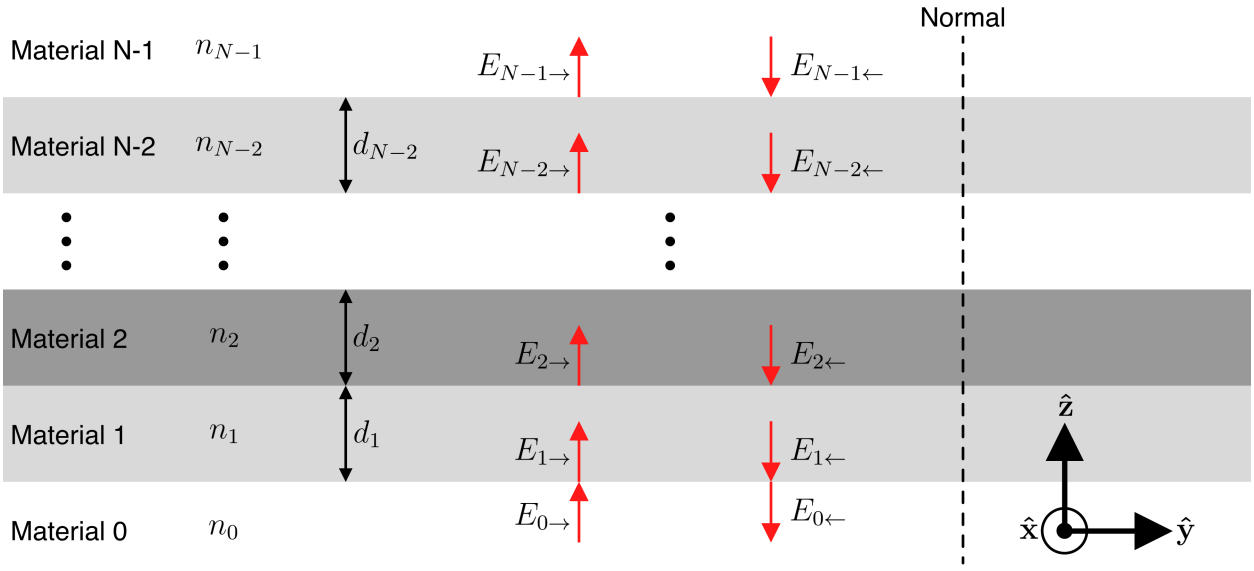

Figure 3.4: The general problem of light interacting with N layered materials. The materials numbered 0 and $N-1$ are semi-infinite, and there are $N-2$ materials of finite thickness between them. These $N-2$ materials have refractive indices n_j and thicknesses d_j.

where $r_{j,j\pm1}$ and $t_{j,j\pm1}$ are the Fresnel coefficients from eqs. (3.9) to (3.12). These relationships show that the field at any boundary is a superposition of the reflected and transmitted waves at that boundary.

For all other interfaces, we also need to take into account the thickness of each material. This is because we have only defined the fields at the top surface of each interface. For example, if we want to analyze the fields at the interface of materials 1 and 2, we only know the fields $E_{2\rightarrow}$ and $E_{2\leftarrow}$ at that interface. To get the forward and backward moving fields in material 1 at this interface, we need to take into account the phase that $E_{1\rightarrow}$ and $E_{1\leftarrow}$ collect as they pass through material 1. For this, we define the quantity δ_j as

$$\delta_j \equiv d_j k_{zj} \,, \tag{3.30}$$

where k_{zj} is the magnitude of the $\hat{\mathbf{z}}$ component of the forward traveling wave in material j [49]. The quantity δ_j captures the phase that accumulates from passing through layer j. The electric field magnitudes of the waves moving away from the interface of two materials j and $j+1$ are then

$$E_{j+1\rightarrow} = r_{j+1,j} E_{j+1\leftarrow} + t_{j,j+1}(E_{j\rightarrow} e^{i\delta_j}) \tag{3.31}$$

and

$$E_{j\leftarrow} e^{-i\delta_j} = (r_{j,j+1} E_{j\rightarrow} e^{i\delta_j}) + t_{j+1,j} E_{j+1\leftarrow} \,. \tag{3.32}$$

Using the fact that $r_{j,j+1} = -r_{j+1,j}$ and $t_{j,j+1}t_{j+1,j} - r_{j,j+1}r_{j+1,j} = 1$ [49], these equations can be written as

$$\begin{pmatrix} E_{j\rightarrow} \\ E_{j\leftarrow} \end{pmatrix} = M_j \begin{pmatrix} E_{j+1\rightarrow} \\ E_{j+1\leftarrow} \end{pmatrix} , \tag{3.33}$$

where

$$M_j = \begin{pmatrix} e^{-i\delta_j} & 0 \\ 0 & e^{i\delta_j} \end{pmatrix} \begin{pmatrix} 1 & r_{j,j+1} \\ r_{j,j+1} & 1 \end{pmatrix} \frac{1}{t_{j,j+1}} \tag{3.34}$$

for $j = 1, \ldots, N-2$. In most practical cases, such as in ECORE, we have some light entering the stack through material 0 and we are are interested in the total reflection amplitude r and the total transmission amplitude t. That is, we can define $E_{0\rightarrow} \equiv 1$, $E_{0\leftarrow} \equiv r$, $E_{N-1\rightarrow} \equiv t$, and $E_{N-1\leftarrow} \equiv 0$. Using repeated application of eq. (3.33), we can then write

$$\begin{pmatrix} 1 \\ r \end{pmatrix} = M \begin{pmatrix} t \\ 0 \end{pmatrix} = \begin{pmatrix} M_{00} & M_{01} \\ M_{10} & M_{11} \end{pmatrix} \begin{pmatrix} t \\ 0 \end{pmatrix} , \tag{3.35}$$

where

$$M \equiv \frac{1}{t_{01}} \begin{pmatrix} 1 & r_{01} \\ r_{01} & 1 \end{pmatrix} \prod_{j=1}^{N-2} M_j \, . \tag{3.36}$$

Once M is determined numerically (typically using computer programs for many layers), we can determine the total reflection and transmission amplitudes from eq. (3.35). The total reflection amplitude is

$$r = \frac{M_{10}}{M_{00}} , \tag{3.37}$$

while the total transmission amplitude is

$$t = \frac{1}{M_{00}} . \tag{3.38}$$

This process of determining the optical response of a multilayer system is known as the transfer matrix method [49].

3.3.2.1 Multilayer optical interactions in ECORE

A schematic of a typical sample used in ECORE experiments is shown in Fig. 3.5. ITO-coated glass is typically used as the substrate for these samples to aid in the deposition of the electrochromic material. A thin layer of the electrochromic material is then deposited onto the substrate. Finally, cells are cultured on top of the electrochromic thin film and are surrounded by cell culture medium. If cell-free experiments are performed, some aqueous ionic solution is used instead of the cell culture medium. Regardless, the top layer can be considered to primarily consist of water.

It is helpful to consider the refractive indices n_j and thicknesses d_j involved in an ECORE sample. More specifically, we will consider a sample using PEDOT as the electrochromic

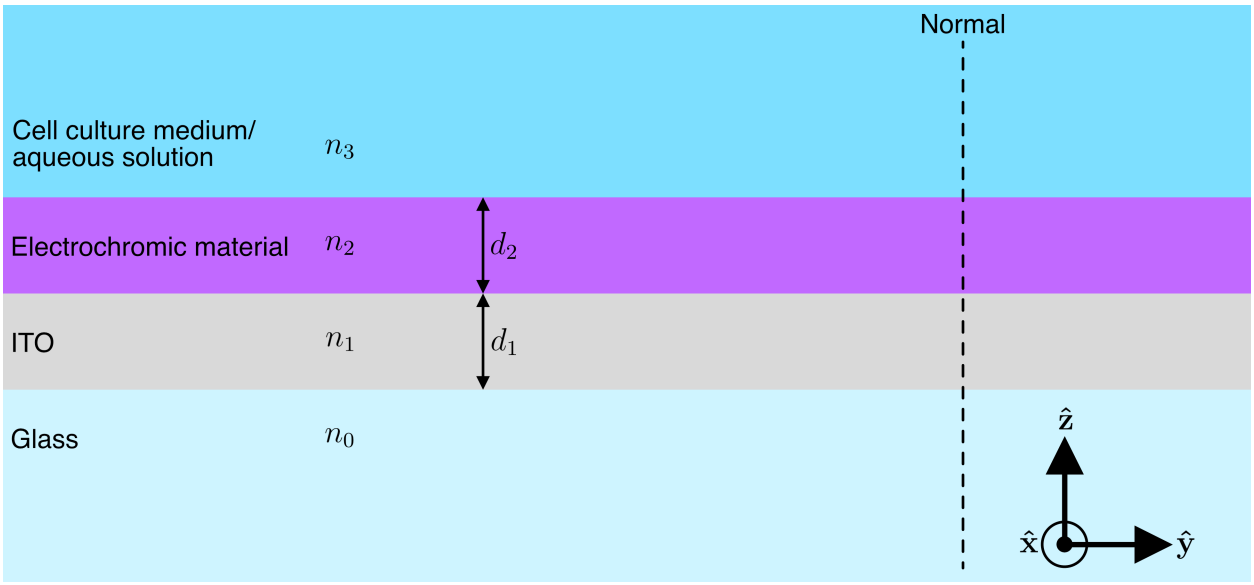

Figure 3.5: Schematic of a sample used in ECORE. These samples usually consist of 4 layers. Light enters into glass, before interacting with thin layers of ITO and the electrochromic material. The top of the sample consists of cell culture media (or some other aqueous solution in cell-free experiments).

Material	j	d_j	n_j
Glass	0	∞	1.518
ITO	1	30 nm	$1.84 + i0.061$
PEDOT	2	$\sim$50 nm	$1.4 + i\kappa_2$
Water	3	∞	1.33

Table 3.1: Typical ECORE sample layer parameters. The exact thickness of the PEDOT thin film is variable and depends on the deposition method. Furthermore, as the composition of PEDOT depends on the deposition method, κ_2 can be treated as an unknown quantity that can be determined using experimental data and comparing with simulations from the transfer matrix method.

material, which is common in ECORE experiments. The relevant values for such a sample are shown in table 3.1 [18]. We treat the first and last materials (glass and water, respectively) as semi-infinite since they are much thicker than the ITO and PEDOT layers.

With these typical sample values, we can start to analyze the behavior of light when it interacts with this multilayer sample. First, we can compute the critical angle for the

sample. Snell's law (eq. (3.8)) holds for each layer in the sample, i.e.

$$n_0 \sin\theta_0 = n_1 \sin\theta_1 = n_2 \sin\theta_2 = n_3 \sin\theta_3 \,. \tag{3.39}$$

The critical angle is determined by the incident medium (glass) and the medium with the lowest index (water). For this system the critical angle is thus

$$\theta_c = \arcsin\left(n_3/n_0\right) = 61.2^\circ \,. \tag{3.40}$$

ECORE experiments are typically operated so that TIR is achieved. Therefore, light is sent into glass so that it is incident on the first interface (glass/ITO) with $\theta_0 > 61.2^\circ$.

However, unlike the single interface problem considered in Fig. 3.1, the light does not only reflect once at the PEDOT/water interface. Instead, as we saw in eq. (3.31) and eq. (3.32), the electric field at each interface is produced by the collective interference of multiple reflections and transmissions. There is also absorption in the intermediate layers, as $\kappa_1 \neq 0$ and $\kappa_2 \neq 0$. Therefore, the light that eventually reflects and emerges from the bottom of the sample is composed of an infinite sum (in principle) of the multiple reflections at each interface, including any absorption that occurs in some layers. The transfer matrix method takes all of this into account and, given known sample parameters such as those in table 3.1, it can be used to compute the total reflectance of the sample using eq. (3.37) and the fact that $R = |r^2|$. Due to absorption in the ITO and PEDOT layers, we also see why it is critical to use both as thin films — thicker films would simply absorb too much of the incident light, leading to excess heat in the sample and a loss of signal at the detector.

We can also use the transfer matrix formalism to better understand the electrochromic response of the PEDOT film. This response results from the application of a voltage which changes the refractive index of PEDOT. Specifically, κ_2 is expected to change by an amount $\Delta\kappa_2$ in response to some applied voltage ΔV [18]. For changes in voltage where the response of the PEDOT is linear, we can write

$$\Delta\kappa_2 \approx \frac{d\kappa_2}{dV}\Delta V \,, \tag{3.41}$$

where $d\kappa_2/dV$ is determined experimentally [18]. Since the reflectance R from the sample is dependent on κ_2, we can also write

$$\Delta R \approx \frac{dR}{d\kappa_2}\Delta\kappa_2 \,, \tag{3.42}$$

where $dR/d\kappa_2$ can be determined using the transfer matrix method. Combining the two relationships above, we get

$$\Delta R \approx \frac{dR}{d\kappa_2}\frac{d\kappa_2}{dV}\Delta V \,. \tag{3.43}$$

Thus, we see that there is a clear and direct link between an applied voltage ΔV and the optical response demonstrated by the electrochromic sample ΔR. This allows for the detection of electrical signals using electrochromism, as first depicted in the schematic in Fig. 1.1.

3.4 Application of voltage signals to samples

The purpose of ECORE is to detect bioelectric signals. However, biological signals can be both small and hard to reproduce, given the diversity of cell types and cultures. To test and benchmark any ECORE setup, a voltage must be applied to the electrochromic material in a controlled and reproducible manner. This application of voltage signals is achieved through the use of a potentiostat. Once an ECORE setup has been verified to work with sufficiently small signals, it can then be used with cells.

3.4.1 Potentiostats

ECORE experiments use potentiostats to apply a voltage to the electrochromic thin film through a conducting ionic solution, which is meant to replicate the aqueous environmental conditions of cell culture media. Potentiostats are routinely used in experiments involving solutions as they provide a reliable way of applying a desired voltage signal to the sample. The key feature of potentiostats is that they employ three electrodes instead of two to overcome the limitations of voltage application through just two electrodes. The issue with two electrodes lies in the fact that electrode potentials are not constant in time and the potential drop between the electrodes is current-dependent. This means that the desired voltage cannot be applied reliably between the 2 electrodes and will fluctuate with time depending on the chemical and environmental conditions. The electrodes used in potentiostats play the following roles:

- Working electrode (WE): this is the main electrode of interest, where the potential is held at a given value compared to the reference electrode
- Reference electrode (RE): this is an electrode with a stable potential that draws negligible current. A commonly used reference electrode is a standard Ag/AgCl electrode
- Counter electrode (CE): this electrode completes the circuit by allowing current to flow between itself and the working electrode in a way that enables the working electrode to be held at the desired potential relative to the reference electrode

A basic schematic of a potentiostat is shown in Fig. 3.6(a). By simplifying the impedances on the interfaces of the electrodes as well as those in the solution, we can further reduce the schematic to the circuit diagram shown in Fig. 3.6(b). At the heart of the potentiostat is the operational amplifier (op-amp), which is used to maintain the desired applied voltage V_{app} between the WE and the RE. We can see this by analyzing the circuit diagram.

The output voltage of the op-amp is

$$V_{\text{out}} = A(V_+ - V_-) = A(V_{\text{app}} - V_{\text{RE}})\,, \tag{3.44}$$

where A is open-loop gain of the amplifier. Since the RE is connected to the input of the op-amp, it will draw negligible current and we can break down the full current over the two

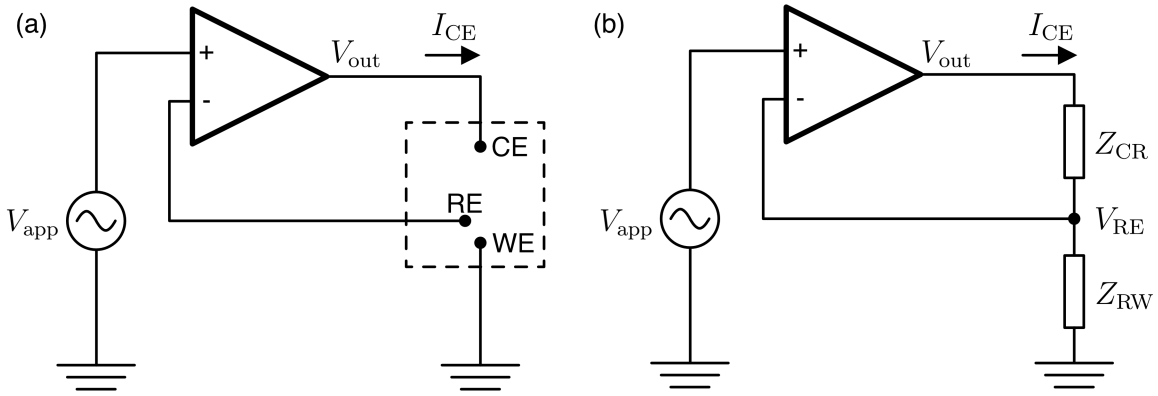

Figure 3.6: A simplified schematic of a potentiostat. (a) The applied potential V_{app} is generated by a function generator. The dashed box represents the liquid solution in which the 3 electrodes are placed (WE=working electrode, RE=reference electrode, CE=counter electrode). The potentiostat is designed in a way that makes current I_{CE} flow through the CE but no current flows through the RE. (b) The schematic in (a) can be drawn using this circuit diagram. All impedance between the CE and RE is represented by Z_{CR}, while all impedance between the RE and the WE is represented by Z_{RW}.

impedances. We have:

$$I_{\text{CE}} = \frac{V_{\text{out}}}{Z_{\text{CR}} + Z_{\text{RW}}} \tag{3.45}$$

and

$$I_{\text{CE}} = \frac{V_{\text{RE}}}{Z_{\text{RW}}} \,. \tag{3.46}$$

Combining the above equations, we get

$$V_{\text{RE}} = \left(\frac{Z_{\text{RW}}}{Z_{\text{CR}} + Z_{\text{RW}}} \right) V_{\text{out}} = AB(V_{\text{app}} - V_{\text{RE}}) \,, \tag{3.47}$$

where $B \equiv Z_{\text{RW}}/(Z_{\text{CR}} + Z_{\text{RW}})$. Simplifying the last equation, we get

$$V_{\text{RE}} = \left(\frac{AB}{1 + AB} \right) V_{\text{app}} \,. \tag{3.48}$$

As A is very large ($\sim 10^6$), and Z_{CR} and Z_{RW} are typically of the same order, $AB \gg 1$ and we have $V_{\text{RE}} = V_{\text{app}}$. Thus the desired voltage V_{app} can be reliably applied to the WE (relative to the RE) by getting current to flow through the CE to maintain this relationship.

In addition to the role they play in cell-free experiments with ECORE, potentiostats are also useful in the deposition of electrochromic materials where the deposition method involves the application of some voltage to deposit a material onto a conducting substrate, such as ITO-coated glass.

3.5 Signal detection

The extracellular potentials that ECORE aims to detect are very small, and therefore cause only very small changes in the optical properties of the electrochromic materials used. Thus every ECORE setup must have very sensitive detection electronics, which minimize noise and maximize the ability to detect small changes in the power of the light that interacts with the electrochromic material.

All ECORE experiments employ a differential signal detection scheme based on a balanced photodetector, which outputs the difference signal of two photodiodes [51]. Two light beams are used from the same light source — one of these is sent straight to one of the photodiodes, serving as a reference beam. The other beam is sent towards the sample, where it interacts with the electrochromic material and then lands on the second photodiode. This second beam carries the main signal of interest, and is therefore referred to as the signal beam.

In a balanced detector, if the light intensity falling on both photodiodes is the same, then any changes in one of the two beams will be amplified to produce a large output while any common-mode noise between the two beams will be suppressed. This helps identify any small, real differences between the beams while also reducing the noise. This type of detection is useful in ECORE as the reflectance changes at the sample are only expected to change the signal beam power in a very small way, while the reference beam power is expected to remain the same.

A simplified schematic of this detector is shown in Fig. 3.7. Light falls on the two photodiodes shown and the relative intensity can be changed to balance the power impinging on both diodes. Both photodiodes are reverse-biased, and produce a current when there is light falling on them. The current produced by each photodiode is given by

$$I_{\mathrm{pd}} = \mathcal{R} P_{\mathrm{pd}} \,, \tag{3.49}$$

where $\mathcal{R}$ is the responsivity of the photodiode (set by its quantum efficiency) and P_{pd} is the power of light falling on it. These currents are shown as arrows in Fig. 3.7. The node between the two photodiodes is connected to the inverting input of an op-amp (AD823, Analog Devices), while the non-inverting input is connected to ground. The output of the op-amp is connected back to the inverting input through a feedback resistor of resistance R_{f}. We can now determine how the circuit behaves by considering the currents involved as well as the operating principles of an op-amp.

The currents at the node can be summed to give

$$I_{\mathrm{f}} = I_1 - I_2 \,, \tag{3.50}$$

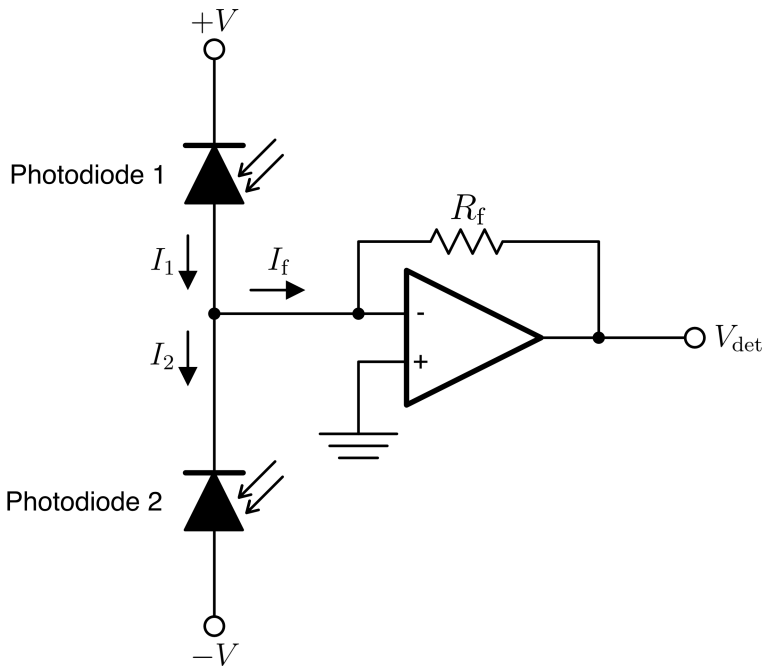

Figure 3.7: A simplified schematic of our balanced detector. The light levels on the two photodiodes are balanced so that the photocurrents from the diodes are initially equal (i.e. $I_1 = I_2$). If, however, the reference beam is kept unchanged while the signal beam changes due to the changing reflectance of the sample, then there will be a nonzero output voltage signal V_{det}.

where I_1 and I_2 are the photocurrents of the top and bottom photodiodes respectively. As the op-amp draws a negligible current at its inputs, I_{f} flows through the feedback resistor. Furthermore, since the two inputs of the op-amp are held at the same voltage, the entire voltage drop of V_{det} occurs across the feedback resistor, i.e. we have

$$V_{\mathrm{det}} = -I_{\mathrm{f}} R_{\mathrm{f}} \,. \tag{3.51}$$

Putting the above two equations together, along with the photocurrents of the two photodiodes, we have

$$V_{\mathrm{det}} = -R_{\mathrm{f}}(I_1 - I_2) = -\mathcal{R} R_{\mathrm{f}}(P_1 - P_2) = \mathcal{R} R_{\mathrm{f}}(P_2 - P_1) \,, \tag{3.52}$$

where the assumption has been made that the two photodiodes have the same responsivity $\mathcal{R}$. We see that the output voltage of the balanced detector is proportional to the difference of the powers falling on the two photodiodes of the photodetector, which is exactly the desired behavior of a balanced detector.

3.6 Previous ECORE experiments

Having discussed the theoretical aspects of electrochromic optical recording, we now briefly describe previously published ECORE setups.

3.6.1 Original ECORE

3.6.1.1 Experimental setup

A schematic depicting the original ECORE experiment [18, 47] is shown in Fig. 3.8. Laser light of wavelength 661 nm is first coupled into an optical fiber. The fiber serves as a spatial filter, transmitting only the fundamental transverse mode of the beam while rejecting higher-order modes. This results in an output beam that closely approximates a Gaussian profile, which has well-defined propagation properties that are desirable for subsequent stages of the experiment.

The output of the fiber is directed through a half-wave plate and a polarizer; the half-wave plate is used to rotate the polarization axis, and the polarizer then selects a well-defined linear polarization state. A second half-wave plate then rotates the polarization before the light enters a Wollaston polarizer. Wollaston polarizers use birefringent prisms to spatially separate orthogonal linear polarization components into two distinct beams. They are preferred over other polarizers due to their high extinction ratios, defined as the ratio of transmitted intensity in the desired polarization to that in the orthogonal polarization. By rotating the second half-wave plate, the relative intensities of the two output beams of the Wollaston polarizer can be changed. One output beam of the Wollaston polarizer is directed towards one photodiode of a balanced detector, serving as the reference beam in the setup.

The other beam (the signal beam) is directed to the sample via a lens which focuses the beam at the sample. The spot size of the focused light at the sample determines the probe size of the experiment [18]. In this experiment, the beam was determined to have a $1/e^2$ intensity radius of 28.4 µm. This makes the spot size similar to the size of a cardiomyocyte [18]. Therefore, the experiment records extracellular action potentials from whole cells.

The sample consists of a glass slide coated with a thin layer of ITO and a thin film of the electrochromic material (in cellular experiments, cells are also deposited above the electrochromic material). As we saw in a previous section, the reflections from the layers above the glass are required to probe the optical changes of the electrochromic material in response to an applied voltage. Thus, we want the light to be incident at the glass-ITO interface at large angles of incidence (for PEDOT we saw in eq. (3.40) that we need $\theta_\mathrm{i} > 61.2°$). Furthermore, the light must be transmitted from air (where the focusing lens is present) into the glass slide for these reflections to take place. However, from eq. (3.8), it is impossible for light to be incident on the bottom surface of the glass slide (i.e., at the air-glass interface) such that it transmits into the glass with an angle $> 61.2°$. Therefore, to transmit light from air into the sample at large angles, the sample is optically coupled to a glass equilateral prism using index-matching oil. The light then reflects from the multilayer

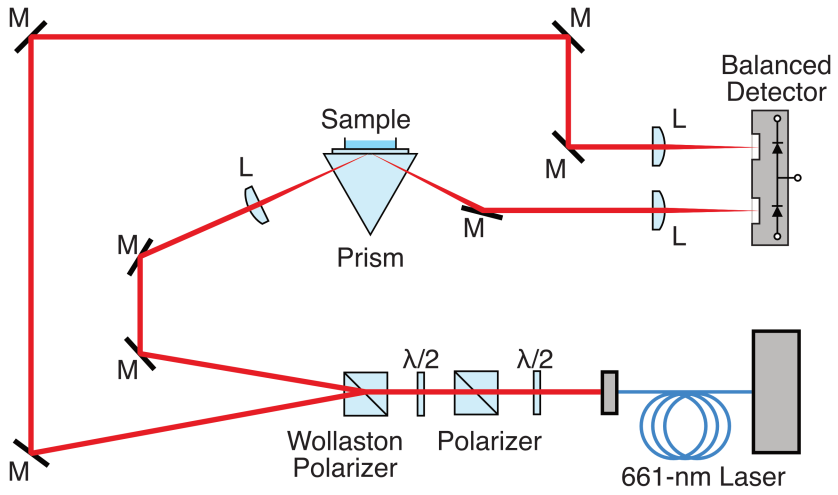

Figure 3.8: Schematic showing the setup of the original ECORE experiment. The following abbreviations are used: M=mirror, $\lambda/2$=half-wave plate, L=lens.

sample and emerges from the other open face of the prism, where it is directed towards the other photodiode of the balanced detector.

At the sample, voltage changes in the proximity of the electrochromic film lead to changes in the index of refraction of the film. An extracellular action potential, therefore, can be recorded using a detector to monitor the changing reflectance of the sample, as we saw in eq. (3.43). However, the fractional reflectance changes ($\Delta R/R$) are expected to be very small, on the order of one part per thousand or smaller. A balanced detector helps detect these small changes by outputting the difference of the detected signal and reference beam powers. This also helps in the reduction of common-mode noise, such as laser intensity noise, which is present in both beams. Therefore, the balanced detector improves the sensitivity of the setup to small extracellular potentials.

3.6.1.2 Setup optimization

In the development of the original ECORE experiment, many variables were considered to optimize the setup. The choice of operating the setup with reflection from (rather than transmission through) the electrochromic material was made to allow for recording with higher SNRs. This is because transmission of light through a sample containing multiple inhomogeneities (such as cells) leads to scattering, which can increase noise. Another factor in increasing noise is the transmission through an aqueous medium, which is very sensitive to environmental vibrations. Thus the setup was optimized for reflection from the sample, as described above [47]. All subsequent ECORE setups have maintained a reflection-based recording method for these reasons.

3.6.1.3 Sample optimization

Another consideration was the choice of electrochromic material. Given the existence of multiple biocompatible materials, discussed in an earlier section, this choice is important in optimizing the recorded signal. Prussian blue, iridium (IV) oxide, and PEDOT were all tested to find the best material from these candidates [47]. The optimal operating conditions of the Prussian blue and iridium oxide thin films were under high K^+ and high H^+ concentrations, respectively. Since the concentration of both ions is low under physiological conditions, these materials do not have the best response in the recording conditions for cellular experiments. In particular, it was found that Prussian blue had too slow of a temporal response to be able to detect action potentials [47]. On the other hand, PEDOT was found to have the best stability in physiological conditions and gave the strongest electrochromic response for the detection of bioelectric signals. Thus PEDOT was selected for subsequent experiments with cells.

3.6.1.4 Results of cell-free experiments

The setup was first tested using an artificial potential, applied though a potentiostat. Square wave potentials of various magnitudes (a few mV) were applied and the optical response of the PEDOT sample, in terms of $\Delta R/R$, was recorded. The recorded response was found to closely follow the shape of the applied square wave potential [18]. For a given recording, the signal strength can be determined by finding the magnitude of this square-wave response. The noise of the recording can be determined using the standard deviation of the recorded trace in a flat region of the trace. The SNR is then defined as

$$\text{SNR} \equiv \frac{\text{ECORE recording magnitude}}{\text{ECORE recording noise}}\,. \tag{3.53}$$

Once the SNR is determined for a recording, the detection limit of the setup can also be determined. This is defined to be the lowest potential that can be detected with a hypothetical SNR = 1. That is, the detection limit is defined as

$$\text{Detection Limit} \equiv \frac{1}{\text{SNR}}\,. \tag{3.54}$$

The typical recording magnitude and noise were determined to be $\Delta R/R \sim 3 \times 10^{-3}\,\text{mV}^{-1}$ and $\Delta R/R \sim 2 \times 10^{-5}$, respectively [18], thus

$$\text{SNR} = \frac{3 \times 10^{-3}\,\text{mV}^{-1}}{2 \times 10^{-5}} = 150\,\text{mV}^{-1} \qquad \text{(Original ECORE)} \tag{3.55}$$

and

$$\text{Detection Limit} = \frac{1}{150\,\text{mV}^{-1}} = 6.7\,\mu\text{V}\,. \qquad \text{(Original ECORE)} \tag{3.56}$$

A detection limit of 6.7 µV should be sufficient for the recording of extracellular action potentials from cardiomyocytes, which have magnitudes of ∼100 µV as we previously saw.

3.6.1.5 Results of cellular experiments

The ability of the original ECORE setup to detect bioelectric signals was then tested by using it to record action potentials from different types of cells. The original ECORE experiment was able to record spontaneous action potentials in human induced pluripotent stem cell (hiPSC)-derived cardiomyocytes, cultured rat hippocampal and dorsal root ganglion (DRG) neurons, and rat hippocampal brain slices [18] without any averaging. It was also noted that ECORE provides similar SNRs to multielectrode array recordings of the cardiomyocyte samples used in the experiments [18]. Unlike multielectrode arrays however, ECORE was able to maintain full spatial flexibility, giving the user the ability to move the beam and study any cells of interest. Furthermore, because the cells do not show any adverse reaction to the PEDOT, recordings from the same sample were taken over multiple sessions spanning many days.

An interesting consequence of ECORE is that, in addition to recording the electrochromic optical response from the PEDOT, it also registers the mechanical movement of cells in the recording [18]. This occurs because a physical movement of the cell causes a slight index change (specifically, n_3 in Fig. 3.5 changes) which leads to a small change in the absolute reflectance R. The reflectance change ΔR_{mech} due to the movement of a cell can be an order of magnitude greater than the ΔR of the electrochromic signal due to the action potential [18]. This effect is especially pronounced in cardiomyocytes, which contract in order to pump blood. However, as the mechanical signal is more prolonged compared to the extracellular action potential, it can be easily filtered out by processing the recording. The mechanical signal is also seen to occur at a later point in time compared to the action potential, providing clear separation of the two effects in a recording.

The original ECORE experiment successfully demonstrated that electrochromism could be used to record bioelectric signals from cells. However, the setup was nontrivial to align due to the interaction of the prism with the oblique incident angles required for total internal reflection. It was also noted that the sensitivity of ECORE could be further improved by optimizing the wavelengths of light used and by exploring more materials, and that the spatial resolution of ECORE could be further enhanced to provide action potential readouts from smaller areas of a cellular sample.

3.6.2 Dual-color ECORE

The original ECORE experiment made use of one light source — a laser of wavelength 661 nm. Like most electrochromic materials, the optical response of PEDOT varies with different wavelengths of light. It is possible to find a combination of two wavelengths such that the reflectance change of a PEDOT film (in response to some applied voltage) is in the opposite direction for the two wavelengths. That is, upon application of some voltage signal, the reflectance of the PEDOT increases for one wavelength and decreases for the other. This property can be leveraged to increase the sensitivity of ECORE.

The dual-color ECORE experiment [19] utilized the same optical setup from the original ECORE experiment. However, instead of using a single laser source, dual-color ECORE employed laser sources with two different wavelengths — 561 nm and 658 nm. These light sources were selected as PEDOT offers opposing responses to the two wavelengths. Light from the two sources is spatially overlapped by coupling into the same optical fiber. The combined light is directed to the sample as described in the previous section. Upon reflection from the PEDOT, the combined light is separated using dichroic mirrors and directed towards two separate balanced detectors (the combined reference beam is likewise split and directed to the respective detectors).

The signals from the two detectors are then linearly combined to give an overall signal with a stronger response to an applied voltage than would be possible with just one wavelength. Since the reflectance changes of the 561 nm and 658 nm beams are opposite to each other, the combined signal amplifies the ECORE recording of any applied voltages. Conveniently, the two wavelengths react in the same manner to any common-mode artifacts, i.e., the linear combination will cancel out most signals that are unrelated to the applied voltage. For example, a dust particle that momentarily drifts through the combined beam will lead to the same effect in both detector signals. Therefore, the combined signal also reduces any artifacts, in addition to the common-mode noise reduction that is already enabled by balanced detection. The overall effect is that the signal of interest is reinforced while noise is significantly reduced [19].

The dual-color ECORE experiment demonstrated that the enhanced signal afforded by the use of two wavelengths improves the recording SNR. With a SNR > 200 for a square wave of amplitude 1 mV, the dual-color setup reported the following detection limit [19]:

$$\text{Detection Limit} = \frac{1}{200\,\text{mV}^{-1}} = 5\,\mu\text{V}\,. \qquad \text{(Dual-color ECORE)} \tag{3.57}$$

Thus the use of two colors improves the performance of ECORE.

The experiment also made improvements in the optical setup to improve the spatial resolution. While still using a simple lens, the focusing of the two light beams was enhanced to achieve a spot size at the sample of $20 \times 12.5\,\mu\text{m}^2$ (semi-major and semi-minor axis at $1/e^2$ intensity, respectively). This made the dual-color ECORE beam just over $3\times$ smaller in area than the original ECORE experiment's beam.

The enhancement of the signal due to the dual-color response was demonstrated in (hiPSC)-derived cardiomyocytes, where the mechanical signals are common-mode and are therefore suppressed while the action potentials are enhanced. It was also noted that the dual-color nature of the experiment makes it complementary to fluorescence experiments, which often have a dual-color nature as well due to the difference in the excitation and emission wavelengths of fluorescent molecules. The experiment also reinforced the ability of ECORE to record signals for long durations, demonstrating stable recordings from the same sample over multiple recording sessions covering multiple weeks.

However, even though the spatial resolution was improved with modifications to the optical setup, the use of simple lenses places limits on the smallest spot size achievable.

Furthermore, because dual-color ECORE retains the prism-coupled geometry of the original experiment, it also remains nontrivial to align due to the oblique incidence angles.

3.6.3 ECORE with alternative materials

So far, we have discussed ECORE experiments utilizing thin films of PEDOT as the electrochromic material. However, given the wide range of electrochromic materials available, it is reasonable to assume that other materials may perform better in the context of ECORE.

Utilizing the same optical setup as the dual-color ECORE experiment, but now with only the laser of wavelength 561 nm, experiments were performed with different electrochromic materials [20]. Specifically, these experiments looked at dioxythiophene-based polymers, including PEDOT and PProDOT.

At the wavelength used, it was found that optical response of the PProDOT was significantly stronger than that of PEDOT. With a SNR $\approx$ 300 for a square wave of amplitude 1 mV, recording with PProDOT gave the following detection limit [20]:

$$\text{Detection Limit} = \frac{1}{300\,\text{mV}^{-1}} = 3.3\,\mu\text{V}\,. \qquad \text{(ECORE with PProDOT @ 561 nm)} \quad (3.58)$$

The improved detection limit was utilized to record action potentials from (hiPSC)-derived cardiomyocytes, as well as from rat hippocampal neurons [20]. These experiments demonstrated how the detection sensitivity of ECORE can be improved by exploring different materials. However, as these experiments again retained the basic optical setup of the original ECORE experiment, they were limited by the same restraints, such as limited spatial resolution and complex alignment procedures.

3.6.4 Summary of previous methods

Table 3.2 summarizes some important aspects of previous ECORE methods. Through changes to the optical setup and by building a better understanding of how electrochromic materials behave, we can see that ECORE has been significantly improved over time. In particular, simultaneous enhancements of the spatial resolution and the detection limit have been achieved, allowing for more sensitive recording from smaller detection regions of samples.

However, in addition to the limited spatial resolution of the methods above, there are other limitations of the original ECORE optical setup. Challenges to the alignment of the setup arise from the prism-coupled geometry, which prevents easy realignment of the signal beam if, for example, the angle of incidence must be changed. The construction and operation of ECORE therefore requires greater experience with optics to successfully operate the specialized setups. Another issue is imaging the samples — this has to be done using a microscope objective placed above the sample. Movement of the beam therefore can also necessitate moving the objective to bring the correct sample area into the field of view. This prevents quick, live imaging when movement of the beam across the sample is desired.

	Original [18]	Dual-color [19]	Alternative materials [20]
Material	PEDOT	PEDOT	PProDOT
Wavelength	661 nm	561 nm & 658 nm	561 nm
Resolution ($1/e^2$)	$28.4 \times 28.4\,\mu m^2$	$20 \times 12.5\,\mu m^2$	$20 \times 12.5\,\mu m^2$
Detection limit	6.7 µV	5 µV	3.3 µV
Biological cells	CMs & neurons	CMs	CMs & neurons

Table 3.2: Summary of the previous ECORE experiments presented in this section. The abbreviation "CMs" means cardiomyocytes.

These limitations present challenges to a wider implementation of ECORE for the recording of bioelectric signals.

3.7 ECORE with microscope objectives

One possible solution to resolving the issues discussed in the previous section is to use a microscope objective to replace the lens and prism in Fig. 3.8. Objectives that both direct the incident light to and collect reflected light from a sample are available and simplify the optical setup greatly. These objectives are commonly used in established microscopy techniques, making them familiar to many researchers. The same objectives are also able to achieve the smallest possible spot sizes allowed by optical theory. Finally, these objectives can be used simultaneously for imaging in addition to performing the total internal reflection needed for ECORE, simplifying the imaging procedure vastly.

In practice, however, high performance microscope objectives present numerous challenges. Because they are constructed using multiple lens elements and have very high magnifications, they are more susceptible to noise from unwanted reflections and vibrational noise. These challenges have so far prevented the use of objectives in ECORE. In the next chapter, we will consider microscope objectives in more detail and see how these challenges can be overcome to realize an objective-based ECORE setup.

Chapter 4

Experimental Setup

Note: Major portions of this chapter are based on a manuscript submitted to a peer-reviewed journal. A preprint is available [52].

4.1 Introduction to microscope ECORE

In this chapter, we will introduce microscope ECORE — a modified ECORE technique based on a high-NA objective. Microscope ECORE utilizes many of the concepts that we discussed in the previous chapter and has been developed from previous ECORE experiments. However, there are a few additional theoretical concepts that we must discuss to better understand microscope ECORE.

4.2 Theoretical considerations

We have explored the pivotal role that light plays in ECORE experiments. However, it is even more important to consider the various aspects that affect the manipulation of light when working with microscope objectives.

4.2.1 Diffraction limit

Collimated light that passes through a converging thin lens will converge to a focused spot at the focal point of the lens, a distance f away from the lens. For compound lenses, such as microscope objectives, this concept can be extended with the definition of the effective focal length, now defined from the principal planes of the system.

Besides the focal length f, lenses are also characterized by their numerical aperture (NA). The numerical aperture of a lens system is defined as

$$\mathrm{NA} \equiv n \sin\theta, \tag{4.1}$$

where n is the index of refraction of the medium in which the lens is operating, and θ is the angle made by the marginal ray with the optical axis of the system. The NA therefore characterizes the ability of a lens system to collect light — higher NA values signify that a lens is able to collect more light. The NA is also invariant as it passes through a system containing materials with multiple refractive indices. This can be seen by comparing Snell's law (eq. (3.8)) with eq. (4.1).

Regardless of the quality of a lens system, diffraction places limitations on how tightly the system can focus light [53]. That is, light cannot be focused down to an arbitrarily small point. This restriction is quantified by the diffraction limit. The radius r of the focal spot for a diffraction-limited system is given by

$$r = \frac{1.22\lambda_0}{2\mathrm{NA}}, \tag{4.2}$$

where λ_0 is the wavelength of light in vacuum. For a light source with $\lambda_0 = 510\,\mathrm{nm}$ utilizing the full NA of an objective with NA = 1.49, the diffraction-limited spot size will have a radius of $r = 209\,\mathrm{nm}$.

The above discussion applies to an aberration-free system. Aberrations distort the quality of the focused spot size and worsen the resolution that is obtained from eq. (4.2). Therefore, the presence of aberrations further limits how tightly light can be focused. Many high performance microscope objectives are corrected for multiple aberrations, and some are able to achieve the diffraction limit when properly operated.

4.2.2 High-NA objectives

Many microscope objectives are commercially available and offer features that enable a wide range of experiments. For example, objectives are often designed for use with one type of immersion medium. Many objectives have nothing in between the sample and the objective (i.e. they use air as the immersion medium), while others may use water or oil as the immersion medium. Objectives employing water as an immersion medium are commonly used for imaging of cells in cell culture media, where a close distance between the objective and sample (the working distance) may be required.

Another reason for using other immersion media is to increase the NA of a lens system. With air objectives ($n = 1$), the theoretical maximum is NA = 1. To achieve higher NA values, oil is often used as the medium. Commonly-used oil immersion objectives use oils with an index $n \sim 1.52$ so that the oil index matches that of glass, which is used in the lens elements of the objective. This enables imaging with higher numerical apertures, and therefore smaller spot sizes (equivalently, with a higher resolution).

In addition to enabling imaging with higher resolution, high-NA objectives are also necessary if the same objective must be used for total internal reflection (TIR) of the incident light. That is, if one wants to both direct incident light to a sample at supercritical angles and collect the reflected light, a high-NA objective is often necessary. This is indeed the case in total internal reflection fluorescence (TIRF) microscopy experiments, which utilize specialized high-NA objectives, often referred to as TIRF objectives.

TIRF experiments are typically carried out in cells (where $n_{\text{cell}} \sim 1.33$) cultured on top of glass coverslips ($n_{\text{glass}} \sim 1.52$). Therefore, to achieve total internal reflection at the glass-cell interface, it is necessary that $n \sin\theta \geq 1.33$ in every medium between the objective and the cell. Equivalently, we must have NA ≥ 1.33. We see that an air objective, for example, simply would not work in this scenario. Therefore, high-NA objectives with oil immersion media are typically used in TIRF experiments, with numerical apertures in the range 1.45 to 1.49. These objectives are also often corrected for major aberrations and are able to perform close to the diffraction limit across a range of wavelengths.

Based on our earlier discussion of a typical ECORE sample (see Fig. 3.5), we can see that an objective designed for TIRF can also be used in ECORE. For the critical angle in a typical ECORE sample ($\theta_c = 61.2°$, eq. (3.40)), the minimum NA that must be achieved is $\text{NA}_{\text{min}} = n_0 \sin\theta_c = 1.33$. Therefore, in principle, a TIRF objective is suitable for ECORE.

However, in practice, high-NA objectives can introduce significant noise when used in an ECORE setup. One source of noise stems from the fact that these objectives often have high magnifications (typically 60× or 100×). Due to these high magnifications, any undesired movement of the setup (for example due to environmental vibrations) may significantly displace the incident or reflected beams from their intended optical paths. This relative movement of the different components of the setup ultimately leads to an increase in the noise of the detected signal. High-NA objectives are often used in setups with strong vibration isolation to reduce this type of noise.

Furthermore, to achieve high levels of performance and minimize aberrations, these objectives are constructed with many lens elements [54]. Incident light (or reflected light from the sample) has many opportunities to reflect from the surfaces of these lens elements and interfere as it emerges from the rear of the objective. These unwanted reflections — known as parasitic reflections — can degrade image quality. In the context of ECORE, if such an objective is used, parasitic reflections would represent a major source of noise, given the low reflectance changes that must be detected to record action potentials.

4.2.3 Parasitic reflections and light sources

In order to better understand parasitic reflections — and how to address them — we must consider the role that the light source plays in the detection of these unwanted reflections.

In addition to the central wavelength of their light output λ_0, light sources that are used in lab settings are also often characterized by their linewidth. The linewidth is given either in terms of the wavelength ($\Delta\lambda$) or the frequency ($\Delta\nu$, where $\nu = c/\lambda$), and represents the spectral width of the emitted light. Given the wavelength linewidth $\Delta\lambda$, the frequency

linewidth can be determined using the relationship

$$\Delta\nu \approx c\frac{\Delta\lambda}{\lambda^2}\,. \tag{4.3}$$

The linewidth is related to the coherence time t_{coh} of the light output. For the common case of a Lorentzian spectral lineshape, the coherence time is

$$t_{\mathrm{coh}} = \frac{1}{\pi\Delta\nu}\,. \tag{4.4}$$

The coherence time characterizes the ability of light to interfere with itself after a time delay. Specifically, if a beam is split into two arms by a beamsplitter and one arm is delayed before the beams are recombined, the coherence time determines how large that delay can be while still allowing observable interference. For delays much shorter than t_{coh}, the two beams interfere strongly, whereas for delays much longer than t_{coh}, the interference visibility becomes negligible.

We can also define a coherence length L_{coh}, which similarly determines the path length difference between the two arms over which interference remains observable. The coherence length is given by

$$L_{\mathrm{coh}} = c\,t_{\mathrm{coh}}\,. \tag{4.5}$$

Many optical applications (including all previous iterations of ECORE) utilize laser light sources. Lasers couple the amplification of light in a gain medium with optical feedback in a cavity to produce output light with very high temporal coherence [55]. In the gain medium, incident photons stimulate the emission of additional photons with the same frequency, phase, and direction as the original photon, leading to coherent optical amplification. The optical cavity reinforces this process by repeatedly reflecting light through the gain medium, allowing only wavelengths that satisfy the cavity resonance condition to build up efficiently. The cavity of a laser consists of two mirrored surfaces on either end of the gain medium, shown in Fig. 4.1(a). One surface is highly reflective ($R_1 \approx 1$), while the mirror on the output side of the laser is partially transmitting ($R_2 < 1$) to allow a portion of the resonant light to emerge as the output beam.

With a stable cavity length, only discrete axial modes that satisfy the resonance condition can be sustained within the cavity. As a result, laser emission is confined to a very narrow spectral linewidth (often $\ll 1\,\mathrm{nm}$), corresponding to a very high degree of temporal coherence. Lasers thus have long coherence lengths, ranging from a few meters to many kilometers. The high temporal coherence of lasers is usually a desirable property, allowing the interference of two beams with fairly large path differences. For the same reason, however, if light from a laser is used in an optical setup containing a high-NA microscope objective, parasitic reflections can remain coherent with the signal beam and interfere at the detector, producing unwanted intensity fluctuations and increased noise in the measured signal.

If the optical feedback is removed from a laser setup and a medium with sufficiently high gain is used, it is possible to achieve output light with much lower temporal coherence than

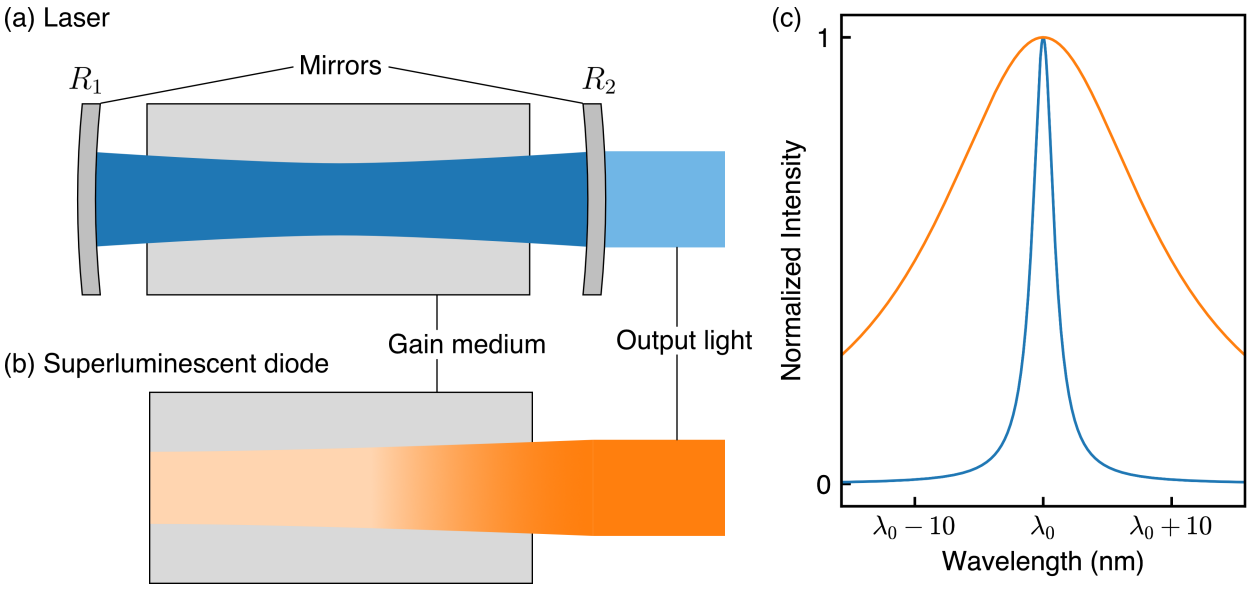

Figure 4.1: Schematics showing the geometrical differences between (a) a laser and (b) a superluminescent diode (SLD). (c) Spectral linewidths of a laser diode (with $\Delta\lambda = 1\,\text{nm}$) and SLD (with $\Delta\lambda = 10\,\text{nm}$) with center wavelengths of λ_0.

in a laser. This concept is known as amplified spontaneous emission [55] and is used in the construction of superluminescent diodes (SLDs), shown in Fig. 4.1(b). Light from SLDs still possesses the other desirable properties of lasers, such as high brightness and high spatial coherence. However, SLDs typically have much wider linewidths (typically on the order of 10 nm to 100 nm) than lasers due to the lack of optical feedback and therefore the coherence lengths are correspondingly shorter. The difference in spectral width between a laser diode (shown here with $\Delta\lambda = 1\,\text{nm}$ for illustration) and an SLD (with $\Delta\lambda = 10\,\text{nm}$) is depicted in Fig. 4.1(c). While the laser spectrum shown is narrower than that of the SLD, actual single-mode laser diodes can achieve linewidths that are orders of magnitude smaller than the value illustrated, often far below 0.001 nm.

Typical SLDs have coherence lengths of only a few micrometers, owing to their large linewidths. These short-coherence-length light sources are useful in preventing the interference of two light signals whose path lengths differ by small distances. If the path length difference of the two beams is larger than the coherence length of the SLD, then their interference will be strongly suppressed. SLDs therefore help in reducing noise from parasitic reflections.

4.3 Sample preparation

While many setup considerations can be carried over from the original ECORE setup to one based on a high-NA objective, one key difference is the sample substrates that may be used. In the original ECORE setup, the signal beam is reflected by the sample through a prism optically coupled to a glass slide using index-matching oil. The thickness of the slide is not very important, as many different thicknesses can be accommodated. For example, if the slide is made thicker and everything else is kept the same, then the reflection will occur farther to the right in Fig. 3.8. Due to the large size of the prism, the reflected beam will still emerge from the other face of the prism, but slightly higher up. Thus the light can still be collected by realigning the setup, allowing for a range of slide thicknesses to work in the original ECORE setup.

In contrast, high-NA objectives are designed to collect as much supercritical light as possible. To enable maximum collection of light (equivalently, to maximize the NA), the sample must be positioned very close to the front element of the objective. That is, the working distance — the separation between the objective and the sample plane — must be very small. This constraint necessitates the use of very thin glass coverslips, usually within a narrow thickness range of 130 µm to 190 µm. If thicker glass slides are used, part of the reflected light falls outside the collection cone of the objective and is therefore not detected. For this reason, the thicker glass substrates used in previous iterations of ECORE cannot be used with high-NA objectives.

Therefore, to ensure our samples were compatible with a high-NA objective, we initially utilized commercially available ITO-coated coverslips from various manufacturers. However, these standard components yielded poor results for the electrodeposition of the electrochromic material (a process discussed in the following paragraph) and therefore failed to perform adequately within our experimental framework. Consequently, we transitioned to custom coverslips (with dimensions $22 \times 22 \times 0.15\,\mathrm{mm}^3$) produced by the same manufacturer used in previous iterations of ECORE. These coverslips are custom-coated with a thin layer of ITO (CB-90IN, Delta Technologies) that matches the ITO preparation used in previous ECORE experiments, ensuring consistency.

As with all ECORE experiments, the glass-ITO substrates must be coated with a thin layer of an electrochromic material. We chose to work primarily with PEDOT as it is readily available and our labs have extensive prior experience with it [18–20, 47]. Thus, all coverslips are first coated with a thin film of PEDOT to create a PEDOT sample. Once coated, these samples can be used directly in cell-free experiments or further processed to attach cultured cells for cellular experiments. To each substrate, we first attached a custom 3D printed poly(lactic acid) sample well. These wells have a circular bottom opening of diameter 6 mm and allow aqueous solutions to be placed above the samples. Once the wells are securely attached to the coverslips, we deposit PEDOT onto the ITO-coated coverslips using a previously developed electrodeposition protocol [19]. While other coating processes can be used, and will be discussed in the next chapter, this electrodeposition protocol is our main method for the preparation of PEDOT. This process creates a thin film of PEDOT in the

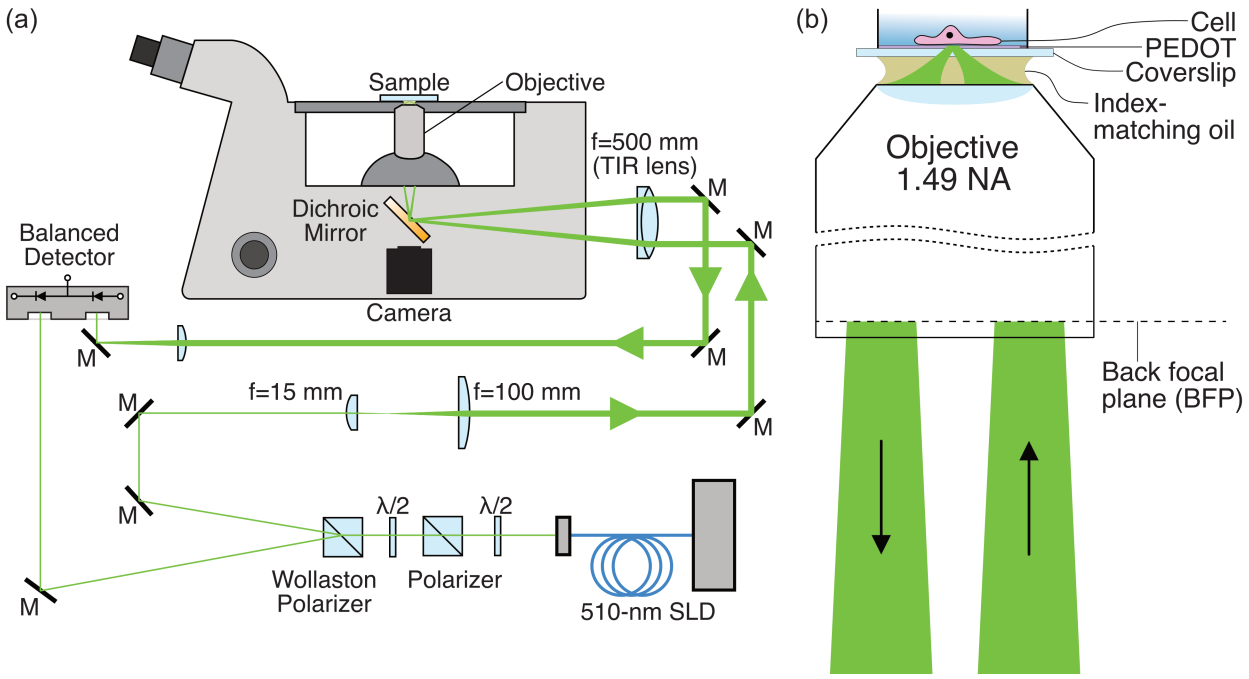

Figure 4.2: (a) Schematic showing the optical setup of microscope ECORE. The following abbreviations are used: M=mirror, $\lambda/2$=half-wave plate. Except for the SLD, all other components are placed on an optical breadboard. (b) Detail showing how the light is focused through the objective, is reflected by the sample, and then collected by the same objective.

circular opening of the well with an area of $\pi(3\,\mathrm{mm})^2 = 28.3\,\mathrm{mm}^2$. Once the electrodeposition process is complete, the PEDOT sample is ready for use in a microscope ECORE experiment.

4.4 Optical setup

A schematic representing the optical setup of microscope ECORE is shown in Fig. 4.2(a). The setup utilizes a geometry that is commonly used in TIRF microscopy. All optical elements, except for the light source, are placed on an optical breadboard measuring 36×24 inches. We will first discuss some notable components in this setup before describing it in more detail.

4.4.1 Key components

4.4.1.1 Light source

A superluminescent diode (SLD) with a wavelength of 510 nm is used in the experiment (EXS210115-00, Exalos). The SLD used has a typical linewidth of $\Delta\lambda = 10\,\mathrm{nm}$. Using

eqs. (4.3) to (4.5), the coherence length of our SLD is determined to be $L_{\text{coh}} \approx 8\,\mu\text{m}$. This is much shorter than the typical coherence lengths of laser light sources, which can range from meters to kilometers. Thus, if parasitic reflections are generated by reflection from any of the optical elements in the setup, their interference with the signal beam will be suppressed. This will occur if the path length difference between the signal beam and a parasitic reflection is a few tens of micrometers or greater. Thus an SLD helps prevent against noise caused by unwanted reflections in the setup.

The choice of wavelength depends on the anticipated sensitivity of the PEDOT to a given wavelength as well as the availability of SLDs near that wavelength. From previous measurements on PEDOT, we know that PEDOT shows good sensitivity in the region of $\sim$500 nm [19, 20]. We therefore sought out SLDs in this wavelength region and found a suitably powerful device at 510 nm.

4.4.1.2 Microscope and objective

We use a popular, commercially available microscope base (Eclipse Ti-U, Nikon). A commercially available microscope base is used to demonstrate that microscope ECORE can be implemented in a typical lab setting, where such microscopes are commonly utilized in a variety of microscopy tasks.

The microscope base is paired with a high-NA TIRF objective (MRD01991, Nikon). This oil immersion objective has NA = 1.49 and a magnification of 100×, and is designed for TIRF applications. This objective is chosen primarily because it is able to achieve total internal reflection due to its high NA.

4.4.1.3 Detector

In our experiment, we use a balanced photodetector with a feedback resistor of resistance $R_{\text{f}} = 100\,\text{k}\Omega$ and two closely matched photodiodes (FDS100, Thorlabs) with responsivities of $\mathcal{R} = 0.177\,\text{A}\,\text{W}^{-1}$ for a wavelength of 510 nm. Along with this information, eq. (3.52) can be used to determine the output voltage of the detector for the power levels falling on each photodiode of the detector.

4.4.2 Description of the setup

Having discussed the major elements of the optical setup as well as some other important considerations, we are now ready to describe the setup in more detail.

Light starts out at the SLD, where it is immediately coupled into a fiber, as shown in Fig. 4.2(a). The fiber is used for spatial filtering, and the output of the fiber is directed to a half-wave plate and a polarizer, which produce a linear polarization state. This light is then directed to a second half-wave plate and a Wollaston polarizer, which splits the two orthogonal polarization components of light along two directions separated by 20° to form

the signal and reference beams. We can use the second half-wave plate to control the relative intensity of these two beams.

While the reference beam is sent directly to one photodiode of the balanced photodetector, the signal beam is first expanded by a pair of plano-convex lenses to a $1/e^2$ intensity radius of $\sim$2 mm. To reduce vibrational noise, all of the optical elements discussed so far are mounted at very low heights. However, the epi-illumination port of the microscope base is higher than these elements. Therefore, the signal beam is raised using two mirrors that form a periscope, and is then directed to the epi-illumination port of the microscope through an achromatic doublet lens with a focal length of $f = 500$ mm.

This $f = 500$ mm lens (hereafter referred to as the TIR lens) is a common feature in TIRF microscopy and is used to focus the signal beam onto the back focal plane (BFP) of the objective [56, 57], shown in Fig. 4.2(b). This lens is mounted on two translation stages that allow movement along and perpendicular to the optical axis. Movement along the axis is used to fine-tune the setup so that the TIR lens is accurately focusing light at the BFP of the objective. Movement of the lens perpendicular to the optical axis is used to change the angle of incidence (AOI) at the sample. This works because the BFP of the objective and the sample plane are Fourier planes — changing the position of the beam at the BFP results in angular variation at the sample plane. Thus we only need to laterally translate the beam at the BFP to easily change the AOI at the sample.

After the TIR lens, the signal beam passes through the objective, which focuses the light onto a sample. This is depicted in more detail in Fig. 4.2(b). The objective is mounted onto the objective turret of the microscope base, which can be moved vertically using a fine-adjustment knob on the base. Vertical movement of the objective (relative to the sample) allows for the correct focusing of light at the sample.

The sample is mounted onto a custom-designed aluminum mount, which is secured to a dual-axis translation stage on the microscope base above the objective. The two axes of movement of this translation stage allow the sample to be moved perpendicular to the optical axis, allowing for imaging of different points on the sample. At the sample, the light is reflected from the multiple layers of materials at the top of the coverslip and is collected by the same objective. The reflected light re-emerges from the epi-illumination port and is collected by another periscope, which now brings the light down to the level of the detector. Finally, the light is now directed to the other photodiode of the balanced detector, whose output is recorded using the recording scheme discussed later in this chapter.

4.4.2.1 Advantages

The microscope ECORE optical setup offers several advantages compared to the original, prism-coupled ECORE setup. In the original setup, focusing the light at the sample requires moving the lens before the prism along the axis of light. However, since the light and the prism are at oblique angles to each other, refraction makes it more difficult to focus the light to the exact point desired on the sample. Furthermore, movement of the incident beam significantly changes how the reflected light emerges from the prism, requiring frequent

realignment of the collection optics. Thus more time is needed to achieve good focusing at the sample. In contrast, focusing the light at the sample in microscope ECORE is simply achieved by translating the objective and the TIR lens along the optical axis, which is much easier and quicker. The TIR lens also makes it simple to change the AOI, as described in the preceding paragraphs. The ability to vary the AOI is frequently desired to optimize the setup as certain angles of incidence offer may provide better recording sensitivity [18–20, 47]. Varying the AOI may also be required if there is a change in the index of refraction of the cellular samples, which may affect the critical angle of the setup through eq. (3.40).

Another advantage is the ease and speed of sample imaging. In the original ECORE setup, the sample must be imaged by a separate objective placed above the sample. Thus movement of the incident laser beam requires a corresponding movement of the objective. On the other hand, in microscope ECORE, the same objective that is used to direct the signal light to and from the sample can also be used to image the sample. Imaging is easily achieved by placing a camera under the dichroic mirror in Fig. 4.2(a). The camera naturally images the field of view (FOV) containing the focused signal beam, and can therefore be used to simultaneously observe the specimen and perform an ECORE experiment.

But perhaps the most significant advantage is that the optical layout of microscope ECORE should be familiar to many researchers who perform microscopy. The use of TIR lens and the expansion of the beam via a pair of lenses are common alignment procedures employed in TIRF microscopy experiments, and many protocols exist to guide researchers on the proper construction of such experiments [56–59]. In addition to the knowledge of this geometry, many labs already possess microscope bases and objectives, which reduces the amount of new equipment a lab would have to acquire to construct an ECORE setup. Combined with the simpler alignment and simultaneous imaging described above, microscope ECORE should therefore be a much more attractive implementation of ECORE for researchers trying to study bioelectric signals.

4.5 Spatial resolution and spot size

4.5.1 Setup capabilities

In principle, it is possible for some objectives (including the objective we use) to focus light down to a spot size that is diffraction-limited. The spot size of the diffraction-limited spot, discussed earlier, is reproduced below:

$$r = \frac{1.22\lambda_0}{2\mathrm{NA}}\,. \qquad \text{(eq. (4.2))}$$

For our SLD with $\lambda_0 = 510\,\mathrm{nm}$, the diffraction-limited spot size will have a radius of $r = 209\,\mathrm{nm}$ (see scheme 1 in Fig. 4.3). To achieve this spot size, the entire back focal plane (BFP) of the objective must be fully illuminated. However, full illumination of the BFP also produces light at the sample which is incident at sub-critical angles. Since our setup

only detects light that has undergone total internal reflection at the reflecting interface, we impose the condition that all light must be reflected. That is, we require light to illuminate only that section of the BFP which allows all of the light to undergo TIR.

To find the diffraction-limited spot size of a beam where all rays are incident at supercritical angles, we must consider the usable NA range of the objective when this condition is imposed. This range can be determined by considering the materials involved (and their refractive indices) at the reflective interface. These were discussed in the previous chapter and the relevant values are summarized in table 3.1. With this information, the minimum NA that must be exceeded to ensure all rays undergo TIR is $\mathrm{NA}_{\mathrm{min}} = 1.33$. The maximum NA, of course, is set by the objective itself, which in our experiments is $\mathrm{NA}_{\mathrm{max}} = 1.49$.

In our setup, the TIR lens placed just outside the epi-illumination port of the microscope base focuses the light to a spot at the BFP of the objective. With this type of illumination, and imposing the condition that the entire beam must undergo TIR, the smallest spot size at the sample is therefore achieved when the focused spot at the BFP spans the entire allowed NA range (scheme 2 in Fig. 4.3). We can use the Abbe sine condition to determine that this spot at the BFP has $\mathrm{NA} = 0.08$. With this NA, the smallest spot size that can be achieved is $r = 3.89\,\mu\mathrm{m}$, considerably larger than if the full BFP is illuminated.

It is possible to illuminate the BFP in such a way that the spot size is smaller than $r = 3.89\,\mu\mathrm{m}$ while the entire beam undergoes TIR. This is achieved through annular illumination of the BFP within the confines of the minimum and maximum NA values for supercritical illumination (scheme 3 in Fig. 4.3). The radial intensity profile for this illumination scheme is given by the following relationship [56]:

$$I \propto \frac{1}{r'^2}\left[J_1\left(\frac{2\pi \mathrm{NA}_{\mathrm{max}} r'}{\lambda_0}\right) - \beta J_1\left(\frac{2\pi \mathrm{NA}_{\mathrm{min}} r'}{\lambda_0}\right)\right]^2, \tag{4.6}$$

where r' is the radial coordinate at the sample plane, J_1 is the Bessel function of the first kind of order 1, and $\beta \equiv \mathrm{NA}_{\mathrm{min}}/\mathrm{NA}_{\mathrm{max}}$. The first minimum of this profile occurs at $r' = 138\,\mathrm{nm}$, which is much smaller than if only a supercritical spot of the BFP is illuminated as is illustrated by scheme 2. It is also smaller than if the entire aperture is illuminated (where $r' = 209\,\mathrm{nm}$ as discussed earlier). However, with annular illumination, more intensity is spread into the diffraction pattern's higher orders, reducing the intensity at the central spot. This effect can be seen in the inset of Fig. 4.3, where we see more of the intensity lies outside the central peak for scheme 3.

4.5.2 Spot size used in the experiment

Fig. 4.4 shows the spot size of the beam in our experiment, compared to other ECORE beams and a typical sample of cardiomyocytes. We are able to focus the light down to a spot size of $12.9 \times 9.4\,\mu\mathrm{m}^2$ (semi-major and semi-minor axis at $1/e^2$ intensity, respectively). In principle, it is possible to reduce the spot size further, down to $r \sim 3.89\,\mu\mathrm{m}$ with our illumination scheme. However, reducing the spot size below our current size has detrimental

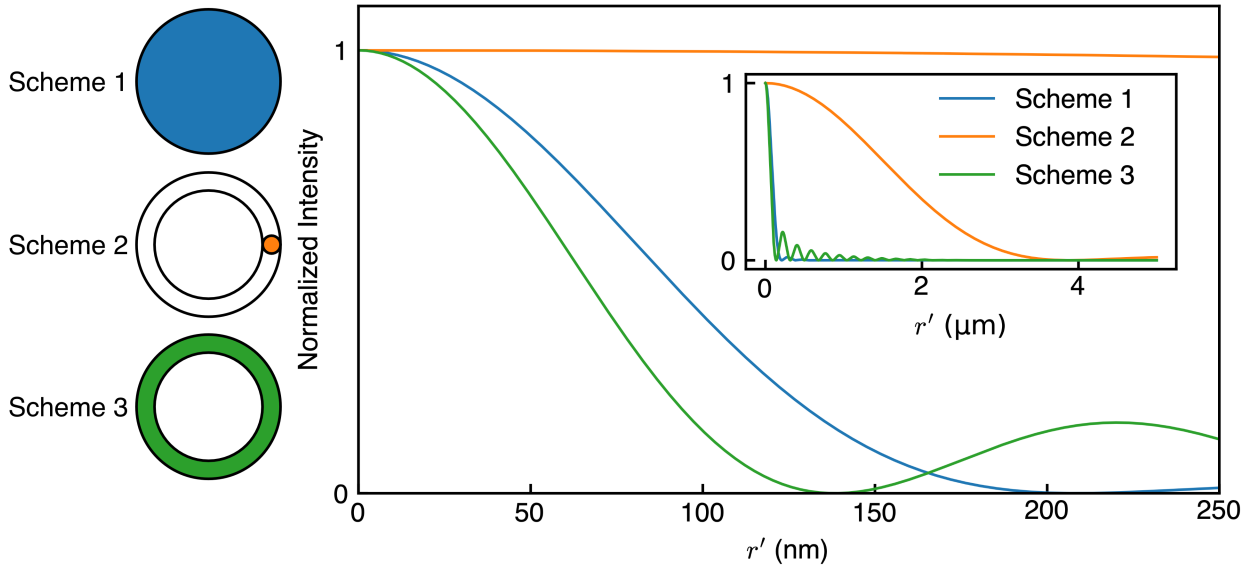

Figure 4.3: The three BFP illumination schemes discussed in the main text are depicted on the left hand side. Scheme 1 is full illumination of the entire BFP of the objective. Scheme 2 is the maximum illumination of the supercritical range of the BFP of the objective that can be achieved when light is focused to a spot at the BFP. Scheme 3 represents full illumination of the supercritical range of the BFP. The plot on the right shows the radial profile of the intensity of the focused spot produced at the sample due to each of the BFP illumination schemes. The inset shows a larger range of r'. Note that the intensity for each illumination scheme has been normalized to the intensity at $r' = 0$ to facilitate comparison between the different schemes.

effects on biological samples, reducing the recording duration as we will discuss in detail in a later chapter. Nevertheless, compared to other ECORE beams, the microscope ECORE beam is smaller and therefore permits recording from smaller regions of samples.

4.6 Data recording and analysis

The output of the balanced detector must be collected, digitized, and stored prior to analysis. High-frequency noise in the detected signal is first removed by using a physical low-pass filter with a cutoff frequency of ∼200 Hz. This filter also prevents aliasing in the digitized signal. The filtered signal is then recorded using a digitizer (Digidata 1550B1, Molecular Devices). The digitizer is capable of recording with very high sampling rates; however, we digitize at a sampling rate of 10 kHz as this is fast enough to capture the dynamics of action potentials. As previously discussed, action potentials can have durations of ∼1 ms, which correspond to frequencies well within the recording bandwidth of a signal digitized at 10 kHz.

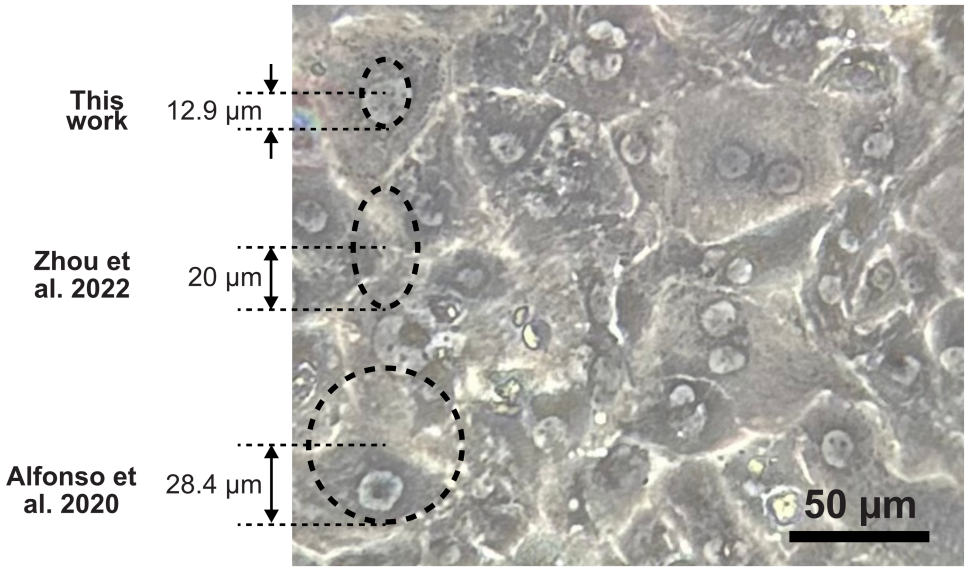

Figure 4.4: A typical sample of cardiomyocytes in a microscope image (from a separate objective). The dashed ellipses show the $1/e^2$ intensity radius spot sizes of various ECORE beams. From bottom to top, these are: the original ECORE beam [18], the dual-color ECORE beam [19], and the microscope ECORE beam.

The digitized signal is recorded and saved using a computer. We use the programming language Python for analysis. Common analysis operations include:

- Visualization and plotting of data
- Conversion of recorded voltage levels into standardized units for comparison between different datasets
- Digital filtering to further reduce noise and improve the SNR. For example, high frequency noise can be removed from the signal by applying a suitable low-pass filter that does not interfere with the desired signal we are recording
- Implementing algorithms to determine important metrics for a recording, such as the SNR

4.6.1 Recorded signal and reflectance changes

The detector output is recorded as a voltage level. To make comparisons across different samples, experimental conditions, and other variables, it is important to develop a standardized metric to compare across different experiments. By detecting the light output from the setup, we are essentially monitoring how the reflectance R of the sample changes. It would

be reasonable to work with ΔR, the instantaneous change in the reflectance as a function of time. However, because R itself is expected to vary across different samples, a better metric is $\Delta R/R$, the normalized change in the reflectance of the PEDOT. This accounts not only for differences in R between multiple samples, but also for changes in R across different areas of the same sample, and therefore provides a more standardized metric than ΔR.

Let's now consider how $\Delta R/R$ can be obtained from the detector output (in Volts). The reflectance of a sample at any point in time is defined by

$$R \equiv \frac{P_{\text{out}}}{P_{\text{in}}}\,, \tag{4.7}$$

where P_{in} is the power of light directed at the sample and P_{out} is the light power reflected by the sample (see Fig. 1.1). The change in reflectance ΔR between two points in time is therefore

$$\Delta R \equiv R_2 - R_1 = \frac{P_{\text{out2}}}{P_{\text{in}}} - \frac{P_{\text{out1}}}{P_{\text{in}}} = \frac{P_{\text{out2}} - P_{\text{out1}}}{P_{\text{in}}}\,, \tag{4.8}$$

where R_1 is the reflectance at some point in time and R_2 is the reflectance at some later point in time. We take the input power P_{in} to be constant in time, and only expect the reflected powers to change. Then, the normalized change in the reflectance $\Delta R/R$ is

$$\frac{\Delta R}{R} \equiv \frac{R_2 - R_1}{R} = \left(\frac{P_{\text{out2}} - P_{\text{out1}}}{P_{\text{in}}}\right)\left(\frac{P_{\text{in}}}{P_{\text{out2}}}\right) = \frac{P_{\text{out2}} - P_{\text{out1}}}{P_{\text{out2}}}\,, \tag{4.9}$$

where we have explicitly determined $\Delta R/R$ at the later point in time. In practice, however, the changes in R are so small that $P_{\text{out1}} \approx P_{\text{out2}}$, and the specific output power value used in the denominator has a negligible affect on $\Delta R/R$.

To determine $\Delta R/R$ from the detector output, we must consider how the detector responds to light that falls on it. The photodetector voltage output V_{det} is proportional to the difference in powers falling on the reference and signal photodiodes of the photodetector as derived previously in eq. (3.52). This relationship was found to be

$$V_{\text{det}} = \mathcal{R} R_{\text{f}} (P_{\text{sig}} - P_{\text{ref}})\,, \tag{4.10}$$

where we have now explicitly named the signal and reference photodiodes of the balanced detector. While the reference power is straightforward to define and measure, note that, in general, $P_{\text{sig}} \neq P_{\text{out}}$. This is because P_{out} represents the light reflected from the sample *just after* reflection while P_{sig} is the light falling on the signal photodiode of the photodetector. Upon reflection from the sample, the light must pass back through the objective where some power will be lost to absorption and/or reflection of the light by the elements in the objective. Therefore, by the time the reflected signal beam reaches the detector, the power will be $P_{\text{sig}} < P_{\text{out}}$. We must take those losses into account when drawing a relationship between eqs. (4.9) and (4.10). We can characterize these losses by writing the relationship as

$$P_{\text{sig}} = C_{\text{loss}} P_{\text{out}}\,, \tag{4.11}$$

where $C_{\text{loss}} \leq 1$ is a constant for any given operating condition of the experiment. For our objective, the transmittance is 82.9 % at our operating wavelength (510 nm). Ignoring losses from mirror reflections, which are negligibly small, we therefore have $C_{\text{loss}} = 0.829$.

We are now in a position to connect the detector voltage V_{det} to $\Delta R/R$. Starting with eq. (4.9), we have

$$\frac{\Delta R}{R} = \frac{P_{\text{out2}} - P_{\text{out1}}}{P_{\text{out2}}} = \frac{P_{\text{sig2}} - P_{\text{sig1}}}{P_{\text{sig2}}}\,, \tag{4.12}$$

where the last equality results from the fact that C_{loss} is found in both the numerator and the denominator. Now consider the detector voltage at time points 1 and 2. We can then write

$$\Delta V_{\text{det}} \equiv V_{\text{det2}} - V_{\text{det1}} = \mathcal{R}R_{\text{f}}\left[(P_{\text{sig2}} - P_{\text{ref2}}) - (P_{\text{sig1}} - P_{\text{ref1}})\right] = \mathcal{R}R_{\text{f}}(P_{\text{sig2}} - P_{\text{sig1}})\,, \tag{4.13}$$

where to reach the last equality we have used the assumption that the light power on the reference photodiode of the detector is constant once the detector has been balanced. Finally, comparing eqs. (4.12) and (4.13), we have:

$$\frac{\Delta R}{R} = \frac{1}{\mathcal{R}R_{\text{f}}}\frac{\Delta V_{\text{det}}}{P_{\text{sig2}}}\,. \tag{4.14}$$

That is, the detector voltage output is proportional to $\Delta R/R$. In addition to recording the detector voltage, to determine $\Delta R/R$ we must therefore also know $\mathcal{R}$, R_{f}, and P_{sig2}. As previously stated, in our setup, we have $\mathcal{R} = 0.177\,\text{A}\,\text{W}^{-1}$ and $R_{\text{f}} = 100\,\text{k}\Omega$. P_{sig2} is determined by measuring the power at the signal photodiode of the detector using a power meter. With this information, we can convert recorded signals into $\Delta R/R$. Most of the data in the following chapters will be presented in terms of $\Delta R/R$.

4.7 Noise mitigation

In addition to noise reduction from the short coherence length of the SLD, we also take other steps to ensure the reduction of technical noise in our experiments.

One of the biggest sources of noise in any ECORE experiment is vibrational noise from the environment. Even small residual vibrations from the environment are able to cause a beam to drift significantly from its intended path, particularly in the case where high-NA, high magnification objectives are involved. These unintended deviations from the optical path cause the recorded light level to fluctuate at the detector, leading to a lower SNR. To reduce the effects of this noise in our experiments, we place the setup breadboard on a floating, damped optical table. The floating table suppresses environmental vibrations so that their effect on the setup is minimized. Despite this, residual vibrations can still make their way through to the experiment. To reduce these residual vibrations, we ensure that all optical elements are rigidly clamped to the optical breadboard, which is then rigidly

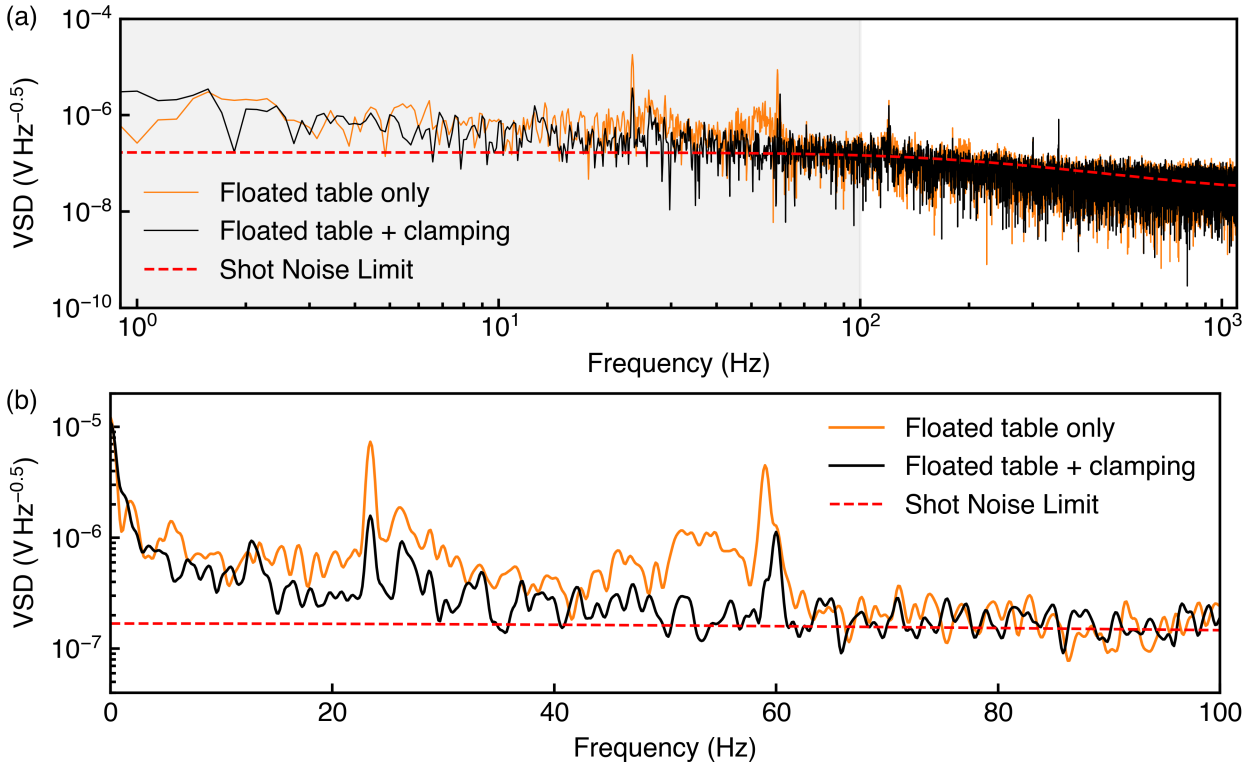

Figure 4.5: (a) VSDs of two recordings from microscope ECORE. In one recording, the optical table is floating but the microscope base is not clamped to the breadboard (orange). In the other recording, we now clamp the microscope base to the breadboard (black). The shot noise limit is also shown. (b) Zoomed-in section of the shaded section of the plot in (a). The spectra have been smoothed using a Gaussian filter to facilitate comparison. Note the linear frequency axis in this plot.

attached to the optical table. This minimizes any relative movement between the elements, and therefore further reduces noise in the setup.

This reduction in noise can be clearly seen when comparing the frequency spectra of recordings obtained with different amounts of clamping of optical components to the breadboard. In one experiment, we studied the effect of rigidly clamping the microscope base to the breadboard (which itself is secured to the floating optical table). We mounted a cell-free sample on the setup (i.e., a PEDOT sample with an aqueous solution), directed the reflected beam to the detector, and recorded the output voltage of the detector (note that no voltage is applied to the sample in this experiment). We then plotted the voltage spectral densities (VSDs) of the two experimental configurations — with and without clamping — along with the expected shot noise level (we discuss shot noise in detail in the next chapter). The results are shown in Fig. 4.5.

From Fig. 4.5(a), we can see that the clamped configuration of the setup has lower noise than when the microscope base is not clamped. Figure 4.5(b) shows the VSDs in the lower frequencies ($< 100\,\text{Hz}$) — where vibrational noise is typically higher. In this plot, the reduction in noise that accompanies clamping is very clear. In fact, we see that there is an order of magnitude reduction in the amplitude of the VSD at certain frequencies. Thus, it is essential to rigidly mount optical components in the setup to mitigate vibrational noise.

To further prevent other environmental factors from adversely affecting our recorded signal, we also place the entire experimental setup within an enclosure made of opaque panels. This enclosure is intended to reduce the amount of room light reaching the detector, and therefore minimizes the noise from environmental light such as overhead room lights. The enclosure also helps keep the optical elements inside clean, and prevents any air currents or particulate matter (such as dust) from disturbing the experiment while it is in operation.

Another common source of technical noise is electrical interference noise, for example $60\,\text{Hz}$ pickup noise. This type of noise frequently occurs due to improper wiring of different electrical devices. For example, if two interconnected electrical devices in a setup are plugged into two separate wall outlets, this can lead to the creation of a ground loop (i.e., when the grounds of the two devices are at different potentials). This ground loop is then sensitive to stray oscillations in magnetic fields, which are always present in the environment. The oscillation of such fields can create an unwanted signal which is picked up by the ground loop through induction, causing noise in the detected signal. A simple way to address this issue is to plug both devices into a common outlet such as a power strip, forcing all devices to share the same physical ground. We therefore plug in all signal application and detection electronics into the same power strip to mitigate this source of noise.

With all of these noise mitigation steps in place, we have now presented the optimized version of the optical setup. In the next chapter, we describe sample optimization and characterization experiments that were carried out throughout the development of microscope ECORE to help maximize its recording capabilities.

Chapter 5

Cell-Free Experiments with Microscope ECORE

Note: Major portions of this chapter are based on a manuscript submitted to a peer-reviewed journal. A preprint is available [52].

As we saw in the earlier discussion of previous ECORE setups, it is possible to record artificial (as opposed to biological) signals using cell-free experiments. These experiments aid in the development of the setup and allow us to characterize its performance before moving on to recording with cells. By their nature, cell-free experiments are also more repeatable given that the fluctuations in voltage are imposed on the setup by the experimenter in a controlled manner.

This chapter looks at cell-free experiments performed with microscope ECORE. We start by describing how these experiments are performed, before explaining the various optimizations that were made to improve the recording capabilities of microscope ECORE. Finally, we characterize the performance of the optimized microscope ECORE setup and demonstrate that it possesses the sensitivity to be able to detect bioelectric signals.

5.1 Setup considerations

We attempt to perform cell-free experiments with conditions that approximate cellular experiments to the extent possible. Most importantly, since cells exist in environments primarily consisting of water, we must apply and record the response of artificial potentials through some solution placed in contact with the PEDOT. Furthermore, this solution must be conductive as the electrodes used in cell-free experiments cannot be placed in contact with the PEDOT. This is in contrast to cellular experiments, where the cells are placed in contact with (or are very near to) the PEDOT film. Thus, to increase the conductivity of this solu-

tion compared to pure water, we use a solution of 1× phosphate buffered saline (PBS). This solution of PBS is held by the sample well that is attached to the top of all samples.

A potentiostat is used to apply a voltage to the PEDOT through the PBS solution. In our experiments, we use an Ag/AgCl electrode as the reference electrode (RE), which is a common practice in experiments using potentiostats. This is because Ag/AgCl electrodes provide a stable, well-defined reference potential. The PEDOT/ITO interface serves as the working electrode (WE) while the counter electrode (CE) is a platinum wire submerged in the PBS solution. The voltage signal is passed into the potentiostat though a function generator, which is typically used to apply a square wave potential to the PEDOT film.

5.2 Typical cell-free recordings

We program the function generator to apply a square wave potential $V_{\mathrm{sq}}(t)$ to the sample through the potentiostat. Most commonly, we apply square waves with a peak-to-peak voltage of $V_{\mathrm{pp}} = 1\,\mathrm{mV}$. All square waves have frequency 1 Hz.

We also typically apply a bias voltage V_{bias} in addition to the square wave. This is important as cells exist in conditions with varying open circuit potentials, and bias voltages can be used to approximate these conditions. The typical open circuit potential for cardiomyocytes is $\sim$−50 mV with respect to a standard Ag/AgCl electrode [18, 19]. As this potential is very small, we typically operate with an applied bias potential of $V_{\mathrm{bias}} = 0\,\mathrm{mV}$. Altogether, we can write the applied signal (the voltage between the WE and RE of the potentiostat in Fig. 3.6) as

$$V_{\mathrm{app}}(t) = V_{\mathrm{bias}} + V_{\mathrm{sq}}(t)\,, \tag{5.1}$$

where V_{bias} is constant in time.

A typical microscope ECORE recording of an applied square wave potential is shown in Fig. 5.1. We can see that the recording closely mirrors the shape of the applied square wave. The recording also shows a temporal response, which is seen in the rising and falling of $\Delta R/R$ over some finite time period. This response can be characterized by the 10 % to 90 % rise time (τ_{r}).

A finite rise time is expected due to the diffusion of ions in solution and the charging of the electrode, which can be modeled using a resistor-capacitor circuit [18]. The resistance R_{e} due to the electrolyte has previously been found to be inversely proportional to the square root of the active sensing area of the film A_{s}, i.e., $R_{\mathrm{e}} \propto 1/\sqrt{A_{\mathrm{s}}}$ [18]. On the other hand, the capacitance C_{P} of the PEDOT film was found to be proportional to the sensing area, i.e., $C_{\mathrm{P}} \propto A_{\mathrm{s}}$. Thus the rise time, which is given by the product of R_{e} and C_{P}, is $\tau_{\mathrm{r}} \propto \sqrt{A_{\mathrm{s}}}$ [18]. As stated earlier, our PEDOT films have an area of $A_{\mathrm{s}} = 28.3\,\mathrm{mm}^2$. For these films, we find a rise time of $\tau_{\mathrm{r}} = (47 \pm 2)\,\mathrm{ms}$. We can use this to predict the response time for typical cells that we will encounter later. For example, a large cardiomyocyte with an area of $2000\,\mu\mathrm{m}^2$ would be expected to have $\tau_{\mathrm{r}} = 0.4\,\mathrm{ms}$. This response time would be fast enough for microscope ECORE to be able to detect action potentials from this cardiomyocyte.

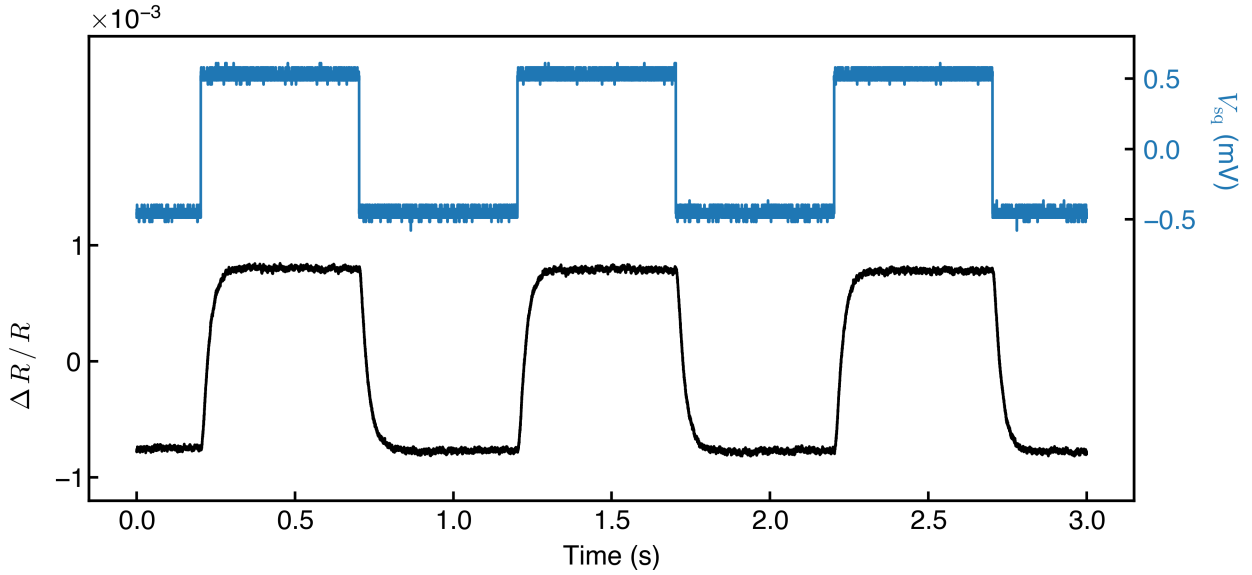

Figure 5.1: A square wave with $V_{\text{pp}} = 1\,\text{mV}$ (blue trace) is applied to a PEDOT film at $V_{\text{bias}} = 0\,\text{mV}$. The resulting microscope ECORE recording of this applied potential is also shown (black trace).

Throughout this chapter, we will look at cell-free recordings like this one to study microscope ECORE and to evaluate its performance. A good recording should show the following characteristics:

- The shape of the recording closely matches the applied potential
- The film shows good sensitivity to the applied potential, i.e., $\Delta R/R$ is high for a given applied potential
- The recording has a high SNR (we typically prefer SNR > 100 for $V_{\text{pp}} = 1\,\text{mV}$)

5.3 Sample optimizations for microscope ECORE

Over the course of the development of microscope ECORE, we performed several optimizations to the PEDOT samples to improve the sensitivity of the samples and enable better recordings.

5.3.1 PEDOT deposition method and input polarization

There are a few ways in which PEDOT can be deposited on a substrate for use in ECORE experiments. Previous ECORE experiments have used two main methods for the deposition of PEDOT [20]:

- Spin coating: A solution containing a dispersion of PEDOT:PSS is used. The PEDOT is deposited onto the glass coverslip using a spin coater. The sample well is attached after the deposition of the PEDOT
- Electrodeposition: A solution of EDOT monomers and PSS is used and held in the sample well attached to an ITO-coated glass coverslip. Using a potentiostat, EDOT is polymerized to form PEDOT by the application of a voltage, which is then deposited directly onto a conducting ITO substrate

To compare these two methods, we first selected the best PEDOT samples made by each method. The best representative sample for each method was chosen to be the one that gave a good balance of high $\Delta R/R$ and high SNR. For the spin-coated samples, we tested samples prepared with rotational speeds of 1800, 3800, and 5800 rotations per minute (rpm): slower speeds correspond to thicker samples. We found that samples prepared at 1800 rpm gave the highest $\Delta R/R$ and also the best SNR. We compared this spin-coated sample with a sample prepared by performing electrodeposition for 60 s. As we discuss later, this electrodeposition time is close to ideal for the preparation of PEDOT samples.

We also tested the response of each sample to the polarization state of the input light. For this experiment only, we used a half-wave plate positioned just before the TIR lens in Fig. 4.2(a) to vary the input polarization of light. We then applied square waves with $V_{\text{pp}} = 10\,\text{mV}$ and $V_{\text{bias}} = 0\,\text{mV}$ to each of these samples and measured the response. The results are shown in Fig. 5.2.

We find that both types of samples have a higher sensitivity to S-polarized input light than to P-polarized input light. However, the electrodeposition sample is relatively insensitive to the input polarization, while the spin-coated sample is highly sensitive, with its response being about 5× stronger for S-polarized compared to P-polarized input light. These differences can be understood using the transfer matrix method discussed earlier, together with the fact that the spin-coated and electrodeposited films will possess different complex refractive indices and film thicknesses. Since both of these are important factors in determining the reflectance for S- and P-polarized light, the optical responses of the two polarizations can differ substantially between the two types of films.

Regardless of the input polarization, we also see that the electrodeposited PEDOT sample shows a significant increase in $\Delta R/R$ compared to the spin-coated sample. For this reason, and for the relative insensitivity of the sample to input polarization, we use electrodeposition to prepare PEDOT samples for all future experiments. Because the electrodeposited samples are not very sensitive to the input polarization, we generally do not vary the input polarization of light in other experiments.

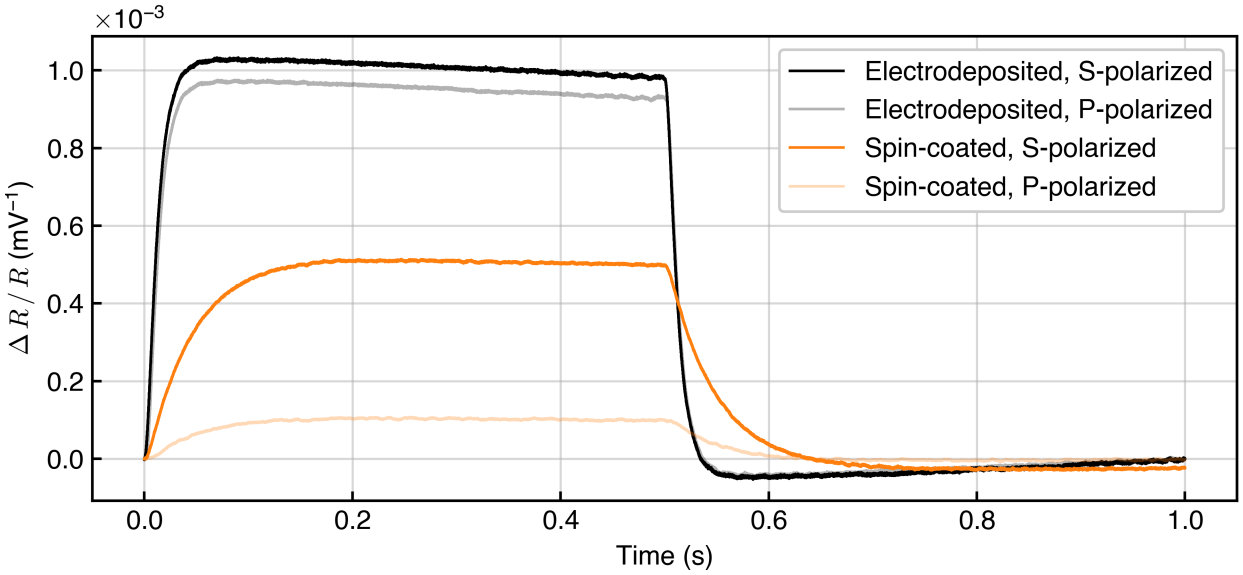

Figure 5.2: A square wave with $V_{\text{pp}} = 10\,\text{mV}$ is applied to two different PEDOT films at $V_{\text{bias}} = 0\,\text{mV}$. The black curves show recordings from the electrodeposited sample while the orange curves show the recordings from the spin-coated sample. In both cases the darker curves shows the response to S-polarized input light while the lighter curves are responses to P-polarized input light. The recordings have been aligned at time $t = 0\,\text{s}$ and grid lines have been included to facilitate comparisons between the different recordings.

5.3.2 PEDOT and PProDOT comparison

Earlier in this dissertation, we introduced PProDOT as a viable alternative to PEDOT. In particular, previous experiments comparing PEDOT to PProDOT in a traditional ECORE setup using light of wavelength 561 nm have shown that PProDOT gives a $\sim 2\times$ improvement in the detection limit [20] (see table 3.2). Since previous experiments with PProDOT have shown strong results versus PEDOT, we also compared the performance of both materials in microscope ECORE. As a representative sample of PEDOT, we used a sample where electrodeposition had been performed for 40 s. This was compared to a PProDOT sample which was prepared according to the method outlined in [20].

The results of this comparison are shown in Fig. 5.3. When tested in the microscope ECORE setup, with the same applied potential, we find that PEDOT shows a $\Delta R/R$ that is approximately $2.4\times$ higher than that of PProDOT. This result is opposite to what has been previously observed. One possible reason for the weaker response of PProDOT compared to PEDOT could be the different wavelength used in microscope ECORE (510 nm) compared to previous experiments with PProDOT (561 nm). While PProDOT remains an exciting material for use in ECORE experiments, we find PEDOT demonstrates good sensitivity in

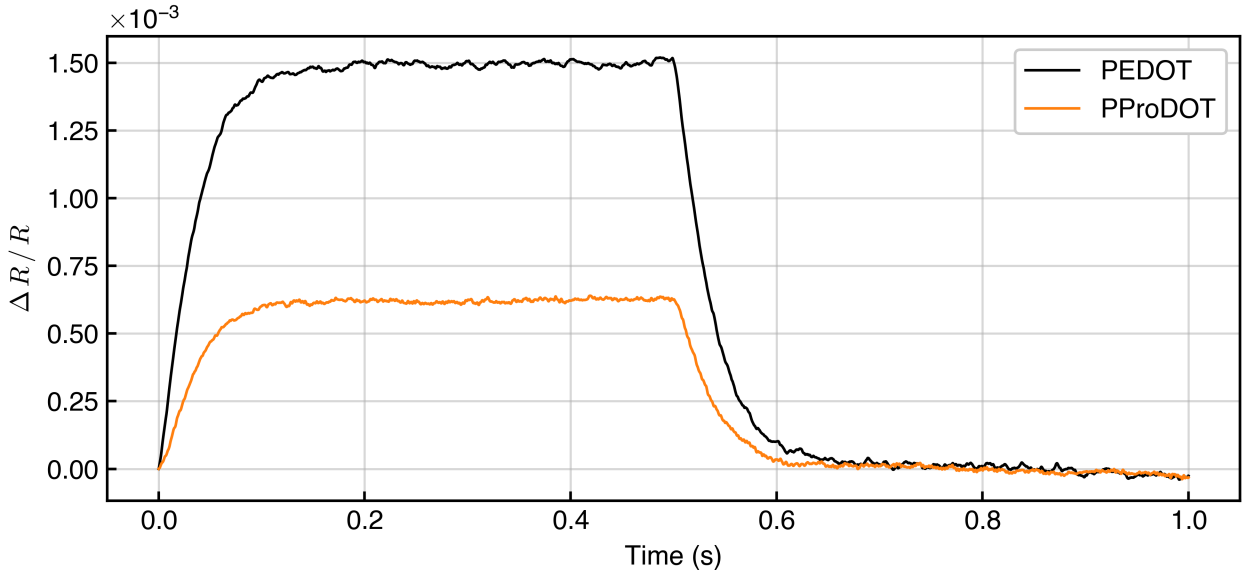

Figure 5.3: A square wave with $V_{\text{pp}} = 1\,\text{mV}$ is applied to a PEDOT sample and a PProDOT sample at $V_{\text{bias}} = 0\,\text{mV}$. The recordings have been aligned at time $t = 0\,\text{s}$ and grid lines have been included to facilitate comparisons between the different recordings.

our setup and therefore use only PEDOT in microscope ECORE experiments.

5.3.3 Thickness of PEDOT thin films

Having tested a few different types of materials and deposition techniques, the final step in the optimization of samples for microscope ECORE is to produce electrodeposited PEDOT samples that give the best response to an applied potential. Specifically, previous experiments have found that the thickness of the PEDOT thin film can have a significant impact on the $\Delta R/R$ magnitude of the recording [18, 19]. We therefore vary the electrodeposition time from the protocol mentioned earlier to produce samples with varying thicknesses of the PEDOT film.

We prepared samples with different PEDOT film thicknesses by performing electrodeposition for 20 s, 40 s, 60 s, and 80 s. A profilometer (Dektak XT-S, Bruker) was used to measure the film thickness by creating a step edge on a sample (using a razor blade) and then scanning perpendicular to the resulting valley to determine the height difference between the coated and uncoated regions. Thickness was measured at 5 different points on each sample, and the average of these measurements was taken to determine the PEDOT thickness of each sample. The average thickness for each of the 4 electrodeposition times was determined to be $(25 \pm 8)\,\text{nm}$, $(51 \pm 6)\,\text{nm}$, $(70 \pm 6)\,\text{nm}$, and $(94 \pm 6)\,\text{nm}$, respectively. These results are summarized in table 5.1.

Deposition time (s)	Average thickness (nm)	Standard deviation (nm)
20	25	8
40	51	6
60	70	6
80	94	6

Table 5.1: Thickness of PEDOT films versus electrodeposition time on ITO-coated coverslip substrates.

To record the response of each sample, we applied a square wave signal with $V_{\text{pp}} = 1\,\text{mV}$ and $V_{\text{bias}} = 0\,\text{mV}$. The $\Delta R/R$ magnitude was determined for each film and the results are shown in Fig. 5.4. We observe an increase in $\Delta R/R$ as the thickness of PEDOT is increased. This behavior can be understood using the transfer matrix method, where increasing the thickness of a layer modifies the phase accumulation according to eq. (3.30), thereby altering the interference of reflected fields within the film. As a result, the reflectance R becomes more sensitive to electrochromic-induced changes in the complex refractive index, which can lead to an enhanced $\Delta R/R$.

We also see a decrease in the reflectance R of the samples with increasing PEDOT thickness. While optimizing $\Delta R/R$ is generally important, we must also keep in mind the higher absorption that occurs with thicker samples. As the samples get thicker and R is reduced, more light must be sent to the sample to get the same amount of light back on the signal photodiode of the detector. This signal power is important as lower powers reduce the SNR of a recording. However, increasing the power for thicker samples also increases the amount of light that is absorbed by the sample. This extra power can heat up the PEDOT film and cause damage to any cells deposited on top of the PEDOT. We therefore find a good balance of high $\Delta R/R$ and R for PEDOT films with a thickness of $\sim$50 nm. This balance gives a good sensitivity ($\Delta R/R$) to applied potentials while still allowing a high SNR due to a relatively high value of R. Thus PEDOT films are prepared with this thickness to optimize recordings and prevent excessive heat from being deposited in the sample.

5.4 PEDOT response to applied voltages

Having optimized the PEDOT samples, we now look at the response of PEDOT to different values of V_{app}. Specifically, we separately vary V_{bias} and $V_{\text{sq}}(t)$ from eq. (5.1). This helps us determine the type of response that may be expected from cellular samples.

5.4.1 Bias voltage

We have already mentioned the important role that the bias potential V_{bias} plays in our effort to approximate bioelectric potentials. We expect from previous iterations of ECORE that

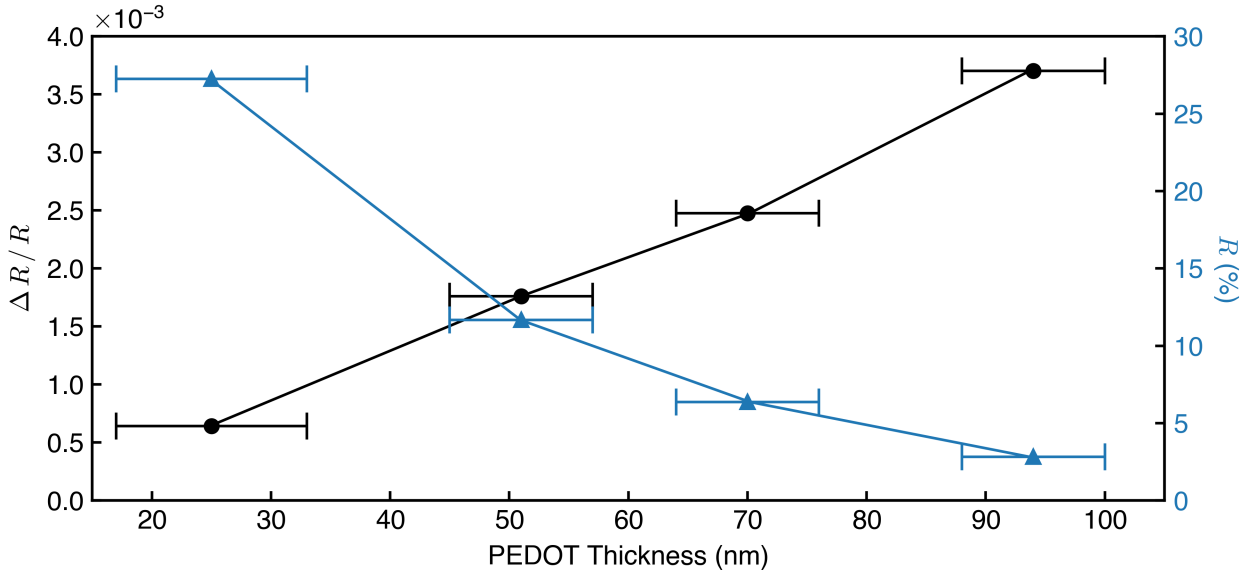

Figure 5.4: A square wave with $V_{\text{pp}} = 1\,\text{mV}$ is applied to PEDOT sample of varying thicknesses at $V_{\text{bias}} = 0\,\text{mV}$. The average values of $\Delta R/R$ and R are determined for each recording and are plotted as black circles and blue triangles, respectively. The horizontal bars on each data point represent the uncertainty in the thickness measurements.

$\Delta R/R$ will have some dependence on V_{bias} [18–20]. We tested this dependence by applying a few different bias voltages to a PEDOT sample. The results are shown in Fig. 5.5.

We see that $\Delta R/R$ increases with decreasing bias voltages, in good agreement with previous experiments [18, 19]. As we mentioned previously, cellular open circuit potentials are $\sim -50\,\text{mV}$. In principle, it should be possible to bias biological samples to achieve a higher $\Delta R/R$. For example, we can see from Fig. 5.5 that holding the sample at a bias voltage of $-200\,\text{mV}$ rather than $-50\,\text{mV}$ increases the $\Delta R/R$ in response to the same applied voltage V_{pp}. However, large deviations from the open circuit potential for cells can be perturbative [12], so this is not preferred. We will therefore elect not to apply a bias potential when working with the cellular experiments presented in the next chapter. This also has the added advantage that we do not need to use a potentiostat at all to apply a bias voltage when working with cellular samples.

To approximate these cellular conditions, we could elect to carry out cell-free experiments with a bias voltage of $-50\,\text{mV}$. However, we note from Fig. 5.5 that the difference in $\Delta R/R$ at $V_{\text{bias}} = -50\,\text{mV}$ and $V_{\text{bias}} = 0\,\text{mV}$ is not very large. For simplicity, we therefore elect to carry out the majority of cell-free experiments with a zero bias voltage, as previous iterations of ECORE have also done [18].

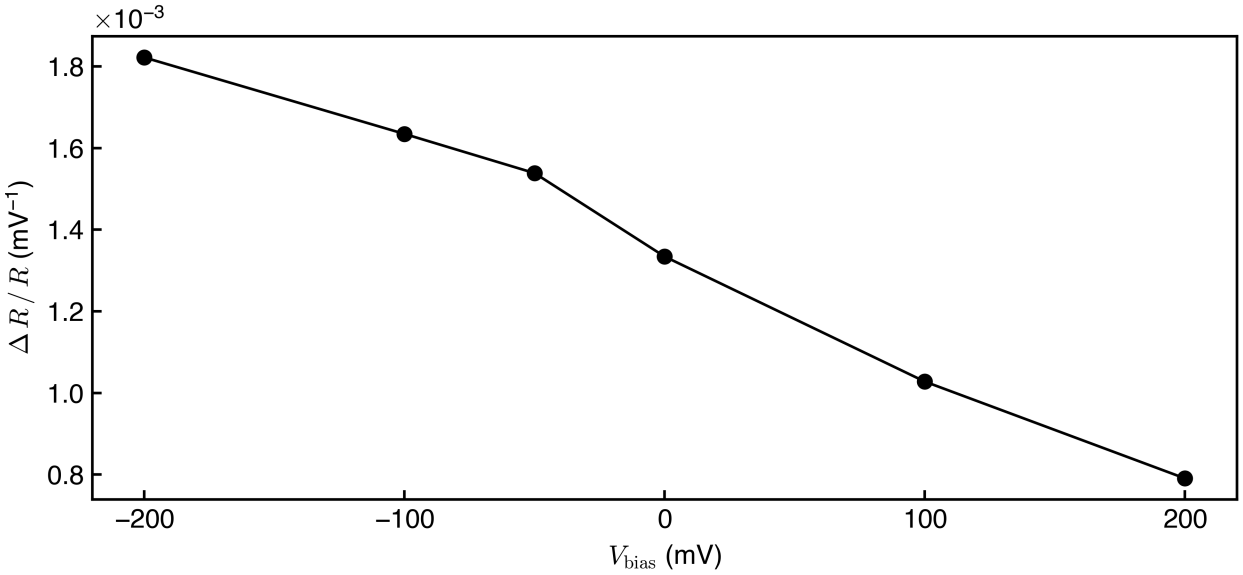

Figure 5.5: Square wave signals with $V_{\text{pp}} = 10\,\text{mV}$ are applied to a PEDOT film at varying values of V_{bias}. The $\Delta R/R$ value is determined for each square wave signal and is divided by $V_{\text{pp}} = 10\,\text{mV}$ to facilitate comparison with other experiments where $V_{\text{pp}} = 1\,\text{mV}$. These values are shown as the black dots in the figure.

5.4.2 Magnitude of the applied square wave

While the bias voltage determines the baseline operating conditions of the experiment, the more important component of the applied signal is the square wave, characterized by V_{pp}. Extracellular action potentials produce rapid voltage fluctuations on the order of $\sim$100 µV, whereas the open-circuit potential of the cellular medium remains comparatively stable over time. The extracellular signal can therefore be viewed as a small, rapidly-varying voltage superimposed on a constant bias potential. In addition, the action potentials of many cells, particularly cardiomyocytes, occur periodically with an approximately regular frequency. We therefore approximate extracellular activity by applying a small cyclic voltage to the sample. This is achieved by applying a square wave signal with a peak-to-peak magnitude of V_{pp} to a PEDOT sample. Compared with other periodic waveforms such as sinusoidal signals, the sharp transitions of a square wave more closely reproduce the rapid changes in extracellular potential associated with membrane depolarization.

In addition to requiring that the setup detect small potentials, it is desirable that the PEDOT response vary in a predictable manner so that it can serve as a quantitative proxy for the applied potential. We therefore vary the magnitude of the applied square waves over a large range, from $V_{\text{pp}} = 200\,\mu\text{V}$ (around the magnitude of a large extracellular action potential) to $V_{\text{pp}} = 20\,\text{mV}$. For each value of V_{pp}, we determine the $\Delta R/R$ of the recording.

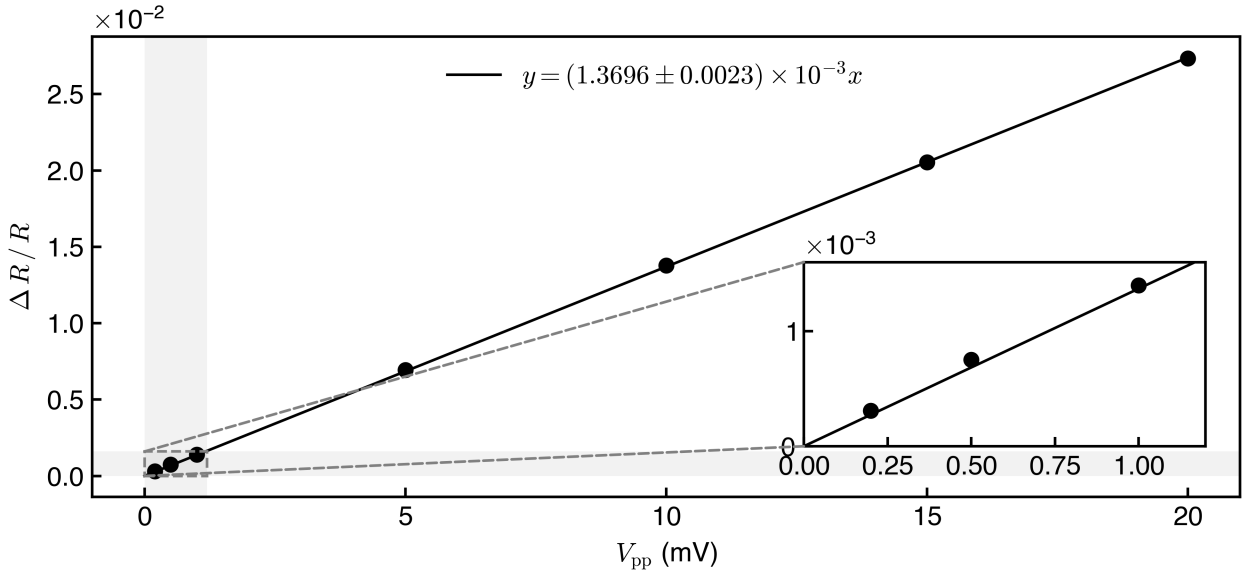

Figure 5.6: Square waves are applied to a PEDOT film at $V_{\text{bias}} = 0\,\text{mV}$ with varying values of V_{pp}. The $\Delta R/R$ value is determined for each square wave signal and is plotted here (black dots). The black line is a linear fit to the data described by the equation shown in the legend. The inset shows data points near the origin.

The results of this experiment are shown in Fig. 5.6.

We find that the response of the PEDOT sample is highly linear, as shown by the fit equation, and in agreement with previous experiments [18, 20]. The linear response of the PEDOT means that $\Delta R/R$ can be used as a representative proxy variable for the applied voltage V_{pp}. It also means that it is possible to calibrate any PEDOT film to specify the exact relationship between $\Delta R/R$ and V_{pp}. Doing so enables us to draw quantitative conclusions about the magnitude of the electrical signals detected using microscope ECORE. However, in practice, calibrating every PEDOT sample is time-consuming and we will therefore continue to work with $\Delta R/R$ rather than calibrate each film. This will not present any issues since PEDOT shows a very linear response to applied voltages.

We can now turn our attention to the important question of whether microscope ECORE is capable of measuring the small extracellular action potentials of cells.

5.5 Microscope ECORE performance

We have demonstrated that our samples are optimized to respond with a high $\Delta R/R$ while still maintaining a relatively high reflectance R. We have also shown that these samples respond to applied potentials in a predictable manner. However, to successfully record the

small extracellular potentials of cells, we also need to demonstrate recordings with high SNRs. We can use the square wave recordings in cell-free experiments to determine whether our setup will be able to record extracellular action potentials from cells.

After finding the best samples and taking steps to reduce the technical noise in the setup — using the methods described throughout this dissertation — we arrive at an optimized microscope ECORE that can now be evaluated for its detection capabilities. In particular, we must characterize the noise of a typical recording from the optimized setup. Due to the low powers typically incident on the photodiodes of the detector (typically 10 µW to 100 µW), shot noise plays a significant role in the overall noise of the signal recorded by the detector.

The shot noise associated with a current I has current spectral density $S_I(f)$ given by the following equation [60]:

$$S_I(f) = \sqrt{2eI}\,, \tag{5.2}$$

where f is the frequency and e is the elementary charge. Combining this with the photodiode current (eq. (3.49)), the voltage spectral density $S_V(f)$ of the shot noise becomes

$$S_V(f) = \sqrt{2eP\mathcal{R}}R_\mathrm{f}\,, \tag{5.3}$$

where P is the light power falling on the photodiode, $\mathcal{R}$ is the responsivity of the photodiode, and R_f is the feedback resistance used to convert the photocurrent into a voltage. As we use a physical low-pass filter, we must also take this into account. When this signal passes through a filter with transfer function $G(f)$, the above equation becomes

$$S_{V,G}(f) = \sqrt{2eP\mathcal{R}}R_\mathrm{f}|G(f)|\,. \tag{5.4}$$

For the passband of the filter, $|G(f)| = 1$, and the voltage spectral density of the shot noise is

$$\mathrm{VSD}_\mathrm{shot} = \sqrt{2eP\mathcal{R}}R_\mathrm{f}\,. \tag{5.5}$$

This represents the shot noise associated with a single photodiode. However, in our experiment we use a balanced detector, which outputs the difference signal of two photodiodes with very similar light powers falling on them. Because shot noise arises independently in each photodiode, the noise contributions from the two currents add in quadrature in a balanced detector configuration, resulting in an overall noise level that is higher by a factor of $\sqrt{2}$ compared to a single photodiode. Thus, the expression above must be further multiplied by $\sqrt{2}$ for our detector to obtain the final expression:

$$\mathrm{VSD}_\mathrm{shot} = \sqrt{4eP\mathcal{R}}R_\mathrm{f}\,, \qquad \text{(Balanced detector)} \tag{5.6}$$

where P is the light power falling on one photodiode. Using eq. (3.49) and eq. (3.52), we can also write the above expression as

$$\mathrm{VSD}_\mathrm{shot} = \sqrt{4eV_\mathrm{DC}R_\mathrm{f}}\,, \qquad \text{(Balanced detector)} \tag{5.7}$$

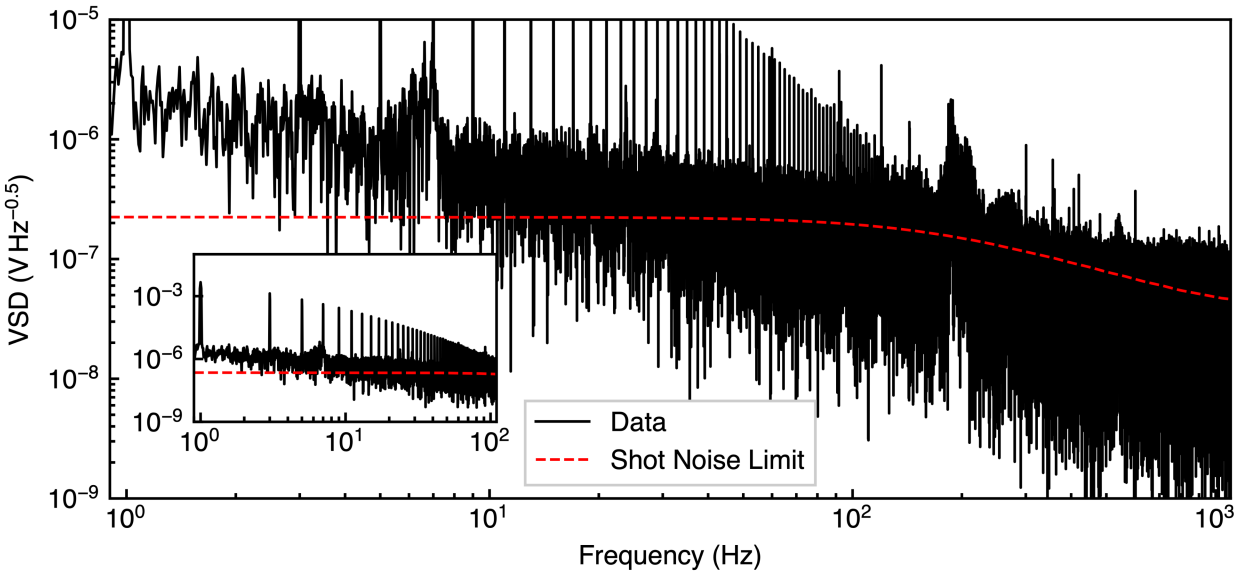

Figure 5.7: A square wave with $V_{\mathrm{pp}} = 1\,\mathrm{mV}$ is applied to a PEDOT film at $V_{\mathrm{bias}} = 0\,\mathrm{mV}$ for a duration of 100 s. The voltage spectral density (VSD) of the recording is plotted in black while the dashed red line shows the estimated shot noise level. The inset shows the VSD in a smaller frequency range and an extended VSD range.

where V_{DC} is the detector voltage when one photodiode is illuminated and the other is blocked (i.e., the steady-state voltage corresponding to a single photocurrent). Because this formulation depends only on the measured quantities V_{DC} and R_{f}, it eliminates explicit dependence on the responsivity $\mathcal{R}$, allowing the shot noise level to be predicted without prior knowledge of the photodiode quantum efficiency.

To characterize the noise and compare it to the expected shot noise level, we recorded the response of a PEDOT sample to the application of a square wave signal with $V_{\mathrm{pp}} = 1\,\mathrm{mV}$ and $V_{\mathrm{bias}} = 0\,\mathrm{mV}$. The shot noise level can be determined using the equations above, along with the filter response over some frequency range. The power of light incident on the signal photodiode of the detector for this experiment was $P_{\mathrm{sig}} = 44\,\mu\mathrm{W}$, giving a passband shot noise level of $\mathrm{VSD}_{\mathrm{shot}} = 2.24 \times 10^{-7}\,\mathrm{V\,Hz}^{-0.5}$. The voltage spectral density of the recorded signal, along with the shot noise level is shown in Fig. 5.7.

At lower frequencies, the noise of the recording is about one order of magnitude higher than the shot noise limit, while at higher frequencies the recording is shot noise limited. We see that there is some room for improvement in the setup at lower frequencies. However, in practice, reducing noise at lower frequencies is quite difficult as much of this noise comes from lower frequency environmental sources.

Having already taken steps to mitigate this environmental noise in the experimental setup, we utilize digital filtering to further reduce noise. This is a common procedure that

has been utilized in previous ECORE experiments [19, 20]. Starting with the full recording that was used to generate the VSD in Fig. 5.7, we apply a 0.01 Hz first-order high-pass Bessel filter to reduce low frequency noise and help flatten the baseline of the recording. We also apply a 280 Hz third-order low-pass Bessel filter to reduce high frequency noise, as has been done previously in the dual-color ECORE experiment [19]. After these filters have been applied, we determine the SNR of the recording using the following steps:

1. For a given cycle of the response, determine the time value associated with the half-amplitude of the cycle. This is done by applying a Gaussian filter to smooth the data and then determining the peak of its derivative

2. Perform a linear fit to the data points in two 25 ms regions, 200 ms on either side of the half-amplitude time. The standard deviation of the difference between the data points and the linear fit represents the noise in that region. The average of these two standard deviations is the noise for that cycle

3. The difference between the average $\Delta R/R$ in each region gives the signal strength for that cycle

4. Using the definition of SNR in eq. (3.53), the SNR for the cycle is the ratio of the signal strength to the noise determined in the preceding two steps

5. The steps above are repeated to determine the SNR for each cycle in the full recording. The mean SNR of all of the cycles is taken to be the SNR of the recording

The procedure above is illustrated in Fig. 5.8(a), and the results for the full 100 s recording are shown in Fig. 5.8(b). In this optimized recording, the mean SNR is determined to be $\mathrm{SNR}_{\mathrm{mean}} = 334$. Using our previous definition of the detection limit (eq. (3.54)), we therefore have

$$\text{Detection Limit} = \frac{1}{334\,\mathrm{mV}^{-1}} = 3\,\mu\mathrm{V}\,. \qquad \text{(Microscope ECORE)} \tag{5.8}$$

With a detection limit of 3 µV, microscope ECORE surpasses the previous best detection limit of 3.3 µV (see table 3.2 for a summary of previous ECORE methods). This result is important as it demonstrates that microscope objectives can be used in ECORE without compromising recording quality, while also simplifying the experimental configuration and making the approach more accessible for implementation by other researchers. Moreover, the performance is not only preserved but improved compared to previous implementations, despite the setup not being at the shot noise limit at lower frequencies.

The detection limit above is achieved through a combination of noise reduction and other optimizations to the setup. With this detection limit, microscope ECORE should be able to detect the small extracellular action potentials that are generated by biological cells. In the next chapter, we demonstrate our experiments using microscope ECORE to record action potentials from cardiomyocytes.

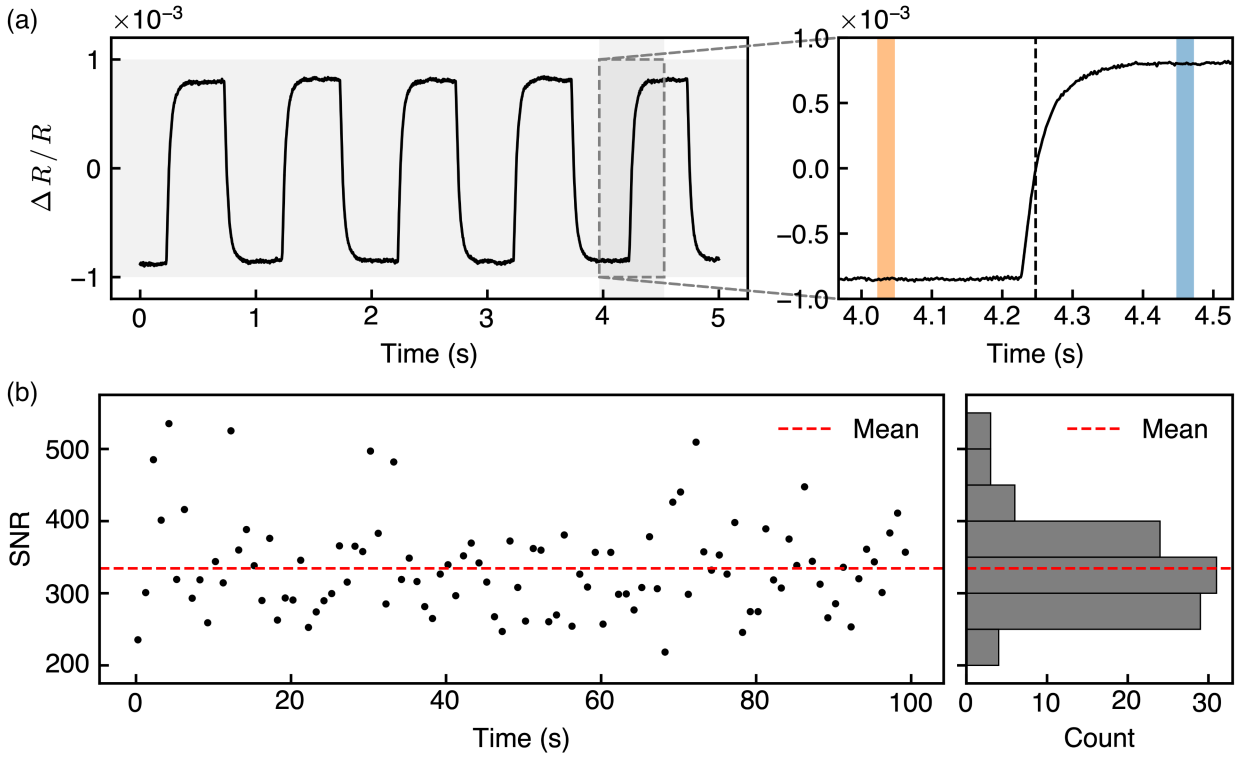

Figure 5.8: The SNR is determined for the same square wave recording that is used to generate the VSD in Fig. 5.7. (a) A 5 s section of the recording is shown on the left. The right panel illustrates the procedure for determining the SNR of the fifth cycle on the left. The dashed black line is the half-amplitude time of the cycle determined using the procedure described in the main text. The orange and blue highlighted sections are 25 ms regions located 200 ms from the black line and represent the regions that are used to determine the SNR of the cycle, as described in the text. (b) The SNR for each of the 100 cycles is shown on the left. The dashed red line shows the mean of all 100 SNRs ($SNR_{mean} = 334$). The right panel shows a histogram of the plot on the left.

Chapter 6

Cellular Recordings with Microscope ECORE

Note: Major portions of this chapter are based on a manuscript submitted to a peer-reviewed journal. A preprint is available [52].

In this chapter, we describe experiments performed using microscope ECORE to record action potentials from cardiomyocytes. We stress that the setup must first be optimized as described in the preceding two chapters, given the small magnitudes of extracellular action potentials and the increased susceptibility to noise when using high-NA objectives.

6.1 Setup and sample considerations

The majority of the experimental setup introduced in the previous two chapters carries over when performing cellular experiments. However, as we now attempt to record from biological samples, a few notable changes are made to the setup and the procedures that we follow:

- Cardiomyocytes are cultured on top of the PEDOT films, and cell culture media is used instead of a solution of PBS
- A potentiostat is no longer used in any capacity
- A cardiomyocyte sample is only recorded on the setup for ∼30 min and then returned to an incubator
- Any particular region of the cardiomyocyte sample is recorded for no more than 3 min to prevent light-induced damage to the cells

Sample preparation in cellular experiments follows the same initial procedure as in cell-free experiments. That is, the PEDOT samples are prepared in the same manner for both types of experiments. However, in cellular experiments, once a PEDOT sample is prepared, we perform additional steps to deposit and culture cells on top of the PEDOT film. This culturing procedure has been described in detail in a previous ECORE experiment [20]. Using this protocol, we culture human induced pluripotent stem cell (hiPSC)-derived cardiomyocytes on the PEDOT samples. These cardiomyocytes are good model cells to study as they exhibit regular, spontaneous potentials. They have also been extensively researched, both in previous experiments done in our labs and by other researchers, and therefore provide a good benchmark by which to test the performance of microscope ECORE.

In the previous chapter, we mentioned the motivation for not using a potentiostat for cellular experiments. In addition to avoiding any perturbations to the cells, not using a potentiostat makes loading the cardiomyocyte sample onto the microscope ECORE setup a lot simpler and faster as no external electrodes need to be inserted into the cell culture media. This also greatly reduces the chances of introducing contaminants into the samples from the electrodes.

We must also consider the health of the cardiomyocytes themselves — a concern we do not encounter with cell-free samples. For the cardiomyocytes to stay healthy, the samples must generally be kept at 37 °C. However, like all previous ECORE setups, microscope ECORE is run at room temperature due to the lack of an incubator on our microscope base. Therefore, to perform experiments with the cardiomyocytes, the samples must be removed from the incubators in which they are stored. They are first covered with a sterile transparent dish to prevent contamination from the air and other setup surfaces, and then loaded onto the microscope ECORE setup, where recordings are made at room temperature. This does not prove to be a major issue as long as the sample is not kept at room temperature for too long. In our experience, cardiomyocyte samples will exhibit signals for ∼30 min before they start to show signs of permanent damage. If a cellular sample is kept at room temperature for much longer than this, then returning it to the incubator will not be sufficient to bring the cells back to a healthy state, destroying the sample altogether. Therefore, with every cardiomyocyte sample, we attempt to transfer it to the setup quickly, record data for ∼30 min, and then promptly return it to the incubator for recovery. After recovering for around 1 to 2 days, the cells may be recorded again.

We also exercise great care in keeping the samples clean. In addition to covering the samples during the experiment, they must also be handled appropriately, especially while removing them from the incubator and loading them onto the sample mount. This transfer process provides many opportunities for bacteria and other contaminants to damage the cells. Therefore, we clean all equipment that touches the samples using a 70 % solution of ethanol or isopropanol. We also regularly observe the cells under a microscope to ensure their health, especially before a recording session.

Finally, we also have to adjust how long our signal beam is incident on an given region of a cardiomyocyte sample. This is because the reduction of the spot size achieved using microscope ECORE, while desired to improve the spatial resolution, also increases the light

intensity impinging on the sample. While some light is reflected (generally ∼10 % for the PEDOT thicknesses we use), the rest is absorbed through multiple reflections within the thin layer of PEDOT at the sample interface. The energy of the absorbed light is converted into thermal energy within the material, leading to local heating of the sample. In fact, this light-induced heating affect has been observed in previous ECORE experiments, with the original ECORE experiment using it to investigate how different light intensities affect the frequency of neuronal action potential firing [18].

In earlier implementations of ECORE, the beam was much larger than that used in microscope ECORE, resulting in a lower intensity at the sample and no observable damage. Under these conditions, thermal effects were not limiting, as the optical energy was distributed over a relatively large spot. In contrast, the greatly increased light intensity in microscope ECORE imposes stricter constraints on allowable illumination times and operating conditions. This introduces practical limitations to avoid excessive local heating during measurements. With the prospect of achieving significantly smaller spot sizes — in principle approaching the diffraction limit — these considerations become increasingly important in the design and operation of microscope ECORE. With our spot size of $12.9 \times 9.4\,\mu m^2$, we will find that we can record from a given region of the sample for ∼3 min before we start observing damage to the cells. Therefore, we try to limit the recording duration in any region we are probing to < 3 min.

6.2 Action potential recordings

Once a cardiomyocyte sample has been loaded onto the setup for recording, we use the camera to observe the sample in the field of view (FOV) of the objective. The sample can be easily translated perpendicular to the optical axis to change the area of the sample we are observing at any give time. A region of interest (ROI) is determined, which may be a particular cell or a group of cells. To record from the ROI, we move the sample so that the known location of the beam coincides with the ROI. In practice, we use a shutter to block the signal beam until we are ready to record — this is done to prevent light-induced damage to that region of the sample while we are not recording. Once the ROI has been aligned with the beam, we open the shutter and obtain the reflection of the signal beam on the signal photodiode. The second half-wave plate in Fig. 4.2(a) is then rotated to balance the light powers on both photodiodes of the detector. This balancing must generally be repeated for each ROI due to the location-dependent R value. Once the light powers are balanced, the detector output is monitored using the digitizer (and simultaneously recorded for later analysis). We repeat this process to typically record ∼ 10 ROIs from a sample for 1 min each before removing the sample and returning it to the incubator for recovery.

A section of a recording from one cardiomyocyte is shown in Fig. 6.1. The periodic nature of the cardiomyocyte signals is evident, with features repeating every ∼5 s for this cell. These observed features are consistent with previous ECORE recordings of similar cardiomyocyte samples [18–20]. In particular, the sharp features have been previously identified as the

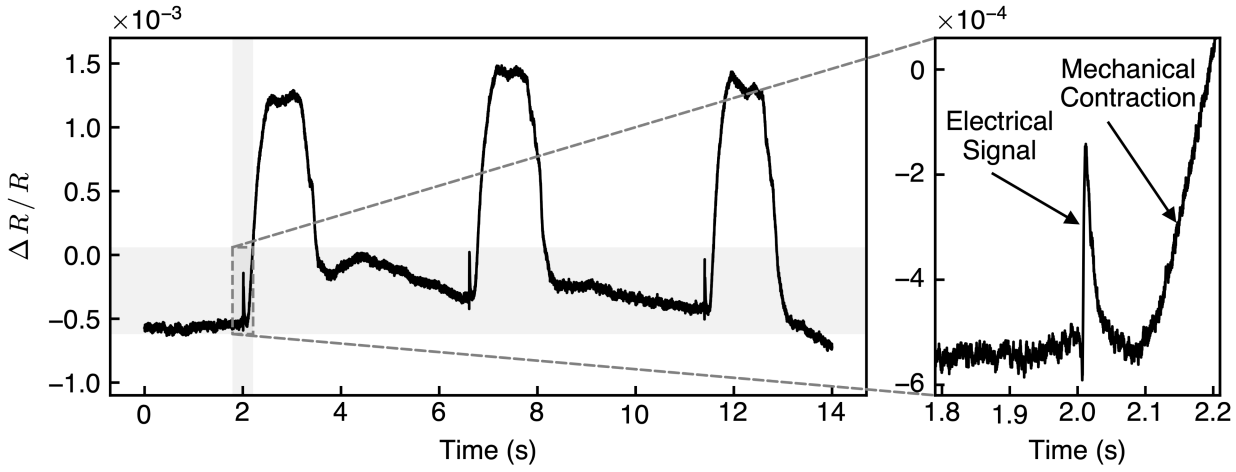

Figure 6.1: A 14 s microscope ECORE recording of a cardiomyocyte is shown on the left. When zooming-in to a section of the data (on the right), we can clearly identify the electrical signal associated with the action potential as well as the mechanical signal associated with movement of the cardiomyocytes.

electrical signals from the cells (i.e., the extracellular action potentials) [18]. Focusing on these sharp signals, as is done in the right part of Fig. 6.1, we indeed find that the time scale of the feature is consistent with the rapid depolarization that occurs in action potentials.

The electrical signals precede larger, more prolonged features — these are identified as the mechanical contractions of the cell. As we mentioned previously, ECORE detects any changes in the refractive indices of the multilayer sample. While we are interested in the electrochromic signals (that is, the index changes of PEDOT associated with extracellular potentials), we also detect changes in the refractive indices of other materials in the sample. In the case of these mechanical contractions, the movement of the cells leads to a small change in the local refractive index of the cell, changing the reflectance R and enabling detection of the contraction in addition to the action potential. In the following experiment, we confirm that these signals are mechanical in nature.

6.3 Identification of electrical and mechanical signals

We repeat an experiment previously carried out with the original ECORE setup [18]. In this experiment, a drug is introduced into the cell culture medium to suppress mechanical contractions while preserving electrical activity, therefore reducing motion-related effects in the measurements. Blebbistatin is used for this purpose, as it inhibits contraction without significantly affecting the electrophysiological properties of cells [61].

We add a 20 µM solution of blebbistatin to a cardiomyocyte sample at $t = 0$ min. We

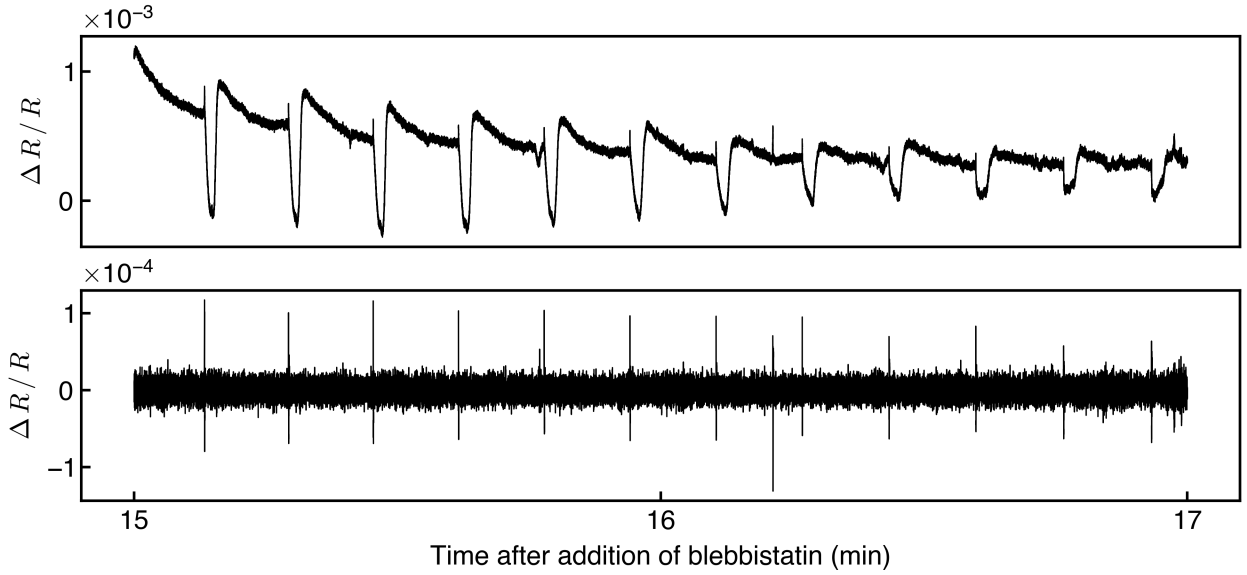

Figure 6.2: The top panel shows the recording of a cardiomyocyte after the addition of blebbistatin at $t = 0\,\mathrm{s}$. The larger signals are reduced over time. The bottom panel shows a filtered version of the signal shown in the top panel. The filter applied further suppresses the larger, prolonged signals and makes the sharper signals more clear.

then record for $\sim$2 min from any one region of the sample before moving to another region and repeating this process to obtain a longer recording of the sample. This helps prevent light-induced damage to the cells. After monitoring the sample signals for $\sim$15 min, we find a region where the cells start to show a clear decrease in the larger, longer features. This is shown in Fig. 6.2.

The top panel in Fig. 6.2 shows the recording from the cell being observed at $\sim$15 min. We see that, over the course of 2 min, the larger-magnitude signal decreases significantly while the sharply-peaked signal that precedes each of the larger signals persists and remains detectable. This reduction of the larger signal is consistent with the reduction in contraction caused by the blebbistatin, and provides further evidence that these signals are indeed mechanical in nature.

The persistence of the electrical signal can be made clearer by filtering out the mechanical signals altogether. To do this, we digitally apply 10 Hz high-pass and 280 Hz low-pass filters (both third-order Bessel) to the recording shown in the top panel of Fig. 6.2. In particular, the application of the high-pass filter suppresses the mechanical signals apparent in the top panel. The filtered signal, shown in the bottom panel of Fig. 6.2, demonstrates the clear, persistent presence of the sharply-peaked signal. As the blebbistatin does not affect the electrical properties of the cell, these signals are shown to be electrical in nature. Additionally, as the time scale of these signals is consistent with the time scales associated with action potentials,

we conclude that these features represent the extracellular potentials that we are interested in recording. To clearly identify these electrical signals, we therefore continue to apply these digital filters in future experiments to suppress the signals from the mechanical contractions, which we are less interested in studying.

This experiment also highlights another feature of the microscope ECORE setup — its ability to facilitate interaction with the sample during ongoing measurements. Because both recording and imaging are performed from the bottom of the cell culture medium, where the cells and coverslip are located, the upper surface of the sample remains fully accessible during operation. This allowed blebbistatin to be conveniently introduced while simultaneously recording from the sample. Such accessibility is partly enabled by the inverted geometry, in which light is incident from below, as is also the case in the original prism-based ECORE configuration. However, the key advantage of microscope ECORE is that it enables imaging through the same objective used for electrochromic recording, whereas the original ECORE setup required a separate objective positioned above the sample, thereby limiting access from above. Beyond facilitating solution exchange during recordings, this enhanced accessibility could also be utilized by researchers, for example, to introduce external electrodes into the cell culture medium for simultaneous electrical stimulation.

Having established that the long-duration signals are due to the mechanical contractions, we can reexamine the recording shown in Fig. 6.1 by applying the digital filters mentioned above. The resulting filtered recording is shown in Fig. 6.3. The application of the filters greatly suppresses the mechanical signals, allowing clearer observation of the electrical signals. In particular, we have shown that electrical signals due to extracellular action potentials can be readily identified using microscope ECORE. This demonstrates the effectiveness of the technique in achieving its primary objective — namely, the recording of extracellular action potentials from biological cells. This is consistent with the high detection sensitivity demonstrated in the preceding chapter using cell-free experiments.

6.4 Limits to recording duration

We now return to our earlier discussion of light-induced damage to the cells, which is caused by the excessive heating of the samples accompanying the reduction in the spot size.

We investigated this type of damage by analyzing the effects of prolonged light exposure to a cardiomyocyte. We directed the beam to a healthy cardiomyocyte that was exhibiting clear electrical activity, and then recorded signals from that cell until the action potentials were no longer detectable, indicating damage to the cell. One such experiment is shown in Fig. 6.4. We typically send 600 µW of light into the rear port of the microscope base, which leads to approximately 500 µW reaching the sample due to the losses in the objective. For this incident light power, we see from Fig. 6.4 that the strength of the electrical signal decreases until, at around the 4 min mark, the signal becomes similar in magnitude to the noise. We conclude that we can record from a ROI of the cardiomyocyte sample for at least 3 min before we start to see any major effects of damage to the cells. Nevertheless, this is a

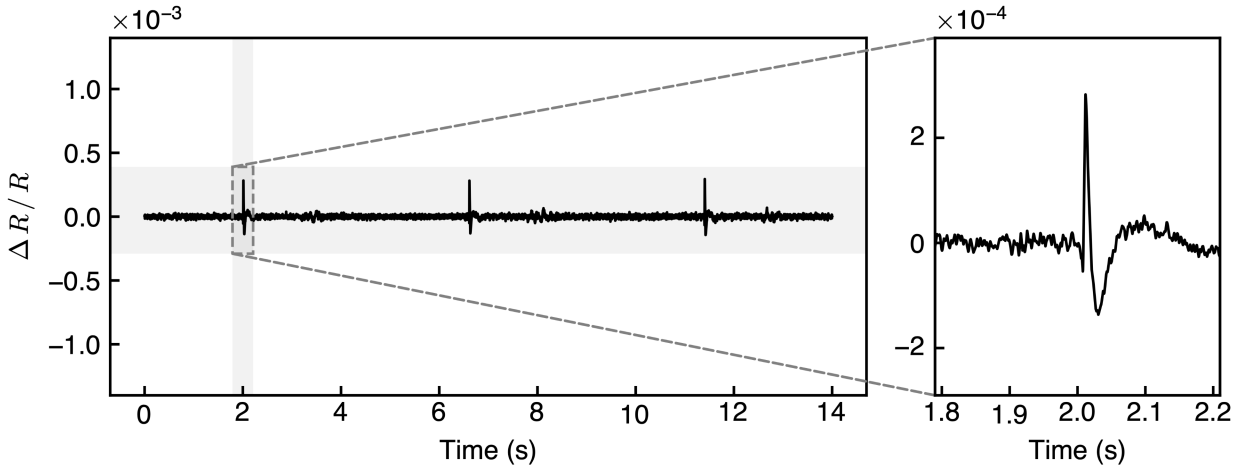

Figure 6.3: The filters mentioned in the text are applied to the recording shown in Fig. 6.1. The mechanical signals are mostly suppressed, allowing the electrical signals from the cardiomyocyte action potentials to be even more clearly identified.

shorter exposure time compared to previous ECORE experiments, which did not have such a time restriction.

As the damage is caused by an increase in light intensity due to the smaller spot size of the beam, the recording duration may be extended by decreasing the incident power. In one experiment, with ∼340 µW incident on the sample, we were able to observe action potentials for about 7 min. However, reducing the power also reduces the overall SNR of the recordings. A balance must therefore be struck between maximizing signal quality and extending the duration over which stable measurements can be obtained. In our experiments, we decided to generally work with ∼500 µW of incident light to achieve good recording quality and to enable the clear identification of action potentials. With this power, we therefore record for no more than 3 min in any given ROI before moving to another spot on the sample. This allows us to acquire sufficient data from any one ROI of the sample without causing irreversible damage to the cells being studied.

While mitigation of this issue is possible by decreasing the incident light power, a more permanent solution may lie in finding materials with high values of both R and $\Delta R/R$. While our PEDOT samples demonstrate high $\Delta R/R$ per mV of an applied potential, they have fairly low reflectances — even the thinnest samples only have $R \sim 27\,\%$ (see Fig. 5.4). A material with much higher R would absorb less energy, which would decrease the damage to the cells from absorbed light. At the same time, the material must show high $\Delta R/R$ in response to applied voltages to be able to detect small action potentials. Identification of such a material would enable longer-term recordings of cells and/or a further reduction in the spot size.

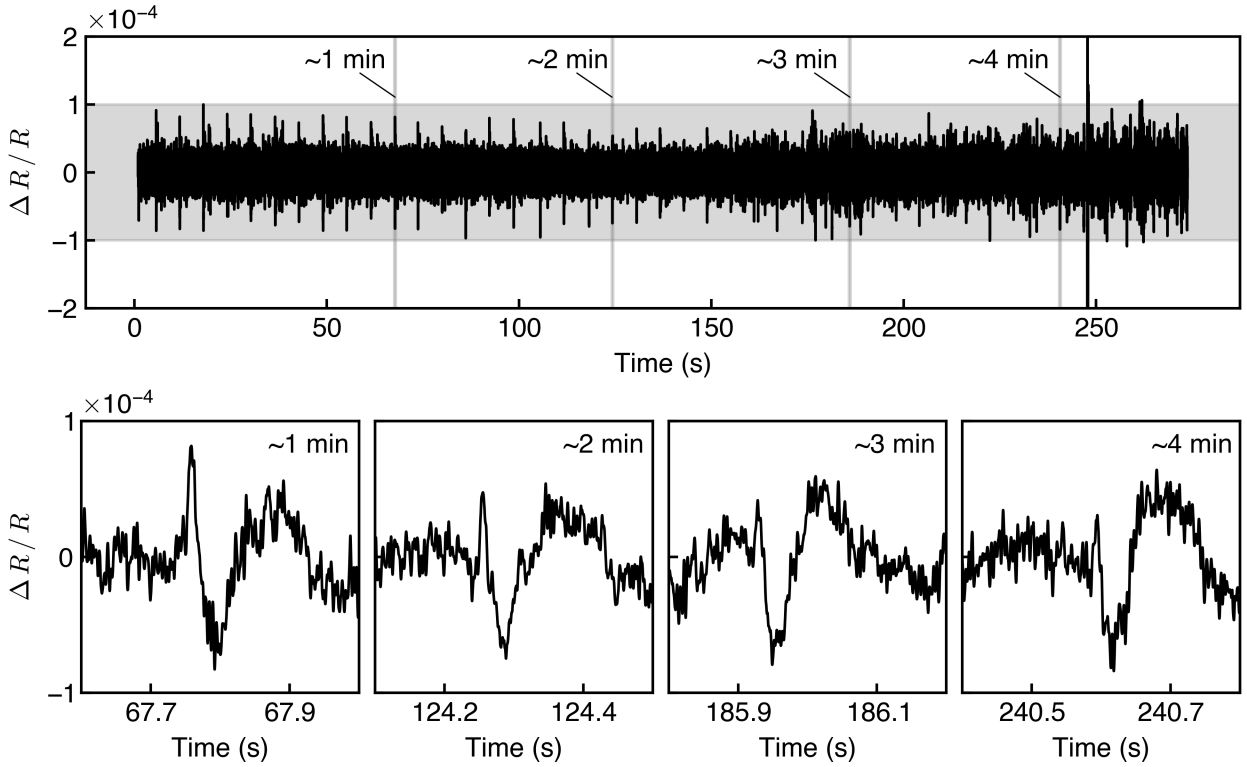

Figure 6.4: The top panel shows a filtered recording from a cardiomyocyte with ∼500 µW of light incident on the sample. The bottom panels show zoomed-in sections from the recording in the top panel. Action potentials at ∼1 min, ∼2 min, ∼3 min, and ∼4 min are shown. The reduction in the strength of the electrical signal over time is clear.

6.5 Spatial mapping of potentials

One major benefit of ECORE compared to extracellular electrode-based techniques such as multielectrode arrays is its spatial flexibility. Because the probing beam is not fixed at a single recording site, the measurement location can be selected dynamically during the experiment. This can be accomplished either by steering the beam to a chosen ROI or, equivalently, by translating the sample so that the desired ROI is brought into alignment with the beam. In either case, the recording position can be adjusted without physically contacting the sample or modifying the device itself. As a result, ECORE allows measurements to be obtained from essentially any arbitrary region of the sample, enabling more versatile recording of cellular activity than is possible with fixed electrode geometries.

Microscope ECORE has the additional advantage that imaging is performed through the same objective used to focus the signal beam onto the sample. In practice, this capability can be leveraged to record from multiple ROIs within the same FOV, allowing the construction

of a spatial "map" of extracellular action potentials across the imaged FOV. For example, if the FOV contains multiple interconnected cells, then by recording the action potentials of different cells in the FOV, we can gain a better understanding of how those cells communicate with each other.

It is also interesting to consider potential regional variations in the action potential within a single cell. Because of the reduction in spot size achieved with microscope ECORE, it becomes possible to probe increasingly localized regions of an individual cardiomyocyte. Therefore, by keeping the beam fixed in place and moving the sample perpendicular to the optical axis, it is possible to sequentially record action potentials from different regions of the same cell. In our setup, we can perform such an experiment using the following steps:

1. Locate a cardiomyocyte that we want to study and identify different ROIs of the same cell
2. Using the known location of the beam, move the sample to align a specific ROI with the beam
3. Obtain a recording of the action potential from this ROI
4. Move the sample to another ROI and obtain a recording
5. Repeat the step above until recordings from all ROIs have been obtained

We performed this experiment by first locating a cardiomyocyte with strong electrical activity, and then obtaining recordings from 9 different regions of the cell by moving the sample, with the recording in each region lasting for 60 s. This sequential scanning procedure is depicted in Fig. 6.5(a).

After obtaining the recordings from these regions, we applied 10 Hz high-pass and 280 Hz low-pass filters to suppress the mechanical contraction signals and high frequency noise, respectively. Because the recordings are acquired sequentially (as opposed to simultaneously), they cannot be directly compared on a common time axis. However, when action potentials are present and clearly identifiable in a trace, they can serve as a reference point and allow us to manually align the traces. This allows for a direct comparison of the recordings from each region. The results of this procedure produce a spatial map of the electrical activity in the FOV.

The spatial map of the potentials corresponding to the 9 regions is shown in Fig. 6.5(b). The results of this mapping exercise show that the recorded electrical signals are stronger along the center column of the cell and weaker elsewhere. In particular, the electrical signals in the right column of Fig. 6.5(b) (regions 7, 4, and 8) are much weaker. One reason for this could be a potential lack of cellular activity in that area — while the left boundary of the cell is clearly visible in Fig. 6.5(a), the right boundary is not immediately clear. It is therefore possible that the recording regions on the right do not have substantial overlap with regions of a cardiomyocyte, therefore showing much weaker signals.

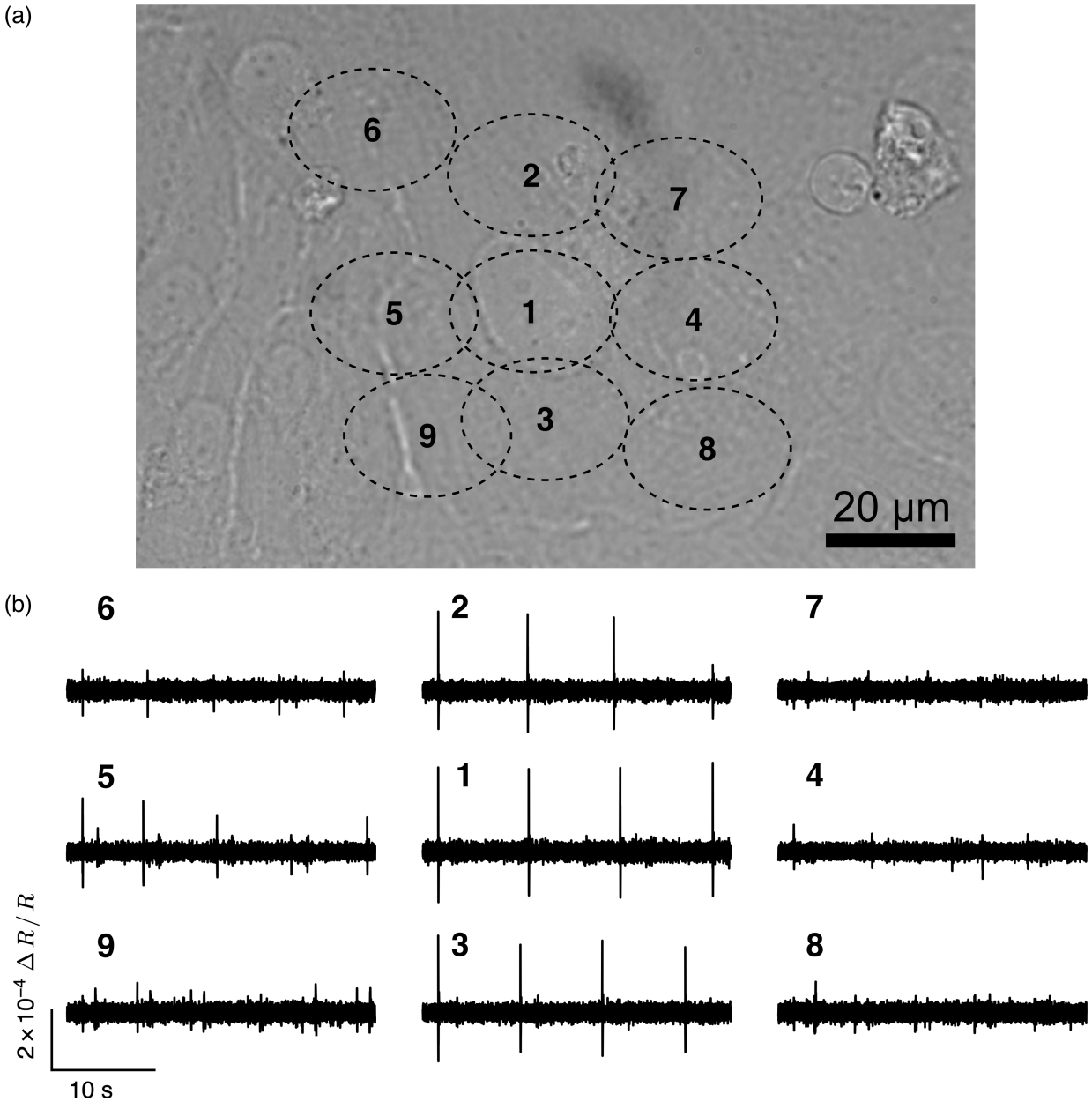

Figure 6.5: (a) This image is a still from a video captured during the recording of a cardiomyocyte. The cell being studied is centered in the frame. The left boundary of the cell is visible (white line running through the ellipses labeled 5 and 9), while other boundaries are not clearly visible. Each ellipse represents the $1/e^2$ radius spot size of the beam, while the labels represent the order with which recordings were obtained from each region of the sample. (b) 30 s sections of filtered recordings from each of the 9 regions shown in (a).

While we cannot conclusively interpret the biological significance of the observed regional variations in action potential amplitude in the cell shown in Fig. 6.5(a), the results (Fig. 6.5(b)) nevertheless illustrate the capability of microscope ECORE to generate spatial maps of extracellular potentials across one or multiple cells within the field of view of the objective.

This spatial mapping of potentials across the FOV could be further enhanced by implementing a rapid scanning procedure that sequentially records from multiple points within the imaging area. In such a scheme, the probing beam could be scanned across predefined locations at a sufficiently high rate, enabling essentially simultaneous recordings to be reconstructed from each position. This would enable time-resolved measurements of the spatial evolution of the signal, providing real-time information on how the action potential is generated and propagates across the FOV. As a result, such an approach would extend microscope ECORE from static spatial mapping to dynamic mapping of electrical activity.

Chapter 7

Summary and Outlook

This dissertation has described the extension of noninvasive, label-free recording using electrochromism by integrating a microscope objective into ECORE. Achieving this integration required careful noise reduction to ensure proper operation of a highly capable objective, whose performance is especially susceptible to external noise sources such as environmental vibrations. The use of a microscope objective provides several advantages compared to previous ECORE setups:

- Microscope ECORE utilizes a high-NA objective in a commercial microscope base using an alignment procedure commonly used in TIRF microscopy. This opens up microscope ECORE to the broader research community, particularly those researchers familiar with microscopy
- Once properly configured and optimized, the setup is simpler to align due to the objective, which allows us to reliably change the beam characteristics at the sample by performing simple manipulations of the beam at the back focal plane of the objective
- In addition to being used for ECORE, the objective can simultaneously be utilized to image the sample. This provides real-time information to the researcher and allows for easier identification of cells with high electrical activity
- The top of the sample is left completely accessible to the researcher. This access can be used to exchange drugs with the sample. This access could also be used to interact with the sample in other ways (e.g., by electrically stimulating the cells using electrodes)
- The spatial resolution is enhanced by using the objective, with much more room for improvement

Alongside these advantages, we show that microscope ECORE achieves a detection limit of 3 µV, a record for any ECORE setup. We demonstrate this increased sensitivity in the successful recording of action potentials from cardiomyocytes.

However, there are some notable limitations to the current microscope ECORE setup. We now discuss how these limitations may be overcome in the future to further enhance microscope ECORE and make it more versatile.

7.1 Improved spatial resolution

We have shown that the smallest theoretical spot size achievable in our setup would have a $1/e^2$ radius of 138 nm (see Fig. 4.3). Our current spot size, with a $1/e^2$ semi-minor axis of 9.4 µm, is much larger than this diffraction-limited spot. It is important to note that the limitation in the further reduction of our spot size is not the optical setup, but rather the onset of cell damage associated with smaller beam sizes.

As we briefly mentioned in the previous chapter, materials other than PEDOT may allow us to overcome this limitation. In the past, alternative materials such as PProDOT have been successfully used in ECORE to improve the detection limit of the setup at certain probing wavelengths [20]. While PProDOT does not improve the detection sensitivity in microscope ECORE operated with light of wavelength 510 nm, the exploration of alternative materials is still a promising avenue that may be further explored to find materials that are both less-absorptive (high R) and highly-responsive (high $\Delta R/R$). Finding such a material may allow for the recording of extracellular action potentials with high SNRs and without causing light-induced damage to the cells. This would also enable a significant reduction in the spot size of microscope ECORE, helping it approach diffraction-limited, subcellular spatial resolution.

7.2 Prolonged recording duration

Solutions that help improve the spatial resolution of microscope ECORE (by reducing the heat deposited due to light absorption in the electrochromic material) will also be helpful in improving the recording durations achieved with microscope ECORE.

In addition to seeking to prolong the recording duration at a single site, future developments of the method may also explore extending the time over which a sample can be kept healthy while mounted on microscope ECORE, allowing for the recording of a sample for $\gg 30$ min. This would require the use of an incubator incorporated with the microscope setup, which would keep the samples at 37 °C and maintain optimal humidity and CO_2 levels. Such incubators are commercially available and have been used for prolonged live-cell imaging [62, 63]. However, these incubators can make a setup more cumbersome to align and additional care has to be exercised to maintain the temperature of the sample, for example by heating the objective itself [62].

7.3 Dual-color microscope ECORE

Another interesting avenue for the future of microscope ECORE is the prospect of incorporating a second probing wavelength into the setup, as is done in dual-color ECORE [19]. Many microscopy experiments already utilize multiple excitation wavelengths within the same setup [64–66]. The addition of another light source to microscope ECORE would enable the benefits that dual-color ECORE has already presented, such as the enhancement of electrical signals and the reduction of artifacts. The second light source could also be used for fluorescence imaging, raising the exciting possibility of simultaneously recording electrical activity from a sample using ECORE and fluorescence-based voltage recording.

However, adding another light source would further increase the light intensity at the sample. Thus, the realization of a high resolution dual-color microscope ECORE setup may also require alternative materials that reduce light-induced cell damage.

7.4 Simultaneous spatial mapping of potentials

We have already shown how microscope ECORE can be used to create a spatial map of the extracellular potentials from a sample. The manual, sequential scanning that we have demonstrated allows us to learn about the magnitude and frequency of action potentials in multiple regions of the field of view (FOV) of the objective.

However, this type of scanning does not enable real-time observation of how action potentials propagate between different regions. To obtain this information, the beam must be rapidly scanned across multiple sites within the FOV, with a measurement acquired at each position. The following procedure could be used to implement rapid scanning:

1. Position the beam at a selected site and record for a fixed dwell time. This yields a single temporal sample for that location

2. Rapidly move the beam to the next site and repeat the measurement for the same dwell time. Continue this process until all desired sites in the FOV have been sampled

3. Repeat the full scan sequence to accumulate multiple temporal samples at each site

The key requirement in the above procedure is that each site must be revisited at a sufficiently high rate to achieve the desired sampling rate. For example, scanning 50 positions with a dwell time of 20 µs per position results in a full-frame scan time of 1 ms. Repeating this sequence continuously would then yield 1000 samples per second at each location, corresponding to an effective sampling rate of 1 kHz per site.

Our labs have recently developed and tested this scanning procedure for the original, prism-coupled ECORE setup. This procedure will be demonstrated in a manuscript currently under submission. In this work, an acousto-optical deflector (AOD) is used to rapidly scan the beam across the sample and record at each site with a desired sampling rate. This gives

an effectively simultaneous readout of the electrical signals from the different regions, and enables a direct comparison of the action potentials in the FOV across a common time axis.

In the future, we could therefore apply this scanning technique to microscope ECORE to realize a scanning microscope ECORE setup, which would yield time-resolved recordings of the spatial evolution of action potentials and greatly expand the spatial flexibility of ECORE. Furthermore, the AOD could be programmed using a simple graphical user interface to record from user-selected regions, giving researchers total recording flexibility within the FOV. If implemented, this would produce the most versatile form of ECORE: a platform that displays real-time images of bioelectric cells alongside their corresponding action potentials.

7.5 Conclusion

We have demonstrated microscope ECORE as a highly-sensitive, label-free method for the recording of bioelectric potentials. The use of a high-NA objective unlocks improvements in spatial resolution and simultaneous imaging, opening clear paths for the continued development of noninvasive optical recording methods. Furthermore, by leveraging existing microscopy techniques, this approach expands the established capabilities of ECORE while simplifying its practical implementation. Microscope ECORE therefore provides a more accessible platform for researchers to utilize this technique in their own studies. By reducing the technical barriers to entry, we anticipate that this method can support the broader scientific community in exploring the complex workings of bioelectric systems.

Bibliography

[1] P. Liu and E. W. Miller, "Electrophysiology, Unplugged: Imaging Membrane Potential with Fluorescent Indicators", Accounts of Chemical Research **53**, 11–19 (2020).

[2] N. Axmacher, F. Mormann, G. Fernández, C. E. Elger, and J. Fell, "Memory formation by neuronal synchronization", Brain Research Reviews **52**, 170–182 (2006).

[3] J. C. Calderón, P. Bolaños, and C. Caputo, "The excitation–contraction coupling mechanism in skeletal muscle", Biophysical Reviews **6**, 133–160 (2014).

[4] G. M. Wahler, "52 - cardiac action potentials", in *Cell physiology source book (third edition)*, edited by N. Sperelakis, Third Edition (Academic Press, San Diego, 2001), pp. 887–898.

[5] S. Peng, A. E. Lacerda, G. E. Kirsch, A. M. Brown, and A. Bruening-Wright, "The action potential and comparative pharmacology of stem cell-derived human cardiomyocytes", Journal of Pharmacological and Toxicological Methods **61**, 277–286 (2010).

[6] O. Caspi, I. Itzhaki, I. Kehat, A. Gepstein, G. Arbel, I. Huber, J. Satin, and L. Gepstein, "In Vitro Electrophysiological Drug Testing Using Human Embryonic Stem Cell Derived Cardiomyocytes", Stem Cells and Development **18**, 161–172 (2009).

[7] M. Scanziani and M. Häusser, "Electrophysiology in the age of light", Nature **461**, 930–939 (2009).

[8] D. S. Peterka, H. Takahashi, and R. Yuste, "Imaging Voltage in Neurons", Neuron **69**, 9–21 (2011).

[9] E. K. St. Louis and L. C. Frey, "Introduction", in *Electroencephalography (eeg): an introductory text and atlas of normal and abnormal findings in adults, children, and infants* (American Epilepsy Society, 2016), 4 to 6.

[10] E. Neher and B. Sakmann, "Single-channel currents recorded from membrane of denervated frog muscle fibres", Nature **260**, 799–802 (1976).

[11] C. L. Hill and G. J. Stephens, "An introduction to patch clamp recording", in *Patch clamp electrophysiology: methods and protocols*, edited by M. Dallas and D. Bell (Springer US, New York, NY, 2021), pp. 1–19.

[12] Y. Zhou, E. Liu, H. Müller, and B. Cui, "Optical electrophysiology: toward the goal of label-free voltage imaging", Journal of the American Chemical Society **143**, 10482–10499 (2021).

[13] E. W. Miller, "Small molecule fluorescent voltage indicators for studying membrane potential", Current Opinion in Chemical Biology **33**, 74–80 (2016).

[14] J. Pine, "Recording action potentials from cultured neurons with extracellular microcircuit electrodes", Journal of Neuroscience Methods **2**, 19–31 (1980).

[15] R. U. Kulkarni and E. W. Miller, "Voltage Imaging: Pitfalls and Potential", Biochemistry **56**, 5171–5177 (2017).

[16] P.-C. Zhang, A. M. Keleshian, and F. Sachs, "Voltage-induced membrane movement", Nature **413**, 428–432 (2001).

[17] J. F. Barry, M. J. Turner, J. M. Schloss, D. R. Glenn, Y. Song, M. D. Lukin, H. Park, and R. L. Walsworth, "Optical magnetic detection of single-neuron action potentials using quantum defects in diamond", Proceedings of the National Academy of Sciences **113**, 14133–14138 (2016).

[18] F. S. Alfonso, Y. Zhou, E. Liu, A. F. McGuire, Y. Yang, H. Kantarci, D. Li, E. Copenhaver, J. B. Zuchero, H. Müller, and B. Cui, "Label-free optical detection of bioelectric potentials using electrochromic thin films", Proceedings of the National Academy of Sciences **117**, 17260–17268 (2020).

[19] Y. Zhou, E. Liu, Y. Yang, F. S. Alfonso, B. Ahmed, K. Nakasone, C. Forró, H. Müller, and B. Cui, "Dual-Color Optical Recording of Bioelectric Potentials by Polymer Electrochromism", Journal of the American Chemical Society **144**, 23505–23515 (2022).

[20] Y. Zhou, E. Liu, A. M. Österholm, A. L. Jones, P. Sun, Y. Yang, C.-T. Tsai, T. Zaluska, W. Zhang, H. Müller, J. R. Reynolds, and B. Cui, "Ultrasensitive label-free optical recording of bioelectric potentials using dioxythiophene-based electrochromic polymers", Nature Communications **16**, 6776 (2025).

[21] M. W. Barnett and P. M. Larkman, "The action potential", Practical Neurology **7**, 192–197 (2007).

[22] D. M. Bers, "Cardiac excitation–contraction coupling", Nature **415**, 198–205 (2002).

[23] A. O. Grant, "Cardiac ion channels", Circulation: Arrhythmia and Electrophysiology **2**, 185–194 (2009).

[24] N. Klauke, G. L. Smith, and J. Cooper, "Extracellular Recordings of Field Potentials from Single Cardiomyocytes", Biophysical Journal **91**, 2543–2551 (2006).

[25] T. Kaneko, H. Toriumi, J. Shimada, and F. Nomura, "Extracellular field potential recording of single cardiomyocytes in agarose microchambers using microelectrode array", Japanese Journal of Applied Physics **57**, 03EB03 (2018).

[26] A. L. Hodgkin and A. F. Huxley, "Action potentials recorded from inside a nerve fibre", Nature **144**, 710–711 (1939).

[27] A. L. Hodgkin and A. F. Huxley, "A quantitative description of membrane current and its application to conduction and excitation in nerve", The Journal of Physiology **117**, 500–544 (1952).

[28] B. Sakmann and E. Neher, "Patch Clamp Techniques for Studying Ionic Channels in Excitable Membranes", Annual Review of Physiology **46**, 455–472 (1984).

[29] M. E. Spira and A. Hai, "Multi-electrode array technologies for neuroscience and cardiology", Nature Nanotechnology **8**, 83–94 (2013).

[30] C. Xie, Z. Lin, L. Hanson, Y. Cui, and B. Cui, "Intracellular recording of action potentials by nanopillar electroporation", Nature Nanotechnology **7**, 185–190 (2012).

[31] R. Burley and J. R. M. Harvey, "Multielectrode arrays", in *Patch clamp electrophysiology: methods and protocols*, edited by M. Dallas and D. Bell (Springer US, New York, NY, 2021), pp. 109–132.

[32] M. Schröter, F. Cardes, C.-V. H. Bui, L. D. Dodi, T. Gänswein, J. Bartram, L. Sadiraj, P. Hornauer, S. Kumar, M. Pascual-Garcia, and A. Hierlemann, "Advances in large-scale electrophysiology with high-density microelectrode arrays", Lab on a Chip **25**, 4844–4885 (2025).

[33] D. Tsai, D. Sawyer, A. Bradd, R. Yuste, and K. L. Shepard, "A very large-scale microelectrode array for cellular-resolution electrophysiology", Nature Communications **8**, 10.1038/s41467-017-02009-x (2017).

[34] B. M. Salzberg, A. L. Obaid, D. M. Senseman, and H. Gainer, "Optical recording of action potentials from vertebrate nerve terminals using potentiometric probes provides evidence for sodium and calcium components", Nature **306**, 36–40 (1983).

[35] R. Yuste and W. Denk, "Dendritic spines as basic functional units of neuronal integration", Nature **375**, 682–684 (1995).

[36] Y. Bando, M. Sakamoto, S. Kim, I. Ayzenshtat, and R. Yuste, "Comparative evaluation of genetically encoded voltage indicators", Cell Reports **26**, 802–813.e4 (2019).

[37] W. Akemann, H. Mutoh, A. Perron, Y. K. Park, Y. Iwamoto, and T. Knöpfel, "Imaging neural circuit dynamics with a voltage-sensitive fluorescent protein", Journal of Neurophysiology **108**, 2323–2337 (2012).

[38] Y. Han, J. Yang, Y. Li, Y. Chen, H. Ren, R. Ding, W. Qian, K. Ren, B. Xie, M. Deng, Y. Xiao, J. Chu, and P. Zou, "Bright and sensitive red voltage indicators for imaging action potentials in brain slices and pancreatic islets", Science Advances **9**, 10.1126/sciadv.adi4208 (2023).

[39] W. Akemann, H. Mutoh, A. Perron, J. Rossier, and T. Knöpfel, "Imaging brain electric signals with genetically targeted voltage-sensitive fluorescent proteins", Nature Methods **7**, 643–649 (2010).

[40] X. Lu, Y. Wang, Z. Liu, Y. Gou, D. Jaeger, and F. St-Pierre, "Widefield imaging of rapid pan-cortical voltage dynamics with an indicator evolved for one-photon microscopy", Nature Communications **14**, 10.1038/s41467-023-41975-3 (2023).

[41] P. P. Laissue, R. A. Alghamdi, P. Tomancak, E. G. Reynaud, and H. Shroff, "Assessing phototoxicity in live fluorescence imaging", Nature Methods **14**, 657–661 (2017).

[42] A. Gonzalez-Perez, L. Mosgaard, R. Budvytyte, E. Villagran-Vargas, A. Jackson, and T. Heimburg, "Solitary electromechanical pulses in lobster neurons", Biophysical Chemistry **216**, 51–59 (2016).

[43] H. J. Lee, D. Zhang, Y. Jiang, X. Wu, P.-Y. Shih, C.-S. Liao, B. Bungart, X.-M. Xu, R. Drenan, E. Bartlett, and J.-X. Cheng, "Label-Free Vibrational Spectroscopic Imaging of Neuronal Membrane Potential", The Journal of Physical Chemistry Letters **8**, 1932–1936 (2017).

[44] R. J. Mortimer, "Electrochromic materials", Annual Review of Materials Research **41**, 241–268 (2011).

[45] A. V. Shchegolkov, S.-H. Jang, A. V. Shchegolkov, Y. V. Rodionov, A. O. Sukhova, and M. S. Lipkin, "A brief overview of electrochromic materials and related devices: a nanostructured materials perspective", Nanomaterials **11**, 2376 (2021).

[46] A. Kraft, "Too blue to be good? a critical overview on the electrochromic properties and applications of prussian blue", Solar Energy Materials and Solar Cells **278**, 113195 (2024).

[47] F. S. Alfonso, "Label free optical detection of bioelectric potentials using electrochromic thin films", PhD thesis (Stanford University, Stanford, California, 2019).

[48] J. Peatross and M. Ware, "Plane waves and refractive index", in *Physics of light and optics* (2015), pp. 43–72.

[49] S. J. Byrnes, "Multilayer optical calculations", arXiv:1603.02720, 10.48550/arXiv.1603.02720 (2020).

[50] J. Peatross and M. Ware, "Reflection and refraction", in *Physics of light and optics* (2015), pp. 73–88.

[51] P. C. D. Hobbs, *Building electro-optical systems* (John Wiley & Sons, Ltd, 2022).

[52] B. Ahmed, E. Liu, L. Maisenbacher, P. Sun, D. Griffith, K. Nakasone, Y. Zhou, B. Cui, and H. Müller, "Microscopy of bioelectric potentials using electrochromism", arXiv:2602.00363, 10.48550/arXiv.2602.00363 (2026).

[53] D. B. Murphy and M. W. Davidson, "Diffraction and interference in image formation", in *Fundamentals of light microscopy and electronic imaging* (John Wiley & Sons, Inc., Hoboken, NJ, USA, Sept. 2012), pp. 78–101.

[54] D. B. Murphy and M. W. Davidson, "Lenses and geometrical optics", in *Fundamentals of light microscopy and electronic imaging* (John Wiley & Sons, Inc., Hoboken, NJ, USA, Sept. 2012), pp. 53–77.

[55] A. E. Siegman, "An introduction to lasers", in *Lasers* (University Science Books), pp. 1–79.

[56] D. Axelrod, "Optical configurations and setup", in *Total internal reflection fluorescence (tirf) and evanescence microscopies* (IOP Publishing, 2022), 5–1 to 5–32.

[57] A. Yildiz and R. D. Vale, "Total internal reflection fluorescence microscopy", Cold Spring Harbor Protocols **2015**, pdb.top086348 (2015).

[58] L. Dresser, P. Hunter, F. Yendybayeva, A. L. Hargreaves, J. A. Howard, G. J. Evans, M. C. Leake, and S. D. Quinn, "Amyloid-β oligomerization monitored by single-molecule stepwise photobleaching", Methods **193**, 80–95 (2021).

[59] A. L. Mattheyses, S. M. Simon, and J. Z. Rappoport, "Imaging with total internal reflection fluorescence microscopy for the cell biologist", Journal of Cell Science **123**, 3621–3628 (2010).

[60] P. Horowitz and W. Hill, "Low-noise techniques", in *The art of electronics* (Cambridge University Press, 2015), pp. 473–593.

[61] V. V. Fedorov, I. T. Lozinsky, E. A. Sosunov, E. P. Anyukhovsky, M. R. Rosen, C. W. Balke, and I. R. Efimov, "Application of blebbistatin as an excitation–contraction uncoupler for electrophysiologic study of rat and rabbit hearts", Heart Rhythm **4**, 619–626 (2007).

[62] M. M. Frigault, J. Lacoste, J. L. Swift, and C. M. Brown, "Live-cell microscopy – tips and tools", Journal of Cell Science **122**, 753–767 (2009).

[63] H.-F. Tsai, D. Carlson, A. Koldaeva, S. Pigolotti, and A. Shen, "Optimization and fabrication of multi-level microchannels for long-term imaging of bacterial growth and expansion", Micromachines **13**, 576 (2022).

[64] C. Rodríguez, Y. Liang, R. Lu, and N. Ji, "Three-photon fluorescence microscopy with an axially elongated bessel focus", Optics Letters **43**, 1914 (2018).

[65] H. Shroff, C. G. Galbraith, J. A. Galbraith, H. White, J. Gillette, S. Olenych, M. W. Davidson, and E. Betzig, "Dual-color superresolution imaging of genetically expressed probes within individual adhesion complexes", Proceedings of the National Academy of Sciences **104**, 20308–20313 (2007).

[66] H. Blanc, G. Kaddour, N. B. David, W. Supatto, J. Livet, E. Beaurepaire, and P. Mahou, "Chromatically corrected multicolor multiphoton microscopy", ACS Photonics **10**, 4104–4111 (2023).